IFToMM

The 16th World Congress of the International Federation for the Promotion of Mechanism and Machine Science

November 5th ~ 10th 2023, Tokyo, Japan

Abstract Booklet

Abstract Booklet of the 16th World Congress of the International Federation
for the Promotion of Mechanism and Machine Science
November 4th 2023
Tokyo, Japan

List of Extended Abstracts

Biomedical Engineering

Computational Kinematics

Education

Engines and Powertrains

Gearing and Transmissions

History of Mechanism and Machine Science

Linkages and Mechanical Controls

Multibody Dynamics

Robotics and Mechatronics

Standardization of Terminology

Transportation Machinery

Tribology

Investigating the Impact of Multiple Tasks on the Estimation of Non-identifiable Muscle Parameters in Musculoskeletal Models: a preliminary study

Yi-Hsuan Lin and Kuei-Yuan Chan[1]

Department of Mechanical Engineering,
National Taiwan University, Taipei 10617, Taiwan,
chanky@ntu.edu.tw

1 Introduction

Developing subject-specific models that accurately represent the muscle parameters is crucial for improving rehabilitation and sports science outcomes. This study aims to estimate these parameters using a musculoskeletal (MSK) model and an optimization technique similar to [1]. However, identifying the correct parameters can be challenging when multiple combinations of parameters can produce similar kinematics [2]. To overcome this challenge, we explore the use of optimization tools with multiple performance metrics to determine the parameter values that are non-identifiable. We conduct several simulation cases to demonstrate the effectiveness of our approach.

2 Methodology and Results Discussion

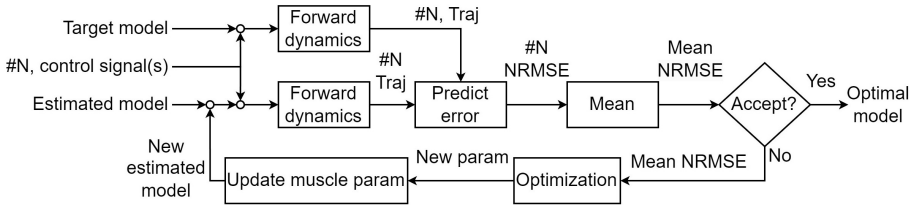

Fig. 1. Flowchart for kinematic trajectory prediction and optimization for N task(s).

In this study, the OpenSim Arm26 MSK model [3] was used to evaluate elbow joint kinematics and biceps muscle parameters. Tasks were selected for evaluation that involved both load and motion, which the kinematic trajectory fitted as transformed sine functions. Control signals from the target model and the Computed Muscle Control tool were used to produce target trajectory via the

Forward Dynamics tool. The difference between the estimated model's trajectory and the target trajectory was quantified using normalized root-mean-square error (NRMSE), with the mean NRMSE used as the objective function in the optimization problem. The parameters were updated using an optimization technique to find the optimal model's best-matching trajectory. It is worth noting that the estimated model differs from the target model solely in terms of the unknown muscle parameters, and the compared trajectories are based on joint speed. The entire process is illustrated in Fig. 1. The evaluation of parameters using single-task or dual-task was carried out using MATLAB and OpenSim API. Subsequently, we will explore how optimization tools facilitate the identification of muscle parameters' values or the observation of their non-identifiability.

The optimization results for each case and target values are presented in Table 1. The NRMSE for the single-task case was significantly smaller than that of [1], but the difference from the target parameters remained significant. However, when multiple tasks were utilized to evaluate the parameters simultaneously, the optimal parameters were found to be closer to the target values. Therefore, utilizing multiple tasks can aid in increasing the accuracy of the estimation.

Table 1. Parameter estimation results for single-task case ($\#N = 1$) / dual-task case ($\#N = 2$) / target values in order, including maximum isometric force ($F_{\mathrm{O}}^{\mathrm{M}}$), tendon slack length ($L_{\mathrm{O}}^{\mathrm{M}}$), and optimal fiber length ($L_{\mathrm{S}}^{\mathrm{T}}$). The mean NRMSE for single-task and dual-task cases are 5.14×10^{-3} and 1.08×10^{-4}, respectively.

Muscle name	$F_{\mathrm{O}}^{\mathrm{M}}$ (N)	$L_{\mathrm{O}}^{\mathrm{M}}$ (m)	$L_{\mathrm{S}}^{\mathrm{T}}$ (m)
Biceps (long head)	574.49/624.60/624.30	0.1346/0.1156/0.1157	0.2326/0.2724/0.2723
Biceps (short head)	356.98/435.26/435.56	0.1078/0.1321/0.1321	0.1949/0.1923/0.1923

Acknowledgement

This work was supported by the National Science and Technology Council of Taiwan under grant MOST 111-2223-E-002 -004 -MY3.

References

1. Hinson Jr, Robert, et al. "Sensitivity analysis guided improvement of an electromyogram-driven lumped parameter musculoskeletal hand model." Journal of Biomechanics 141 (2022): 111200.
2. Bujalski, P., J. Martins, and L. Stirling. "A Monte Carlo analysis of muscle force estimation sensitivity to muscle-tendon properties using a Hill-based muscle model." Journal of Biomechanics 79 (2018): 67-77.
3. Delp, Scott L., et al. "OpenSim: open-source software to create and analyze dynamic simulations of movement." IEEE Transactions on Biomedical Engineering 54.11 (2007): 1940-1950.

Development of the Classification System for Surgical Skills in Endoscopic Sinus Surgery

Kaito Yamada[1], Masanobu Suzuki[2], Kou Miyaji[1], Koki Ebina[1]
Kazuya Sase[3], Teppei Tsujita[4], Xiaoshuai Chen[5], Takashige Abe[6]
Shunsuke Komizunai[7], Yuji Nakamaru[2], Taku Senoo[1]
Akihiro Homma[2], and Atsushi Konno[1]

[1] Grad. school of Information Science and Technology, Hokkaido University, Japan,
{yamada@scc, konno@ssi}.ist.hokudai.ac.jp
[2] Dept. of Otolaryngology-Head and Neck Surgery, Hokkaido University, Japan
[3] Dept. of Mech. Eng. and Intelligent Systems, Tohoku Gakuin University, Japan
[4] Dept. of Mech. Eng., National Defense Academy of Japan, Japan
[5] Grad. School of Science and Technology, Hirosaki University, Japan
[6] Dept. of Urology, Hokkaido University, Japan
[7] Faculty of Eng. and Design, Kagawa University, Japan

1 Introduction

Endoscopic Sinus Surgery (ESS) is an operation that requires a high level of skill, and there is a need to develop an efficient training method. Therefore, in this study, the movement data of surgical instruments in ESS and the open sinus volume as a result of the surgery were obtained through the measurement experiment. Machine learning was performed using indices calculated from the measured data. This paper describes the details of the building the classification model that evaluates the surgical skill of surgeon.

2 Methods

Thirty-six participants performed one full-house ESS for sinus opening using an elaborate 3D sinus model. Simulated surgeries were measured using a system that can simultaneously measure multiple instruments based on motion capture (Fig. 1), and several kinematic indices were calculated from the measured data. The volume of the open sinus were also calculated from the CT images of the postoperative 3D sinus model [1], and these indices were used as input for building model. The experienced surgeon evaluated the surgical skill by refereeing endoscopic camera images based on the evaluation index for ESS (ESS-OSATS) [2]. Three machine learning algorithms, SVM (Support Vector Machine), PCA (Principal Component Analysis based)-SVM, and GBDT (Gradient Boosting Decision Tree), were used in this study. The model accuracy was evaluate by nested and repeated 10-fold cross-validation. In 10-fold cross-validation, 36 data sets were divided into 10 data sets, one as test data and nine as training data. The Friedman test and the Wilcoxon signed-rank sum test were utilized to compare these accuracies.

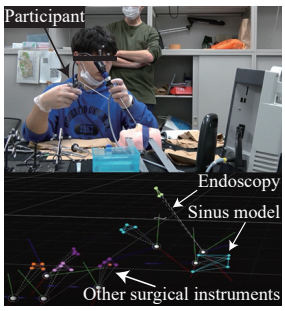

Fig. 1: Overview of experiment

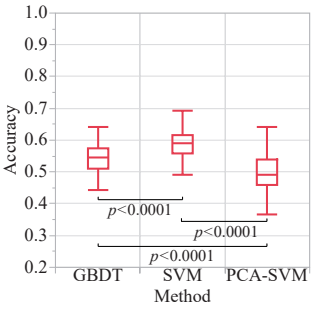

(a) Three-class classification

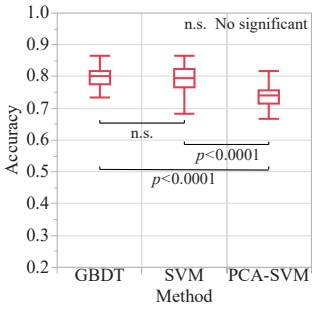

(b) Two-class classification

Fig. 2: Accuracy of each classifier

3 Result

The participants were divided into three or two classes according to their ESS-OSATS scores. In three-class discrimination, the difference between Experts (n=13, score=65–78) vs. Intermediates (n=9, score=54–64) vs. Novices (n=14, score=18–53) was examined. In two-class discrimination, the difference between Experts (n=13, score=65–78) vs. Novices and Intermediates (n=23, score=18–64) was examined. Figure 2 shows a plot of the classification accuracy after 100 runs for each method. The validation results showed that the SVM was superior to the other methods in three-class classification (median accuracy: 59.2%). In the two-class classification, SVM and GBDT were superior to the PCA-SVM (79.6% and 80.0%, respectively). Note that there were no significant difference between SVM and GBDT.

4 Conclusion

In this study, a surgical skill classification system was developed based on the kinematic indices and the sinus volume obtained in the measurement experiments using elaborate 3D sinus model. The accuracy of the three classification methods was compared, and SVM was found to be the best method for the skill classification system. The next task is to develop a score evaluation system using a regression method that provides more specific and quantitative feedback.

Acknowledgement

This work was supported by JSPS Grant-in-Aid for Scientific Research (A) (18H04102) & (23H00480).

References

1. K. Yamada, et al.: “A study of techniques for evaluating endoscopic surgery skills,” SICE SI 2022, pp. 807–810, 2022. (in Japanese)
2. S.Y. Lin, et al.: “Development and Pilot-Testing of a Feasible, Reliable, and Valid Operative Competency Assessment Tool for Endoscopic Sinus Surgery,” American Journal of Rhinology & Allergy, vol. 23, no. 3, pp. 354–359, 2009.

Nordic Walking Simulation Research

Jacek Bałchanowski[1[0000-0002-1510-0122]] and Sławomir Wudarczyk[1[0000-0003-4953-4516]] and Artur Handke[1[0000-0002-6727-2751]]

[1] Wrocław University of Science and Technology, Wrocław, Poland
jacek.balchanowski@pwr.edu.pl,slawomir.wudarczyk@pwr.edu.pl,
artur.handke@pwr.edu.pl

1 Material and methods

The positive health effects of Nordic Walking (NW) have been demonstrated in many works. However, there is still a lack of evidence regarding how NW walking changes the stress relief of human limb joints. The study aimed to develop a numerical model of the human locomotor system during gait and NW and conduct simulation research. The aim of the simulation was to compare the forces in selected joints during human gait and NW. The first step in building a computer model of human motion was to acquire data from the real object [1]. A measurement system (Fig 1) using inertial IMU sensors (iSen STT-Systems) was used to obtain the biomechanics of human motion. NW pole orientation angles and ground forces (along the NW pole axis) were measured using the developed mobile mechatronic NW measurement system [2, 3]. Both systems were synchronized in time using an appropriate timestamp (trigger). The measurements allowed us to obtain the kinematic parameters of individual limb segments. The files obtained from iSen STT-Systems in BVH format had to be transformed and integrated with the data obtained from the author's mechatronic NW pole measurement system. Only adequately prepared data were applied as kinematic excitation in the model.

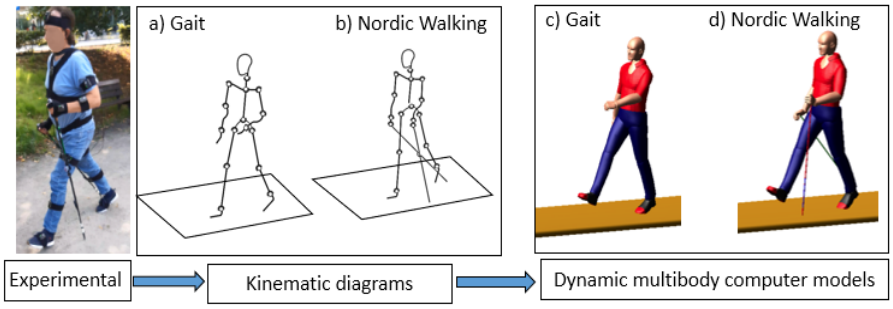

Fig. 1. Stages of building a model of human biomechanics during gait and with NW poles in the computer system for dynamic analysis of multibody systems.

The numerical model of human gait biomechanics was based on a structure containing the upper and lower limbs, the body formed from the combination of the pelvis, the trunk with the thorax, and the head bedded on the neck. All joints in the model were replaced with spherical kinematic pairs, thus allowing direct transfer of data obtained

from measurements to force relative movements in the model. In joints with fewer degrees of freedom, the corresponding rotations were zero. This approach allowed the format of the kinematic forcing functions to be unified. The grip of the NW stick with the hand was also modelled using a spherical joint. Contact between the feet and the ground was modelled using flexibility and friction. The developed parametric computer model made it possible to use measurements of gait parameters obtained for professionals, amateurs of both sexes for simulation studies.

2 Result

As part of a simulation study of a man during normal gait and NW, the runs of interaction forces in the modelled joints were obtained. Fig. 2 shows example load diagrams at the left hip and right knee joints during the gait and Nordic Walking of a middle-aged man (55 years old, 83 kg body weight, 170 cm high).

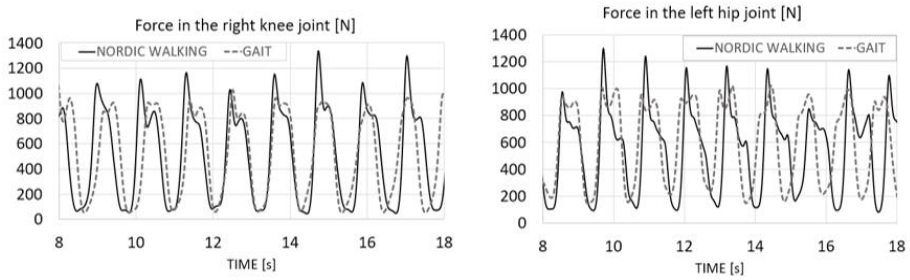

Fig. 2. Interaction force runs in the right knee and left hip joint during gait and NW

3 Final Remarks

Simulation studies have made it possible to determine and compare loads in selected human joints during walking with and without NW poles. Analyses of the results of the simulation studies indicate that proper using NW poles causes less load in some joints with respect to gait (without NW poles) with similar kinematic parameters of movement.

References

1. Seel T., Raisch J., Schauer T., IMU-based joint angle measurement for gait analysis, Sensors (Basel), 2014, 14.
2. Wudarczyk, S., et al.: Research on the mechatronic gait monitoring system with Nordic Walking poles. In: 15th International Conference Mechatronic Systems and Materials, MSM 2020, IEEE, cop., Piscataway (2020).
3. Wudarczyk, S., et al.: Experimental research on mechatronic Nordic Walking poles. In: 15th International Conference Mechatronic Systems and Materials, MSM 2020. IEEE, cop., Piscataway (2020).

Soft Robot for Cell Culture with Multi-directional Mechanical Stretches

Atsushi TAKATA, Takayoshi KAMADA, and Yuta KURASHINA

Department of Mechanical Systems Engineering,
Tokyo University of Agriculture and Technology, Japan, takata-a@go.tuat.ac.jp

Keywords: Soft robot, Cell culture, Pneumatic actuator.

1 Introduction

To date, the mechanism of how skeletal muscle matures is unproven. Thus, some diseases such as muscular dystrophy are still intractable. One of the key factors in myoblasts' maturation that researchers have been tackling is mechanical stimuli. In a previous study, the myoblasts of the mouse were repeatedly stretched in one direction using a novel flexible cell chamber, and its real-time response was observed during incubation [1]. However, real mechanical stretches of myoblasts in our body are multi-directional because muscles not only contract but also are bent. Therefore, in our study, a soft robot actuated by pneumatic power is utilized to load multi-directional strain on cells. Although some bioengineering studies utilized soft robots that move a single bending-like motion [2], our robotic chamber is the first case of multi-directional movement. After that, deformations were measured by image processing.

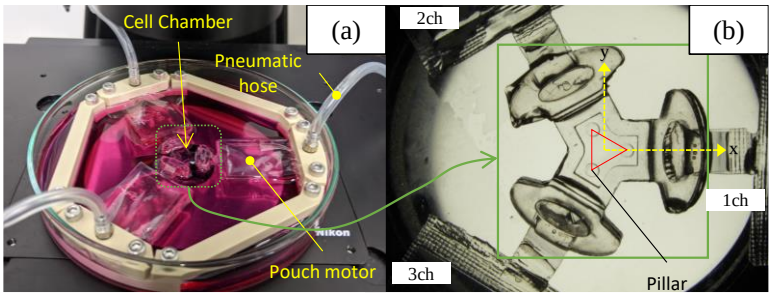

Fig. 1. Soft robotic chamber moves in multi-direction.
(a) Overview of the robot. (b) Deformation was captured by a microscope.

2 Design of Robot with Pneumatic Actuator

The developed system is shown in Fig. 1(a). The cell chamber was made by casting PDMS. The pouch motor [3] is an actuator that is made of heat-sealed nylon film. The light brown exoskeleton parts were PEEK. Since all parts can be sterilized, this system

is suitable for cell culture. As shown in Fig. 1(b), three pouch motors 1ch, 2ch, and 3ch contract when air pressure is applied through the air hoses. And they pull the chamber in a horizontal xy-plane. Furthermore, Fig. 2 shows C2C12 cells that were suspended in collagen gel and seeded on the culturing zone.

3 Evaluation of Strain using Image Processing

The strain generated in the chamber by pouch motors was captured from the top using a microscope. There are three pillars in the culturing zone, and we measured the deformation of a triangle with them as vertices. An air pressure of 60 kPa was applied to 1ch, 2ch, and 3ch in turn. The strain assumed that the deformation is linear in the same way as the triangular elements in FEM method. Figure 3 shows the resultant x-strain ε_x, y-strain ε_y, and xy-shear strain γ_{xy}. A maximum strain of 7.1% occurred. The strain of our device needs to be enlarged because muscle cells *in vivo* contract by about 10%.

Fig. 2. Cells in developed chamber.

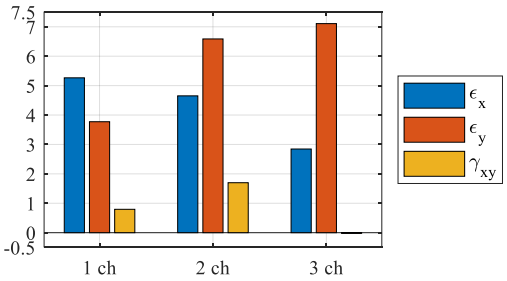

Fig. 3. Air Pressure 60 kPa caused up to 7.1% strain.

4 Conclusion

In this paper, we developed a cell chamber with soft actuators that give multi-directional stretch. The strain generated in the culturing zone was measured by image processing, and the strain was up to 7.1%. In the future, we will work on improving the actuator for larger strain and cell culture with stretching stimuli.

References

1. K. Kasahara, Y. Kurashina, S. Miura, S. Miyata and H. Onoe, “Real-Time Three- Dimensional Single-Cell-Resolution Monitoring System for Observation of Dynamic Cell Behavior under Mechanical Stimuli,” 2021 IEEE MEMS, 454-457(2021).
2. Paek, J., Song, J.W., Ban, E. et al. Soft robotic constrictor for in vitro modeling of dynamic tissue compression. Sci Rep 11, 16478 (2021).
3. R. Niiyama, D. Rus and S. Kim, “Pouch Motors: Printable/inflatable soft actuators for robotics,” 2014 ICRA, 6332-6337(2014).

Power Transmission Mechanism from Upper Limb to Lower Limb by Pneumatic Artificial Muscles for Development of Self-Assist Suit

Ayumu Nara[1] and Kenji Hashimoto[2][0000-0003-2300-6766]

[1] Meiji University, 1-1-1 Higashi-Mita, Tama-ku, Kawasaki, Kanagawa 214-8571, Japan
[2] Waseda University, 2-7 Hibikino, Wakamatsu-ku, Kitakyushu, Fukuoka 808-0135, Japan
kenji.hashimoto@waseda.jp

Walking is necessary to maintain quality of life. In recent years, the percentage of people who run to keep their health has increased, but running places a heavy load on the lower body, making it difficult for people whose muscles have begun to deteriorate to run long distances. This is why people of all ages are attracted to Nordic walking (walking with poles), which actively uses the upper body [1]. Similarly, if the energy of the upper body can be transferred to the lower body, the load on the lower body can be reduced. Therefore, our long-term goal is to develop a support suit that can transfer the energy of a runner's upper body to the lower body so that people who have begun to lose muscle can still enjoy jogging and running.

There are many walking support robots with electric actuators, such as Robot Suit HAL® [2]. However, most of them support walking with the actuators installed in the walking support robot, so they have little effect on increasing the wearer's muscle strength. Therefore, our goal is to develop a "self-assist suit" that can assist the wearer by its own power in the long term. The objective of this research is to develop a power transmission mechanism that can transfer energy from the upper limb to the lower limb for the realization of the self-assist suit.

There are various possible methods of transmitting power from the upper limb to the lower limb, including the use of link mechanisms, wires, and rubber. In this study, we chose to use air pressure to transmit power, with the possibility of future expansion, such as transmitting power from one joint of the upper limb to multiple joints of the lower limb. Specifically, McKibben artificial muscles are used in the power transmission mechanism. Two pressurized artificial muscles are connected in series, and when one artificial muscle (the drive side) is extended, the other (the driven side) contracts (see Fig. 1 (a)).

Focusing on the knee joint during walking, the angular change is approximately 60 degrees [3]. Considering the thickness of the human thigh and lower leg, the required contraction rate for artificial muscles is about 10%.

The McKibben artificial muscles consist of a rubber tube covered with a synthetic fiber sleeve. When pressure is applied to the rubber tube, the radial expansion force of the rubber tube is converted into an axial contraction force by the synthetic fiber sleeve. Due to the working principle, the contraction rate of McKibben artificial muscles varies depending on the combination of material and dimensions of the rubber tube and sleeve.

The urethane tube is often used for the rubber tube in the McKibben artificial muscle, but as shown in Fig. 1 (b), this did not provide sufficient contraction. As a result of trial and error, we used R-Air (a racing bicycle tube sold by Panaracer Co., Ltd.), which has excellent elasticity, for the rubber tube. When the artificial muscle using R-Air on the drive side was pulled under 0.05 MPa pressure as the initial condition, a contraction rate of more than 10% was obtained. Furthermore, when the volume of the drive-side artificial muscle was relatively increased by making the natural length of the driven-side artificial muscle 1/2 the length of the drive-side artificial muscle, an even greater contraction rate was obtained, as shown in Fig. 1 (b).

Through experiments, it was suggested that a power transmission mechanism using pneumatic artificial muscles with R-air could be applied to a self-assist suit. Fig. 1 (c) shows the self-assist suit currently under development using the power transmission mechanism described in this study.

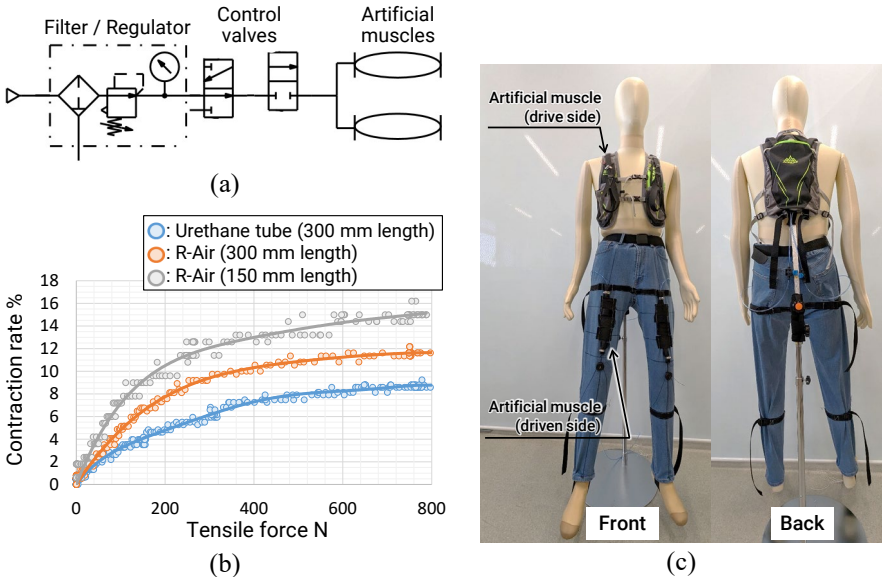

Fig. 1. Proposed power transmission mechanism: (a) Pneumatic schematic of power transmission mechanism using pneumatic artificial muscles, (b) Experimental results of power transmission mechanism evaluation, (c) Self-assist suit using the power transmission mechanism.

References

1. Tschentscher, M. Niederseer, D., Niebauer, J.: Health Benefits of Nordic Walking: A Systematic Review. American Journal of Preventive Medicine 44(1), 76-84 (2013).
2. Sankai, Y.: Leading Edge of Cybernics: Robot Suit HAL. In: 2006 SICE-ICASE International Joint Conference, pp. P-1-P-2, Busan, Korea (2006).
3. Perry, J.: Gait Analysis: Normal and Pathological Function. Slack Inc. (1992).

System Stability Evaluation of Head-Shaking Test Using Balance Controller Parameters

Emiko Uchiyama[1] and Wataru Takano[2]

[1] The University of Tokyo, 7-3-1, Hongo, Bunkyo-ku, Tokyo, 113-8656, Japan,
e-uchiyama@g.ecc.u-tokyo.ac.jp,
home page: http://www.euchiyama.jp
[2] Osaka University, 1-3, Machikaneyama-cho, Toyonaka-shi, Osaka, 560-8531, Japan,

1 Background

Fall and consequent fractures make elderly frailty and lead them to use a nursing cares. Robinovitch[1] found that elderly people in care facilities fall by their incorrect shifts of center of motions. On the other hand, falls in homes are not well surveyed due to difficulties of studying as keeping their privacy. Our group has conducted interview research to the elderly who had experienced hip fractures after their falls, and pointed out that repetitive turns during going from/to toilet may be a trigger of losing balance and one of causes of falls[2]. From this point of view, adequate means to keep the home environments safe even if they once have experienced fall and fracture is required. Ueda[3] proposes the intervention ways to notice the patients of their fall risk when people discharged using their room plan. In this research, we aimed at proposing a risk estimation method that evaluates the elderly peoples' fall risk at their homes from motions from the view of the system stability. As the first step, we consider static standings and discuss its stability.

2 Related work and Method

We hypothesized that the elderly people's stability controls to unexpected disturbances turn to be unstable as they repeat turns (in other words, shake their heads). For the balance control in a stationary state we have already proposed a test to identify people's internal balance control parameters[4]. In this research, we first identify the control parameters in static state and examine stability and responsiveness of the system using the identified parameters.

3 Experiment and Result

We measured participants' joint positions and ZMP positions during motions using a motion capture system. The parameters of the controller was identified referring the proposed method in [4]. CoM/ZMP trajectories during test were analyzed. Also, median value of the CoM trajectory as the point to which the

data converge in the control system and responsiveness to the impulse input of the system using the identified parameters was analyzed. One set of examples of analysis is shown on Fig. 1.

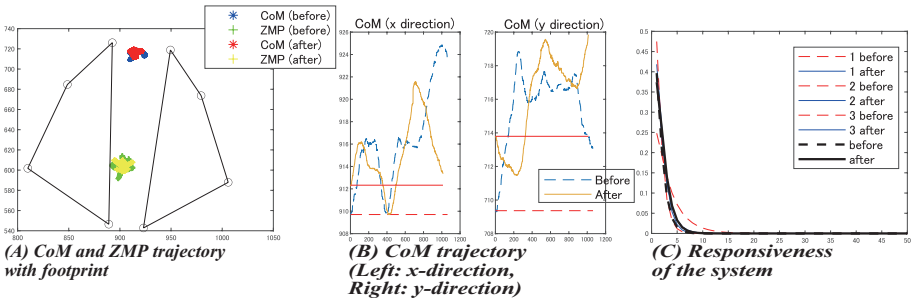

Fig. 1. The CoM trajectory and responsiveness of the controller was analyzed.

4 Conclusion

We proposed the scheme that evaluates the balance abilities of people as using parameters of the controller. To discuss the stability before and after the balance screening test, the responsiveness and the convergence of the CoM position after disturbances were analyzed. Since we only considers the static state at the current method, expanding this theory to the dynamic motions is the next step.

Acknowledgement

This research is supported by SECOM Science and Technology Foundation and KAKENHI(20K19858).

References

1. S.N.Robinovitch, F. Feldman, R. Schonnop Y. Yang, P.M. Lueng, T. Sarraf, J. Sims-Gould, and M. Loughin. Video capture of the circumstances of falls in elderly people residing in long-term care: an observational study. *The Lancet*, Vol. 381, pp. 47–54, 2013.
2. BK.Son, M. Akishita, E. Uchiyama, S. Imaeda, S. Taniguchi, Y. Sumikawa, S. Unyaporn, T. Matsubara, S. Tanaka, T. Tanaka, T. Otsuki, J. Okata, and K. Iijima. Multiple turns: Potential risk factor for falls on the way to the toilet. *Geriatrics & Gerontology International*, Vol. 19, pp. 1293–1295, 2019.
3. T. Ueda, Y. Higuchi, G. Hattori, H. Nomura, G. Yamanaka, A. Hosaka, M. Sakuma, T. Fukuda, T. Fukumoto, and T. Nemoto. Effectiveness of a tailored fall-prevention program for discharged older patients: A multicenter, preliminary, randomized controlled trial. *International Journal of Environmental Research and Public Health*, Vol. 19, No. 3, 2022.
4. E. Uchiyama, W. Takano, Y. Nakamura, T. Tanaka, and K. Iijima. Head shaking test: Human balance ability evaluation test by estimating control parameters for fall preventions. *The 6th Jc-IFToMM International Symposium*, 2023(to be published).

Parasitic Motions of a Delta Parallel Continuum Robot

Oscar Altuzarra, Mónica Urizar, Alfonso Hernández, and Enrique Amezua

University of the Basque Country UPV/EHU,
Torres Quevedo s/n, Bilbao 48013, Spain
Contact author: monica.urizar@ehu.eus

One of the most successful designs of a Lower Mobility Parallel mechanisms is the family of translational parallel mechanisms called Delta. The articulated parallelogram used in each limb introduces a constraint on the rotation of the end-effector about the normal to the parallelogram's plane, generating a coupled restriction of the three possible rotations, i.e. a pure translational motion of the end-effector. One side of the parallelogram is attached to the end-effector while the other one is translated with an actuator of different types, configuring the vertical or horizontal Delta, Keops-Delta and rotational Delta.

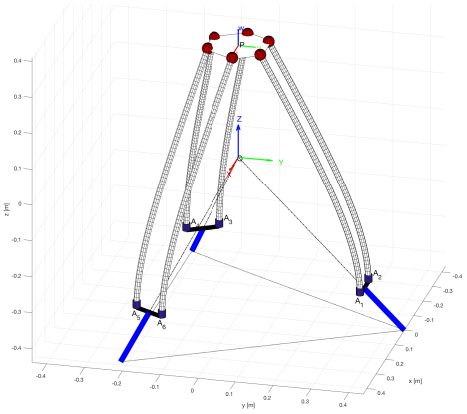

Fig. 1. Flexible Keops-Delta $3\underline{P}FFSS$ with Cosserat Rods

In order to design a flexible alternative to those translational mechanisms we have to bear in mind that *hard* geometric constraints are not possible in such flexible devices. By introducing flexible parallelograms, as shown in Fig. 1, the motion of the end-effector is not fully restricted to avoid rotations due to the flexibility of the rods. The aim of this contribution is to show the design process to get a quasi-translational behaviour of the system over a certain workspace under a certain range of loads by selecting appropriate dimensions of the system.

The $3\underline{P}FFSS$ Delta is a coupled mechanism of flexible rods, the rigid end-effector being connected to 3 parallelograms formed by flexible rods, which are

attached to the end-effector by spherical joints at their distal-ends B_i while the proximal-ends A_i are clamped to a rigid segment, with clamping orientation to be kept in vertical direction. These proximal segments are directly translated by actuators, in the Keops-Delta of Fig. 1 being placed on a pyramidal scheme.

The *FK* consists of determining the pose of the end-effector, i.e $\mathbf{p}_{\mathcal{P}}$ and the quaternion $\tilde{\mathbf{e}}$, when input values for each rod ρ_i and a load are imposed [1]. Guess values are required to start a boundary value problem on a vector of 25 geometric and static equilibrium residuals. A Newton method is used in the shooting method, requiring the evaluation of a Jacobian of the residue vector with respect to the problem's variables. After each iteration, guess values are updated and the process starts again until residuals' values are below a specified tolerance. In Lower Mobility Parallel Continuum Mechanisms, output components are obtained without any distinction on whether they are *principal* or *parasitic*. However, for the *IK* it is essential to assess appropriately which components are the *principal* ones. We will show that some translational and rotational ellipsoids can be found to achieve this target. Then, these output components are imposed in the *IK* while the *parasitic* ones are unknowns. Once these Kinematic problems are solved, a workspace and singularity analysis [2] can be performed.

Experimental validation is performed on a prototype of the Keops-Delta. An actuators' platform was designed with 3 linear guides controlled by stepper motors. A system was developed for the electronic control, which includes a MATLAB GUI application that communicates through a serial port with a microcontroller, allowing the control implementing *FK* and *IK* solutions. For measuring the parasitic rotational outputs, the MMA8451Q three-axis accelerometer sensor is used. This sensor can detect accelerations on the x, y, and z axes and has a digital sensitivity of 4096 counts per g. The data is collected at 14-bit resolution, and the analog output is converted to digital information using an ADC before being analysed by a microcontroller. This analysis aids in the determination of an object's orientation using a straightforward trigonometric algorithm.

Acknowledgments

The authors wish to acknowledge the financial support received from the Spanish Government through the Ministerio de Ciencia e Innovación (Project PID2020-116176GB-I00) financed by MCIN/AEI/10.13039/501100011033 and the support for the research group through Project IT1480-22 provided by the Departamento de Educación from the Regional Basque Government.

References

1. Black, C.B.; Till, J. and Rucker, D.C.: Parallel Continuum Robots: Modeling, Analysis, and Actuation-Based Force Sensing. IEEE Transactions on Robotics. 34, 29-47 (2018) 10.1109/TRO.2017.2753829
2. Briot,S. and Goldsztejn, A.: Singularity Conditions for Continuum Parallel Robots. IEEE Transactions on Robotics. 38, 507-525 (2022) 10.1109/TRO.2021.3076830

Designing Planar Mechanisms with the Software Mechanism Developer (MechDev)

Vincent Brünjes[1], Thomas Knobloch[1], Takahiro Aruga[2], Mathias Hüsing[1], Burkhard Corves[1]

[1] Institute of Mechanism Theory, Machine Dynamics and Robotics, RWTH Aachen University, Eilfschornsteinstraße 18, 52062 Aachen, Germany
[2] Iwatsuki Lab., Tokyo Institute of Technology, Room #351, Ishikawadai-1 Building 2-12-1, Ookayama, Meguro-ku, 152-8550 Tokyo, Japan
huesing@igmr.rwth-aachen.de

1 Extended Abstract

The Institute of Mechanism Theory, Machine Dynamics, and Robotics (IGMR) at RWTH Aachen University is currently developing the software "Mechanism Developer" (MechDev) for the analysis and synthesis of planar mechanisms with one or more degrees of freedom. The focus of the development is to create a powerful tool for engineers that distinguishes itself from existing software solutions not only by its performance but also by its intuitive operation. As a goal, the software should be made accessible also to those who do not have a background in mechanism theory.

At the IGMR different contributions have already been made towards the kinematic calculation of planar linkages [2; 6], the synthesis and analysis of cam mechanisms [1; 3; 4], and the analysis of gear mechanisms [5]. This contribution focuses on the usage of the software to these ends. For this purpose, the current range of functions of MechDev is first summarized. Subsequently, these functions are validated with an example mechanism.

The current scope of functions includes the kinematic analysis of planar linkages consisting of revolute and prismatic joints, cam followers, as well as the kinetostatic analysis for the calculation of drive torques induced by gravitational force, external forces, and spring-damper elements. Joint friction can also be considered. In addition, MechDev offers the function to synthesize cam wheels by specifying the desired output motions or analyze cam mechanisms based on imported cam geometries. The specification of such output motion, which provides the basis for cam wheel synthesis, can also be used for the motion design of servo motors. Furthermore, both the development and analysis of gear and gear-coupler mechanisms is possible.

The functions mentioned before, as well as further features, are presented using the cutting mechanism included in [7] as an example. A screenshot using the software

is shown in Fig. 1 (a). Given the available methods of interaction with MechDev (shown in Fig. 1 (b)) it is possible to optimize the mechanism interactively by drag-and-drop. The presentation shows the complete design process, from the definition of the mechanism in MechDev to the interactive optimization of the drive torque.

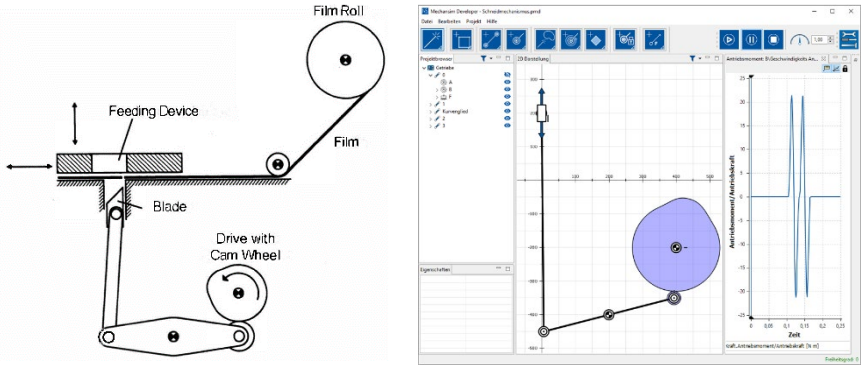

(a) (b)

Fig. 1. A cutting mechanism from VDI 2142-3 [7] (a) and a screenshot from MechDev (b).

References

1. Beckermann, A.; Müller, M.; Hüsing, M.; Corves, B., Analytical Kinematic Analysis of Cam Mechanisms in MechDev, In: Uhl, T. (Ed.), Advances in mechanism and machine science, Cham, Switzerland: Springer Nature Switzerland AG, 2019, ISBN 978-3-030-20130-2, S. 429–438.
2. Corves, B.; Huesing, M.; Müller, M., A Model-View-Controller based Software Approach for the Interactive Design of Planar Mechanisms, In: Zhang, X.; Wang, N.; Huang, Y. (Ed.), IFToMM Asian Mechanism and Machine Science, Bengaluru, India, 2018.
3. Corves, B.; Huesing, M.; Müller, M.; Beckermann, A., Analyse von Kurvengetrieben in MechDev, In: Gössner, S. (Ed.), Tagungsband 13. Kolloquium Getriebetechnik, Fachhochschule Dortmund, 18. - 20. September 2019, Berlin: Logos Berlin, 2018, ISBN 383254979X.
4. Müller, M.; Hüsing, M.; Beckermann, A.; Corves, B., Linkage and Cam Design with Mechanism Developer (MechDev), In: 25th Jc-IFToMM Symposium, Kanagawa, Japan, 2019.
5. Knobloch, T.; Brünjes, V.; Hüsing, M.; Corves, B., Analyse von Koppel-, Kurven-, Räder- und Räderkoppelgetrieben mit Mechanism Developer (MechDev), In: Berger, M., Corves, B., Lüth, T. (Ed.), Tagungsband Getriebetagung 2022, Technische Universität Chemnitz, 22. - 23. September 2022, Berlin: Logos Berlin, 2022, ISBN 978-3-8325-5552-8.
6. Müller, M.; Mannheim, T.-P.; Hüsing, M.; Corves, B., MechDev – A new Software for Developing Planar Mechanisms, In: Kecskeméthy, A. et al. (Ed.), Third Conference on Interdisciplinary Applications in Kinematics, Lima, Peru, 2018, ISBN 978-3-030-16422-5, S. 151–158.
7. VDI 2142, Auslegung ebener Kurvengetriebe - Praxisbeispiele, Norm, Verein Deutscher Ingenieure, Berlin: Beuth Verlag GmbH, 2013.

Kinematic Modeling and Analysis of a New Hybrid Seven-Bar Linkage Mechanism

Amandyk Tuleshov[1], Recep Halicioglu[1,2], and Moldir Kuatova[1]

[1] U.Joldasbekov Institute of Mechanics and Engineering, Almaty, Kazakhstan
[2] Turkish Machine Theory Association, Turkey

1 Introduction

More than 50% of forming materials processes in the engineering industry are carried out using forging machines, including crank presses, due to some advantages such as high productivity, the possibility of various types of stamping, and high precision stamping in the extreme position of the working body. One of the most essential directions in developing crank presses is their multi-link linkages. Using multi-link mechanisms is a reasonably effective way to implement the requirements of stamping technology. In addition, most interest has been focused on their driving systems. Because hybrid mechanisms are driven by both a constant-speed and servo motor, some problems are experienced, and it is necessary to solve these problems. This study aims to present a new hybrid seven-bar linkage mechanism with related kinematics modeling and analysis. The mechanisms' kinematics is studied with inverse problem. This mechanism provides flexible motion by using a servo motor with a lower power capacity. In addition, the linkage flexibility is achieved using a rocker pair that provides programmable motion output.

2 Kinematic modeling and analysis

2.1 Mechanism configuration

A hybrid seven-bar linkage mechanism is presented in Figure 1. The mechanism is composed of: crank (r), links (l, d), slider (D), and coulisse mechanism ($C(x_c, y_c)$). All joints are revolute. The crank and coulisse mechanism are driven by a constant speed motor (CSM) and a servo motor (SM). In the Bottom dead center point (BDC) of the slider, r and l are lined up at one angle, and d and slider are lined up in a straight line. The TDC is the top dead center point. The coulisse is a mechanical linkage that facilitates the conversion of a rocking or rotational motion into a reciprocating motion and vice versa. The main advantage of the coulisse mechanism is that it provides

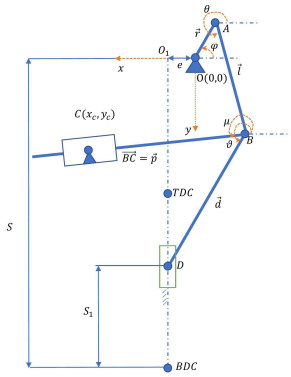

Fig. 1. Schematic illustration of a new hybrid seven-bar linkage mechanism

a reasonably high speed of slider reverse stroke. In addition, the coulisse mechanism can transmit much less effort than the crank mechanism. The coulisse mechanism is connected with the slider through an adjusting link BC (p) to tune its motion. S_1 is the slider displacement.

2.2 Kinematic analysis

In this section, the inverse kinematics equations of a 2DOF hybrid mechanism with a seven-bar configuration are obtained (Figure 1). Two loop closure equations are considered and written in vector form. By resolving them into x and y components and differentiating, can be obtained the p representing the servo motor's linear displacement, velocity, and acceleration. In inverse kinematics analysis, the input values are φ and S_1 variables, and θ, μ, φ, $\vartheta = \mathrm{f}(\varphi, S_1)$.

$$p = \pm\sqrt{(x_c - r\cos(\varphi) - l\cos(\theta))^2 + (y_c - r\sin(\varphi) - l\sin(\theta))^2} \quad (1)$$

$$\dot{p} = r\dot{\varphi}\sin(\varphi - \mu) + l\dot{\theta}\sin(\theta - \mu) \quad (2)$$

$$\ddot{p} = p\dot{\mu}^2 + r\ddot{\varphi}\sin(\varphi - \mu) + r\dot{\varphi}^2\cos(\varphi - \mu) + l\ddot{\theta}\sin(\theta - \mu) + l\dot{\theta}^2\cos(\theta - \mu) \quad (3)$$

3 Motion Applications

The angular velocity of CSM is a constant value (positive direction $1,256 rad/sec$). The slider stroke is 30 mm. The designed dwell motion with kinematic specifications is obtained. By providing inverse kinematics analysis, we received the kinematics characteristics of SM.

4 Kinematic Modeling

The proposed hybrid mechanism model was developed by solving motion equations in MATLAB.

5 Conclusion

In this study, a new hybrid seven-bar linkage mechanism was presented with related kinematics modeling and analysis. It is studied with inverse problem This proposed mechanism configuration provides flexible motion and lower power capacity by using a servo motor. The linkage flexibility is achieved using a rocker pair that provides programmable motion output. In this way, different motion scenarios can be implemented.

6 Acknowledgment

This research was supported by the Funding of the Kazakhstan Ministry of Science and Higher Education (Project No. AP19577094). We also would like to sincerely thank the Joldasbekov Institute of Mechanics and Engineering for providing resources.

3-U<u>C</u>U: a new parallel robot with 6 degrees of freedom

Chedli Bouzgarrou[1] and Khaled Assad Arrouk[2]

[1] Université Clermont Auvergne, CNRS, Clermont Auvergne INP,
Institut Pascal, Department M3G, 63000 Clermont-Ferrand, France
chedli.bouzgarrou@sigma-clermont.fr
[2] Al-Baath University, The Faculty of Mechanical and Electrical Engineering,
Department of Mechanical Design and Production, Homs, Syria
kharrouk@albaath-univ.edu.sy

Keywords: mechanism synthesis, linear – angular transmission, parallel robots, decoupled motions.

1 Introduction

Parallel kinematics Machines (PKMs) or robots have been widely studied during the past three decades. The majority of known PKMs have only one actuated joint for each limb, preferably a joint close to the fixed base. In contrast, robots with more than one actuated joint per limb have attracted less interest. This is mainly due to the loose of some benefits of PKMs such as mobile mass reduction. In this paper, we introduce a transmission device that enables the full actuation of the two degrees of freedom (DOFs), translation and rotation, of the equivalent of a cylindrical joint [1]. Such a technology makes possible the actuation of two DOFs of a manipulator limb in a compact an efficient way. Thus, new generic mechanism architectures can rise based on fully actuated cylindrical joints such as the *3-<u>C</u>RS* manipulator [2]. Another interesting robot architecture is the *3-U<u>C</u>U* that we present for the first time in this paper, with partially decoupled motions.

2 Linear – angular transmission

We propose a linear – angular transmission devise described by the kinematic diagram of **Fig. 1a**. This devise uses as inputs 2 screws (1a) and (1b), with parallel axes, connect to the support (0) by two revolute joints. Two nuts (2a) and (2b) are mounted on each of these screws and each of them is connected by a revolute joint to the carriage (3). The axes of the revolute joints between the carriage (3) and the nuts (2a) and (2b) are parallel to the axes of the screws. The carriage (3) is connected by a prismatic joint to the support (0) along an axis parallel to those of the screws. An output shaft (4), is connected by a revolute joint to the carriage (3) whose axis is also parallel to that of the screws. Each nut is connected to the output shaft (4) by a transmission element such as a belt (5a and 5b), a chain or a gear train, so as the angular speed of the nuts (2a or 2b) and that of the output shaft (4), with respect to the carriage (3), are proportional. Such a design allows translation and a rotation, of parallel axes, of the output shaft (4) with

respect to the support (0). Therefore, the connection between the output shaft (4) and the support (0) is then equivalent to a motorized cylindrical joint. **Fig. 1b** gives an illustration of the mechanical design of the proposed device, with gear transmissions, integrated in a robot limb. The transmission is symmetric and generates independent output translation and rotation.

3 3-U<u>C</u>U design

If we use the transmission device presented above within a limb of a parallel mechanism, we have two actuated DOFs in this limb. In order to synthetize parallel robot architecture with such a device, we can use Gogu's mobility formulae [3] to determine the possible remaining joint types and their arrangements to obtained the required DOFs of the limb. Therefore, to have a PKM with 6 DOMs and 3 limbs, we need 6 DOFs per limb. One of possible solutions is to add two universal joints as we propose for the *3-U<u>C</u>U* parallel robot depicted in **Fig. 1c**. Moreover, in order to achieve motion decoupling between translation and rotation, the three *U*-joints connecting the limbs to the mobile platform must have all their axes concurrent at one point, the center of the mobile platform (MPF). Therefore, only translational motorized joint variables control the position of the MPF. For a given position of the MPF, only rotational motorized joint variables control the orientation of the MPF such as a spherical robot. In addition, the proposed design reduces bending loading since each isolated limb is attached to the rest of the mechanism by *U*-joints at both ends.

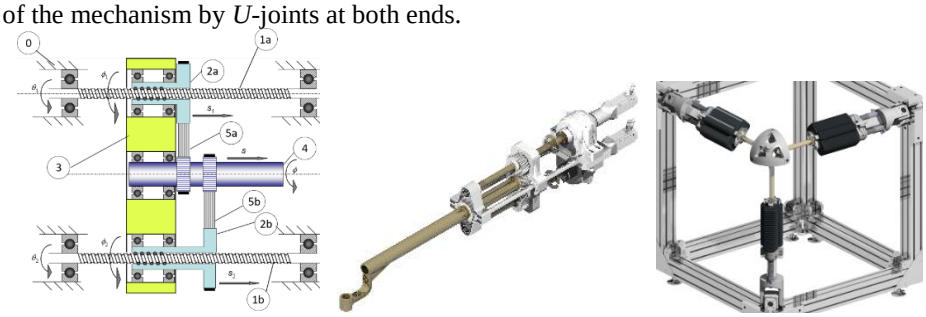

(a) (b) (c)

Fig. 1. Linear – angular transmission device (a), CAD model of the transmission device integrated in *3-U<u>C</u>U* limb, (c) CAD model of the *3-U<u>C</u>U* robot.

References

1. Bouzgarrou, C.: Mechanical transmission device and system comprising such a device. Patent EP3507524, (2019).
2. Bouzgarrou, C., Koessler, A., Bouton, N.: Singularity analysis and reconfiguration mode of the 3-CRS parallel manipulator, IEEE International Conference on Robotics and Automation (ICRA), Paris, France, (2020).
3. Gogu, G.: Structural synthesis of parallel robots, Dordrecht: Springer Netherlands (2008).

Survey of Graphic Software for teaching Mechanism Synthesis using Path Curvature Theory

Mohan Nagrurkar[a], P. S. Deole[b], P. B. Shiwalkar[c]

[a,b,c] Shri Ramdeobaba College of Engineering and Management, Nagpur-13, India
shiwalkarpb1@rknec.edu

1 Introduction and need

Wider choice of rigid body mechanisms for creating compliant mechanisms is overdue [1]. Approximate straight line linkages, as a family, are focused in this discussion. Inflection Circle (IC), on its' own, and in unison with the Cubic of Stationary Curvature (CSC) are two main strengths for teaching Mechanism Synthesis. Today there are negligible takers for these concepts [2]. Using commonly visible applications, interest in these concepts can be rekindled [3]. To achieve this, eight different graphic softwares are compared for usability towards this goal.

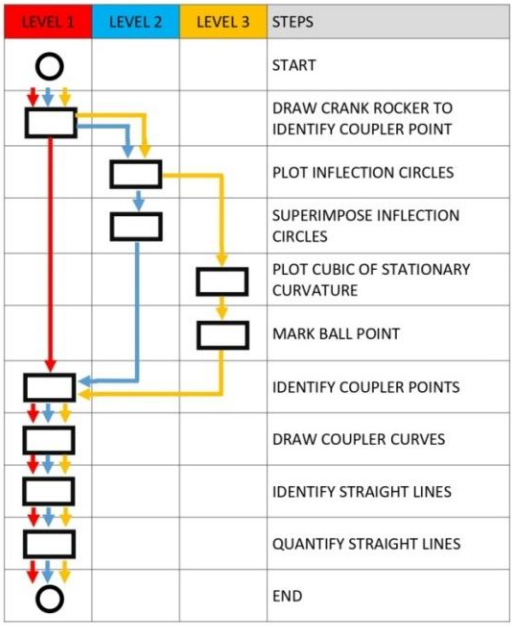

Fig. 1. Graded levels of tracing and quantification of straight paths

2 Methodology

Eight listed graphic software suitable for teaching the concepts at three levels of understanding are in Fig.1. Table 1 shows only seven features out of twenty techno-commercial features. Concepts of level 3 (yellow path) are more involved compared to level 1 (red path) and level 2 (blue path). Six features of kinematic analysis (not included here) are noted to be of help in further research.

Table 1. Abridged set of features listed for used softwares

FEATURES ↓ SOFTWARES →	Auto-CAD	Mech Ana-lyzer	SAM 8.2	Link-age	Ad ams-.	GI M	An alytix ing	Model
Input [Lengths (L)/Coordinates (C)/Both(B)]	B	L	C	L	L	B	L	B
Can it draw ICs at various crank positions	✓	-	-	-	✓	✓	✓	-
Can it draw a cubic of stationary curvature?	✓	-	-	-	-	✓	-	-
Output [Graphical(G)/Coordinates(C)/Both(B)]	B	C	G	G	G	G	G	G
Export to AutoCAD (dwg)	✓	-	✓	✓	-	-	✓	✓
Export coupler curves values to Excel	✓	✓	✓	-	-	-	-	-
Mechanism Library	-	✓	✓	✓	-	✓	-	-

3 Conclusion

With proper selection of the graphic software with appropriate background processing capacity, academic interest in the apparently complex concepts of IC and CSC can be rekindled to reap the proper benefits.

References

1. Zhao K. and Schmiedeler J.P.: Using Rigid-Body Mechanism Topologies to Design Path Generating Compliant Mechanisms, Journal of Mechanisms and Robotics, February 2016, Vol. 8 (2016)
2. Torres-Moreno J., Giménez-Fernández A.: Carbone G. and Ceccarelli M., Kinematic and Dynamic Analysis of Old Mechanism by Modern Means, The 14th IFToMM World Congress, Taipei, Taiwan, October 25-30, 2015, DOI: 10.6567/IFToMM.14TH.WC.PS7.001 (2015)
3. Shiwalkar P.B. and Padole P.M.: Revisiting Inflection Circle Via Level Luffing Crane for Academic Revival, HMM 2022, HMMS 40, pp 255-265, doi:10.1007/978-3-030-98499-1_21 (2022)

Comparative Combustion Characteristics of Dimethyl Ether and Diesel Fueled Engines

Shanti Mehra, Hardikk Valera, Vikram Kumar, Avinash Kumar Agarwal*
Engine Research Laboratory, Department of Mechanical Engineering
Indian Institute of Technology Kanpur, Kanpur-208016, India
*Corresponding Author: akag@iitk.ac.in

1 Introduction

Compression ignition (CI) engines are used for various functions ranging from transportation and power generators to agriculture equipment and machinery. Conventional diesel engines are efficient and have good fuel economy but have higher emissions of nitrogen oxides (NO_x) and particulate matter (PM). DME is a promising fuel for CI engines since it has a high cetane number and an inbuilt oxygen atom in its chemical structure. The chemical properties of DME lead to a shorter ignition delay and almost negligible soot emissions. Therefore, this study conducted experiments on a direct injection, mechanical injector type, in-line three-cylinder CI engine. The test fuels were DME and diesel. DME exists as a gas at normal room temperature conditions and is liquified when pressurized above 5 bar [1]. DME has a high vapor pressure, low lubricity, and a lower calorific value. Therefore, the fuel injection system was modified for the injection of DME into the engine cylinders. The engine speed was fixed at 1200 rpm, and the engine load was varied from no load to 6.47 bar BMEP.

1.1 Fuel Line Pressure

DME has a low liquid density, higher vapor pressure, and higher compressibility. Therefore, the pressure build-up in the high-pressure fuel lines differs from that of diesel.

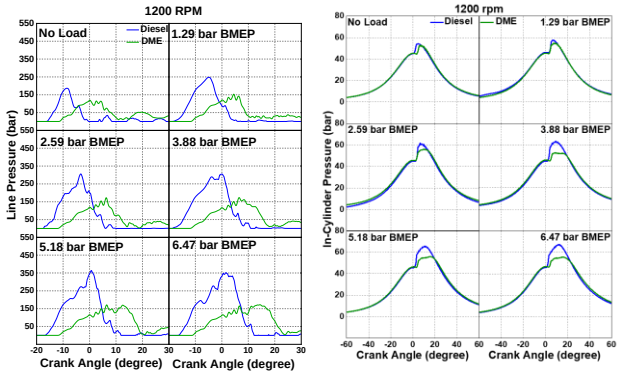

(a) **(b)**

Fig. 1 (a) Fuel Line Pressure **(b)** In-cylinder pressure vs crank angle for 1200 rpm engine speed

It can be seen in Fig.1(a) that DME had a longer injection delay and injection duration than diesel. This was because the quantity of DME injected was almost 1.5 times diesel to maintain the same energy density input as diesel. Also, DME had pressure oscillations and a higher residual pressure in the high-pressure line because the higher compressibility of DME leads to more energy storage in compressed DME during its injection [2].

1.2 Combustion Characteristics

The in-cylinder pressure was lower for DME than diesel because of the lower calorific value of DME. Also, the latent heat of vaporization is higher for DME [3]. The peak of HRR was higher for diesel than DME in the premixed combustion phase. The sharp rise in the CHR curve was delayed for DME. This was due to the longer injection delay for DME. The CHR was higher for DME after the steep rise. The combustion duration was shorter for DME.

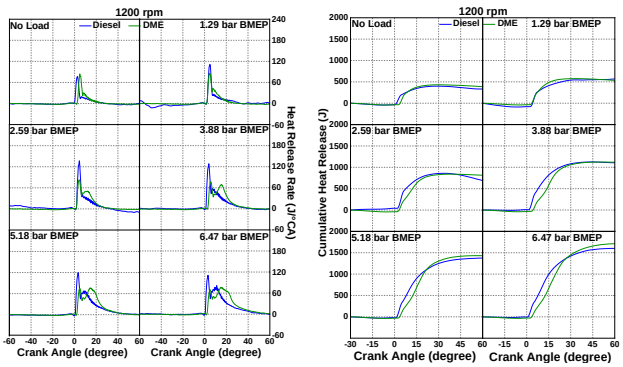

(a) (b)

Fig. 2 (a) HRR and **(b)** CHR vs crank angle for 1200 rpm engine speed

The mixing-controlled phase dominated DME's combustion. The lower calorific value of DME led to the injection of higher fuel quantity, leading to an increased injection delay. However, the shorter ignition delay of DME due to its higher cetane number led to the accumulation of lower fuel quantity and, therefore, lower heat release during the premixed combustion phase. Additionally, the DME-fuelled engine had higher thermal efficiency, lower combustion noise, and almost smokeless combustion, thus proving to be a promising alternative to conventional diesel engines.

References

1. Arcoumanis C, Bae C, Crookes R, Kinoshita E. The potential of dimethyl ether (DME) as an alternative fuel for compression-ignition engines: A review. Fuel, 87(7):1014-30. (2008)
2. Kapus P, Ofner H. Development of fuel injection equipment and combustion system for DI diesel engines operated on dimethyl ether. SAE Technical Paper (No. 950062) (1995)
3. Sorenson SC, Glensvig M, Abata DL. Dimethyl ether in diesel fuel injection systems. SAE Transactions.; 438-49 (1998)

Design and Efficiency Analysis of 3K Paradox Planetary Gear Drives

Qi-You Zhuang [1] and Shyi-Jeng Tsai [1] [0000-0002-7874-7943]

[1] National Central University, Jhong-Li District, 320 Taoyuan City320, Taiwan
sjtsai@cc.ncu.edu.tw

1 Introduction

In multi-stage planetary gear mechanisms, the so-called "paradoxical planetary gear mechanism" is commonly used for high speed ratios. The 3K-PPGT type often employs two ring gears with small tooth differences and multiple identical planetary gears meshing with them. However, this type of planetary gear mechanism presents a complex geometric calculation problem because the planets mesh simultaneously with two different sized ring gears. On the other hand, the PPGT mechanism generates backflow of power inside the mechanism, which increases power loss and causes a decrease in transmission efficiency. When used as a speed increasing mechanism, it can even result in self-locking. The gearing data used in this study are presented in **Table 1**.

Table 1. Gearing data of study case.

	S	A1	P1	P2	A2
Tooth number	25	-47	11		-41
Speed ratio			20.68		
Number of planets			6		
Module			2		
Pressure angle [deg]	20	20	20		20
Face-width [mm]	40	20	40		20
Center distance [mm]			36		

2 Non-Standard Profile Design

In this study, the direct tooth profile design method was adopted by utilizing the concept of complementary tooth profiles. The design parameters were selected as the tooth crown height and the working addendum circle tooth thickness, while the standard tooth cutting tool system was excluded, and the design was directly performed using involute tooth profiles. Design limitation equations, including tooth tip interference, tooth flank/root interference, and contact ratio, were established based on gear pairs, and design charts were created, Fig.1. Then, the geometric parameters of the gear were obtained based on the optimal load capacity relationship between gear pairs using the tooth root strength calculation formulae in ISO 6336. The profiles are shown in Fig.2.

3 Efficiency Calculation

In this study, the power loss was calculated using relationships such as power balance and torque balance, and an efficiency analysis matrix for multi-stage planetary gear mechanisms was established. On the other hand, based on the planetary gear set analysis model established by Tsai et al. [1, 2], it was expanded into a load calculation matrix

for the PPGT, and the loads and corresponding gear torques affected by friction on each contact tooth pair were calculated, and the instantaneous meshing efficiency and transmission efficiency of the mechanism were derived. In the study, the efficiencies for both reducer and increaser applications were analyzed. Fig.3 and Fig.4 show the power flow and instantaneous efficiency analysis results with different friction coefficients μ for increaser application, respectively [3].

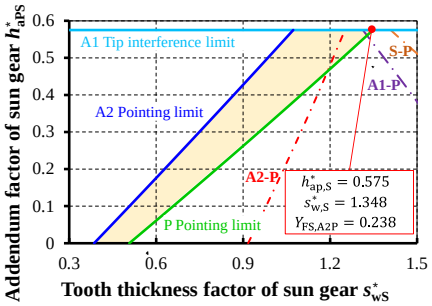

Fig. 1. Design chart of profile parameter

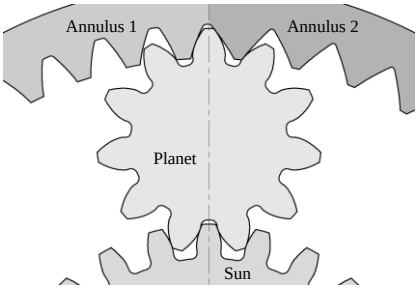

Fig. 2. Designed Profiles

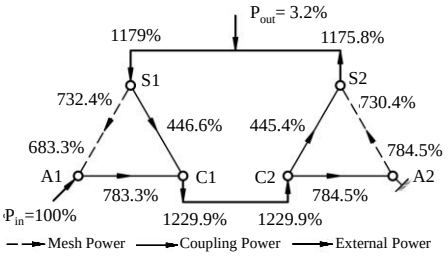

Fig. 3. Power flow and magnitude

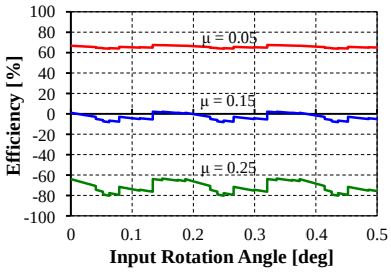

Fig. 4. Instantaneous efficiency: increaser

4 Conclusion

In this study, the direct tooth profile design method was used to successfully solve the design problem. From efficiency analysis results, the variation amplitude of the meshing efficiency during operation and reduces the impact of the direction change of the friction force can be reduced, when PPGT with sequential mesh phase. The efficiency of the 3K-type mechanism is about half that of the traditional serial planetary gear mechanism, and the reduction will be greater in the case of acceleration. When the friction coefficient is greater than 0.15, the gear mechanism will be self-locked.

References

1. Tsai, S.-J. and Zhuang, Q.-Y.: Analytical approach for load sharing analysis of a differential type three-stage planetary gear drive. In proceedings of MPT2017-Kyoto, (2017).
2. Tsai, S.J., Huang, G.-L. and Ye, S.-Y.: Gear meshing analysis of planetary gear sets with a floating sun gear. Mechanism and Machine Theory, 84 (2015)
3. Müller, H. W. Die Umlaufgetriebe (The Planetary Gear Drives). Springer-Verlag Berlin Heidelberg (1998).

Gear tooth topology modification with considering honing wheel dressing in power gear honing

Quoc-Duy Nguyen [1][0000-0001-7418-8884] and Yu-Ren Wu [2][0000-0001-5856-2944]

[1,2] National Central University, Zhongli District, Taoyuan City, Taiwan (R.O.C)
yurenwu@ncu.edu.tw

Abstract. The dressing process in the power gear honing process is critical to correct and reshape a honing wheel with abrasion. However, there is a marked lack of considering this process. In view of this, this study proposes a closed-loop gear tooth topology modification method for power gear honing, considering both dressing and honing processes. A dressing gear is generated by the modified rack cutter, which is utilized to reshape the honing wheel profile and then applied to finalize the work gear. The expected tooth modification is achieved by the additional motion derived from the combination of the sensitivity matrix and the Levenberg-Marquardt algorithm. A numerical result of a double-crowned helical gear tooth is presented to prove the practicality of the proposed model.
Keywords: gear honing, dressing process, topology modification.

1 Introduction

The gear-honing method enables high production efficiency [1]. Although there are many previous studies evaluating the advantages or exploring methods to achieve crowned gear tooth surfaces during honing process [2-5], however, none of them investigated the issue of honing wheel dressing. Therefore, this study proposes a method of gear tooth topology modification with considering dressing and honing processes for CNC power gear honing.

2 Proposed method

As shown in **Fig. 1**, the modeling procedure in this research is illustrated. The mathematical model of dressing and honing processes are established based on a CNC gear honing machine. A dressing gear with a barreled shape tooth is used to reshape the honing wheel, which is then used to hone the work gear tooth to achieve the required tooth modification by adding additional motions in the machining axes of the CNC machine. A sensitivity matrix relating to the dressed amount and the additional motions is constructed to determine the corresponding values of dressing and honing settings for the required work gear tooth profile using the Levenberg-Marquardt algorithm. To see the geometry difference between the corrected honing wheel and the modified work gear, their tooth surface topographies with the normal deviation are presented.

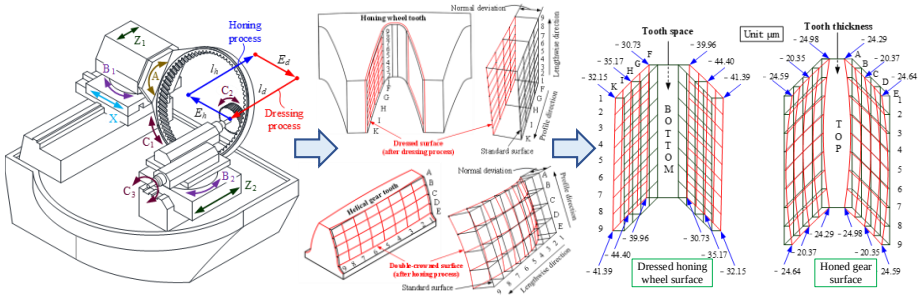

Fig. 1. Procedure of gear tooth modification considering both dressing and honing processes.

3 Numerical examples and discussions

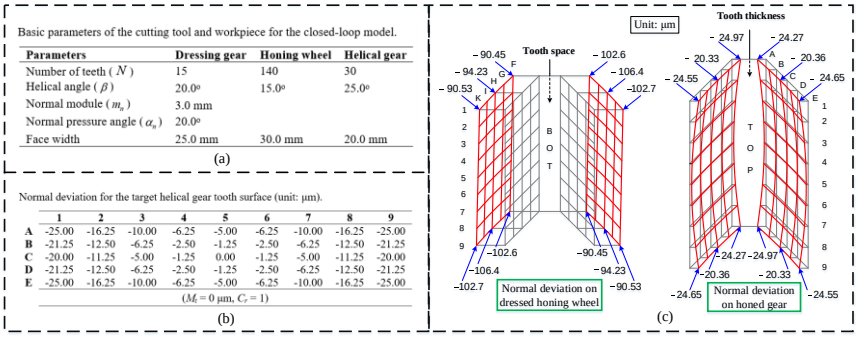

Basic parameters of the cutting tool and workpiece for the closed-loop model.

Parameters	Dressing gear	Honing wheel	Helical gear
Number of teeth (N)	15	140	30
Helical angle (β)	20.0°	15.0°	25.0°
Normal module (m_n)	3.0 mm		
Normal pressure angle (α_n)	20.0°		
Face width	25.0 mm	30.0 mm	20.0 mm

(a)

Normal deviation for the target helical gear tooth surface (unit: μm).

	1	2	3	4	5	6	7	8	9
A	-25.00	-16.25	-10.00	-6.25	-5.00	-6.25	-10.00	-16.25	-25.00
B	-21.25	-12.50	-6.25	-2.50	-1.25	-2.50	-6.25	-12.50	-21.25
C	-20.00	-11.25	-5.00	-1.25	0.00	-1.25	-5.00	-11.25	-20.00
D	-21.25	-12.50	-6.25	-2.50	-1.25	-2.50	-6.25	-12.50	-21.25
E	-25.00	-16.25	-10.00	-6.25	-5.00	-6.25	-10.00	-16.25	-25.00

($M_t = 0$ μm, $C_r = 1$)

(b)

(c)

Fig. 2. (a) basic inputs; (b) normal deviation for the target work-gear tooth surface, and (c) calculated results of normal deviation on the honing wheel and work-gear tooth surfaces.

A numerical example is presented to show how to achieve a double-crowned work-gear tooth surface using the proposed method. As shown in **Fig. 2(c)**, the honing wheel is approximately dressed by 90~107 μm, and those normal deviations at corners on the double-crowned gear surface are very close to the target crowning value of -25.00 μm. The result proves the practicability of the proposed method.

References

1. D.T. Mehta and M.G. Rathi, A review on internal gear honing, Int. J. Eng. Res. Technol. 2(5) (2013) 973-983.
2. V.Q. Tran and Y.R. Wu, A novel method for closed-loop topology modification of helical gears using internal-meshing gear honing, Mech. and Mach. Theory 145 (2020) 103691
3. V.Q. Tran and Y.R. Wu, Dual lead-crowning for helical gears with long face width on a CNC internal gear honing machine, Mech. and Mach. Theory 130 (2018) 170-183.
4. J. Han, Y.G. Zhu, L. Xia, and X.Q. Tian, A novel gear flank modification methodology on internal gearing power honing gear machine, Mech. and Mach. Theory 121 (2018) 669–682

Load sharing in planetary transmissions affected by eccentricity and index errors in the sun

J. Sanchez-Espiga[1[0000-0001-8413-3561]] A. Fernández-del-Rincón[1[0000-0001-6999-0776]], M. Iglesias[1[0000-0003-3557-0647]], A. De-Juan[1[0000-0003-3583-1624]], P. García[1[0000-0003-4856-3155]], G. Huo[1,2], F. Viadero [1[0000-0002-6483-1802]]

[1] Universidad de Cantabria, Santander, Cantabria, 39005, Spain
[2] Harbin Institute of Technology, Harbin, China
viaderof@unican.es

1 Introduction

Planetary gear transmissions are a crucial component in the power transmission of systems such as vehicles, aircrafts [1] and wind generators [2]. This importance comes from their advantages compared to other gear transmissions, the power density, compactness, robustness and coaxiality between inlet and outlet. These transmissions also provide the opportunity of increasing the number of planets to augment its power density. However, the number of elements that compose the transmission bring more possibilities for manufacturing errors [3], [4] too. Thus, this work focuses on the impact some of those manufacturing errors have in the performance of the planetary transmissions where they belong.

The errors that are considered in this precise work are time-dependent errors present in the sun gear. More precisely, these errors are eccentricity and index errors.

Therefore, this work focuses on the impact these errors have the in the geometry of the contact between the sun gear and the planets that surround it. Then, these changes have an impact directly on the transmission's load sharing.

2 Load sharing

In this work, a 2D hybrid model developed by the authors following Vedmar's proposal [5] and presented in [6] is employed to model the behavior of Equally Spaced In-Phase (ESIP) and Equally Spaced Sequentially Phased (ESSP) planetary transmissions.

This model uses a hybrid approach to solve the contact between gears and finds the balance in the transmission in order to be able to analyze the behavior of these transmissions under a series of working conditions.

3 Influence of the time dependent errors in the load sharing

The errors are modeled following a sinusoidal formulation, such as the one presented in [7]. This formulation agrees with the manufacturing process followed to cut the

gears. In addition, this formulation allows the comparison between the impacts of both errors in the same transmission.

Thus, the importance of this analysis comes from the impact that these errors have in the transmission's performance. Firstly, due to their nature this impact varies with time. Therefore, starting by the eccentricity error it means that the gear is not rotating with respect to its geometrical center, but at a distance of that point. As the gear rotates, this error is going to change its role, from tangential mounting error to radial error or a combination of both. Thus, these errors will change their importance in the load sharing [8] and modulations appear.

On the other hand, the index error refers to the difference between the actual position of a tooth and its ideal position. Therefore, the error will vary from generating and advancement to a delay in the contact between the sun gear and the planet i. Thus, there will be a modulation also in the load sharing ratio variation in the transmission due to this change.

References

[1] J. Kurzke, "Fundamental differences between conventional and geared turbofans," *Proceedings of the ASME Turbo Expo*, vol. 1, pp. 145–153, 2009.

[2] H. Aurrekoetxea and I. R. De Ocenda, "Experimental and theoretical study of load mesh factor for different boundary conditions in wind gearbox planetary stages," in *International Conference on Gears 2019*, VDI Verlag, 2019, pp. 835–844.

[3] A. Bodas and A. Kahraman, "Influence of Carrier and Gear Manufacturing Errors on the Static Load Sharing Behavior of Planetary Gear Sets," *JSME International Journal Series C*, vol. 47, no. 3, pp. 908–915, 2004.

[4] A. Kahraman, "Static Load Sharing Characteristics of Transmission Planetary Gear Sets : Model and Experiment," *Transmission and Driveline Systems Symposium*, no. 1, pp. 1–10, 1999.

[5] L. Vedmar and B. Henriksson, "A General Approach for Determining Dynamic Forces in Spur Gears," *Journal of Mechanical Design*, vol. 120, no. 4, p. 593, 1998.

[6] M. Iglesias, A. Fernandez del Rincon, A. de-Juan, A. Diez-Ibarbia, P. Garcia, and F. Viadero, "Advanced model for the calculation of meshing forces in spur gear planetary transmissions," *Meccanica*, vol. 50, no. 7, pp. 1869–1894, 2015.

[7] A. Fernández-Del-Rincón, M. Iglesias, A. De-Juan, A. Diez-Ibarbia, P. García, and F. Viadero, "Gear transmission dynamics: Effects of index and run out errors," *Applied Acoustics*, vol. 108, pp. 63–83, 2016.

[8] J. Sanchez-Espiga, A. Fernandez-del-Rincon, M. Iglesias, and F. Viadero, "Influence of errors in planetary transmissions load sharing under different mesh phasing," *Mechanism and Machine Theory*, vol. 153, p. 104012, Nov. 2020.

An Analytical Model for Power Skiving Process of Helical Face Gears

Khoe-Qui Le[1] and Yu-Ren Wu[1] [0000-0001-5856-2944]

[1] Department of Mechanical Engineering, National Central University, Taoyuan City 320317, Taiwan
yurenwu@ncu.edu.tw

Abstract. Nowadays, face gears are machined by gear shaping or gear hobbing. Several studies have been conducted on applying gear skiving processes to generate "straight-tooth" face gears. Even so, a skiving methodology to manufacture "helical-tooth" face gears is not proposed yet. This study proposes a mathematical model for manufacturing helical face gears using the power skiving process. A helical skiving cutter is generated using a corrected rack. The cutting path on the CNC machine is then adjusted by adding additional motions in forms of polynomials. A skiving simulation is performed to attain the face gear surface with the specified polynomial coefficients. The Levenberg-Marquardt algorithm and sensitivity matrix are employed to calculate the polynomial coefficients to attain the accuracy requirement of the gear surfaces. The numerical results have verified the practicability of the proposed method.

Keywords: Helical Face Gear, Power Skiving, Sensitivity Matrix.

1 Introduction

Power skiving is an efficient cutting process to continuously cylindrical gears [1]. In addition, many researchers studied the skiving process of spur face gears [2-4]. There lacks studies of applying the skiving process on helical face gear. In view of this, this paper presents the application of power skiving for generating helical face gear to improve the processing time and gear quality.

2 Mathematical model for generation of skiving cutter

Figure 1 shows an illustration of the skiving process used in this study. Based on a CNC skiving machine, a mathematical model of the face gear skiving process is established. A corrected rack is used to generate the power skiving, which is then used to manufacture the helical face gear by adding additional movements in the machining axes of a CNC machine. The Levenberg-Marquardt algorithm and sensitivity matrix are employed to calculate the polynomial coefficients to attain the accuracy requirement of the gear surfaces. The tooth surface topologies with normal deviations are presented to verify the practicability of the proposed method.

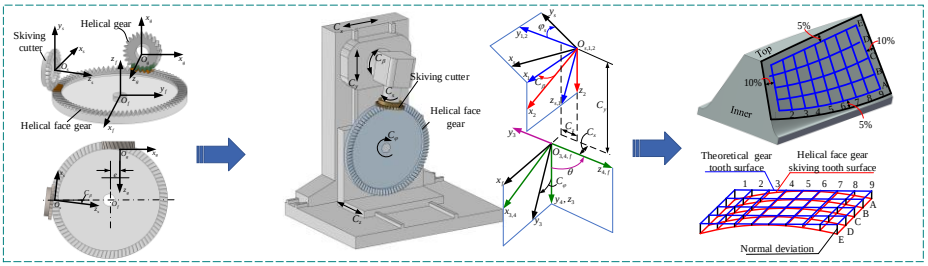

Fig. 1. Helical face-gear skiving process with considering the modified cutter profile and the additional machining-axis motion.

3 Numerical examples and discussions

Designed parameters of the helical face gear, pinion and power skiving cutter.

Parameters	Helical face gear	Pinion	Skiving cutter
Number of teeth (N)	86	23	27
Helix angle (β)	10.0°RH	20.0°LH	5.0°RH
Normal module (m)	4.0 mm	4.0 mm	4.0 mm
Normal pressure angle (α_n)	26°	26.0°	26°
Face width (w)	25.0 mm	25.0 mm	15 mm

(a)

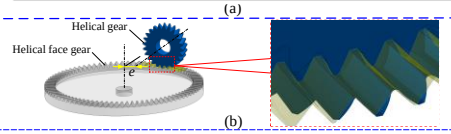

(b)

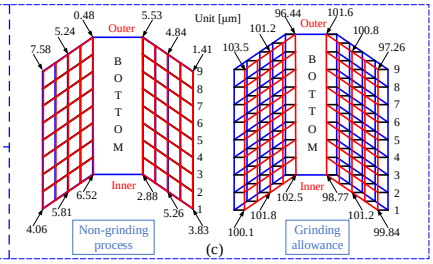

(c)

Fig. 2. (a) design parameters; (b) skived helical face-gear assembled with its mating helical gear; (c) results of normal deviation with and without considering grinding allowance.

An example is presented to show the skiving simulation results of helical face gears for two desired cases: the accuracy grade B5 (ANSI/AGMA 2009-B01 standards) with a maximum deviation on the skived tooth flanks smaller than 7.5 μm (case 1) and the even grinding stock of 100 μm on the skived tooth flanks (case 2). The results indicate that the skived face gear flanks satisfy the desired designs. It is validated the practicability of the proposed model.

References

1. T.-T. Luu and Y.-R. Wu, "A novel correction method to attain even grinding allowance in CNC gear skiving process," Mech. Mach. Theory, vol. 171, p. 104771, (2022).
2. H. Guo, T. Ma, S. Zhang, N. Zhao, and A. Fuentes-Aznar, "Computerized generation and surface deviation correction of face gear drives generated by skiving," Mech. Mach. Theory, vol. 173, p. 104839, (2022).
3. Z. Han, C. Jiang, and X. Deng, "Machining and meshing analysis of face gears by power skiving," J. Adv. Mech. Des. Syst. Manuf., vol. 16, no. 1, pp. JAMDSM0002–JAMDSM0002, (2022).
4. S. Mo, S. Wang, B. Luo, H. Bao, G. Cen, and Y. Huang, "Research on the skiving technology of face gear," Int. J. Adv. Manuf. Technol., vol. 121, no. 7–8, pp. 5181–5196, (2022).

Designing a Spur Shaper Cutter for a Non-Involute Circular Spline

Yun-Hao Cheng[1] and Yi-Cheng Chen[1][0000-0001-7886-3680]

[1] National Central University, Taoyuan 320, TAIWAN
ethan@ncu.edu.tw

1 Spur Shaper Cutter Design

1.1 Introduction

Circular spline (CS), along with flex spline and wave generator, is one of the major components of harmonic drives. This article presents a designing process for a spur shaper cutter to produce a non-involute CS, Firstly, a given profile of a non-involute CS was expressed by a B-spline curve via curve fitting. Then the shaper cutter was derived based on the shaping mechanism [1], the provided CS [2] as well as the theory of gearing [3].

1.2 Shaping Mechanism for CS

A spur shaper cutter resembles a pinion with tapered teeth along the axial direction, and thus is commonly called a pinion cutter. Besides, rake angle, tip relief angle and side relief angle are usually necessary on the shaper cutter for the chip removal purpose and cutting force consideration. Fig. 1 illustrates the kinematic relationship between a spur shaper cutter and a CS which exhibits internal teeth. The pinion cutter and the CS respectively possess external and internal spur teeth.

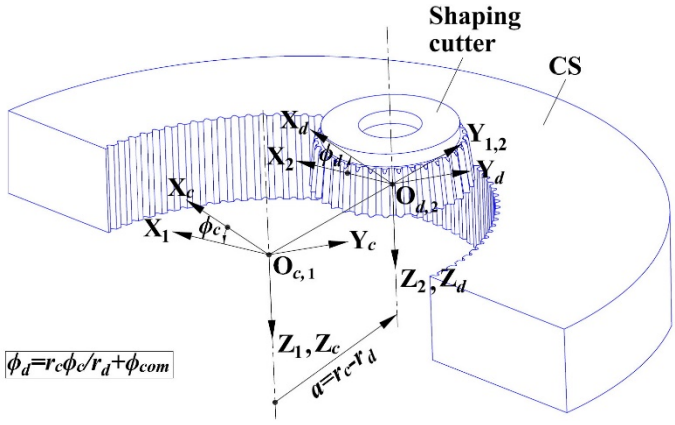

Fig. 1. The shaping process by using a spur shaper cutter to produce a CS.

1.3 Numerical Example

Fig. 2 depicts the designed and generated tooth profiles of the CS. As revealed by Fig.2, the designed CS and the generated CS profile have negligible deviations. More specifically, the maximum deviation between the generated profile and the designed one is less than 1 μm, as shown in Fig. 2, which validates the correctness of the derived shaper cutter corresponding to the proper CS production.

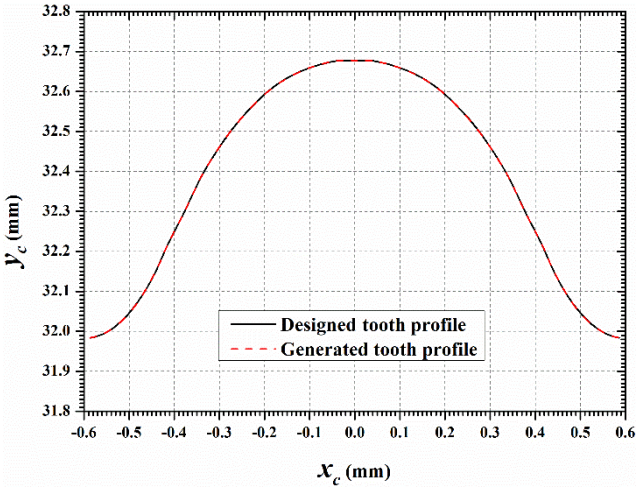

Fig. 2. Designed CS profile and the CS profile generated by the shaper cutter.

Acknowledgement

The authors would like to thank the National Science and Technology Council of Taiwan for finally supporting this research under grant NSTC 111-2221-E-008-073-MY2.

References

1. Tsay, C.B., Liu, W.Y., Chen, Y.C.: Spur gear generation by shaper cutters, J. of Mat. Proc. Tech. 104(3), 271-279 (2000)
2. Cheng, Y.H., Chen, Y.C.: Design, analysis, and optimization of a strain wave gear with a novel tooth profile, Mech. Mach. Theory 175, 104953 (2022).
3. Litvin, F.L., Fuentes, A.: Gear geometry and applied theory, Cambridge University Press, New York (2004).

Ferdinand Freudenstein's Spatial Kinematics

Pierre Larochelle

South Dakota School of Mines & Technology, Rapid City SD 57701, USA,
Pierre.Larochelle@sdsmt.edu,

Prof. Ferdinand Freudenstein is widely recognized as the Father of Modern Kinematics [3, 4]. He made innumerable contributions to the field, one of which is the training of future researchers. By the end of 1965, Dr. Freudenstein had graduated his first cadre of doctoral students from Columbia University that would go on to become world-class researchers and leaders in kinematics. These doctoral graduates included George Sandor (1959)[1], Bernard Roth (1962), Ronald Phillip (1964), A.T. Yang (1964), and Armand Dilpare (1965). In 1966, and soon thereafter, a second cadre was studying with Prof. Freudenstein: Frank Buchsbaum (1967), Leo Dobrjansky (1967), Don Wallace (1968), Ralph Dratch (1970), Steve Dubowsky (1971), and Mark Yuan (1972).

In this paper we examine in detail an advanced graduate-level course taught by Prof. Freudenstein that bridged these first two cadres of doctoral students. In the autumn term of 1965, Prof. Freudenstein taught ME E8405 Spatial Kinematics at Columbia University. In Figure 1 the detailed description of this course from the Columbia University Bulletin is shown [2]. This would be Dr. Armand Dilpare's last term at Columbia University. Dr. Dilpare was a non-traditional student, having worked in industry for several years before beginning his doctoral studies. In his practice of engineering, Dr. Dilpare developed an appreciation for detail and advanced abilities in engineering graphics. He employed these skills when taking detailed and meticulous notes in his courses at Columbia University. Upon his retirement from the Florida Institute of Technology in 1994, Dr. Dilpare donated his course notes to the author. An example of his course notes, on the Euler-Savary Equation on a Sphere, is shown in Figure 2. In this paper we examine the contents of Dr. Freudenstein's advanced graduate course in spatial kinematics through the lens of Dr. Dilpare's detailed course notes.

M.E. E8405y. Spatial kinematics

Professor Freudenstein. (3) Hours to be arranged.

Prerequisite: a graduate course in kinematics or design.
Freedom, classification, and type synthesis of spatial mechanisms; motion on a sphere and general spatial motion; infinitesimal and finite displacement theory, including velocities, accelerations, curvature, and higher invariants; screw calculus; matrix transformations and Cayley-Klein parameters; quaternion algebra and dual number techniques; application to kinematic analysis and synthesis of basic spatial mechanisms, including determination of static forces and torques, transmission characteristics, and passive constraint criteria; survey of spatial mechanisms and discussion of applications.

Fig. 1. ME E8405 Course Description [2]

[1] The year the doctoral degree was awarded is listed in parenthases.

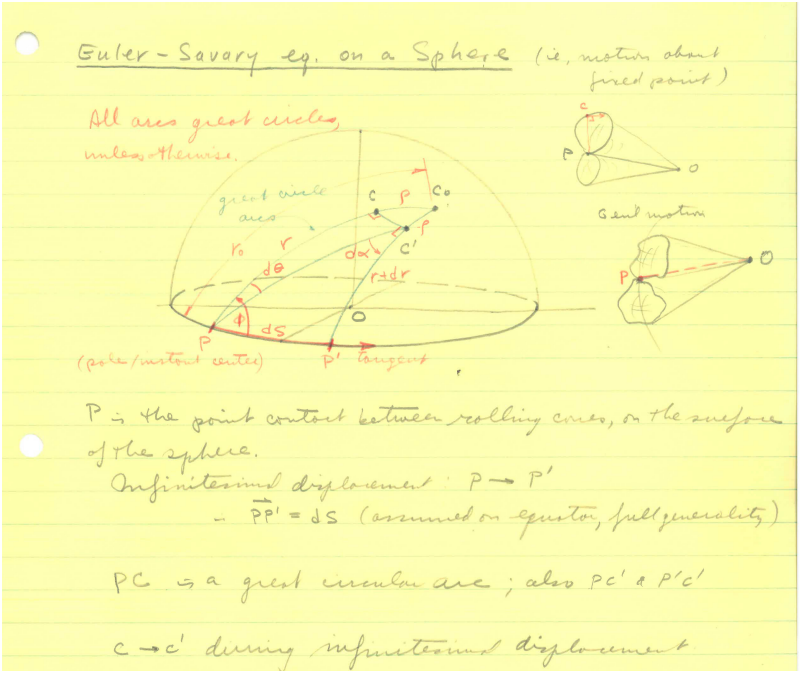

Fig. 2. Example from ME E8405 Course Notes [1]

Acknowledgments The late Dr. Armand Leon Dilpare is gratefully acknowledged for giving his detailed and illustrated ME E805 Spatial Kinematics fall 1965 course notes to the author. Dr. Ferdinand Freudenstein is whole-heatedly acknowledged for his founding of modern kinematics and for inspiring generations of kinematicians around the globe.

References

1. Dilpare, A.: Course Notes ME E8405 Columbia University Fall 1965.
2. Columbia University: School of Engineering and Applied Sciences Bulletin 1965-1966, Columbia University. New York, NY. Series 65, Number 5, May 28, 1965. https://findingaids.library.columbia.edu/ead/nnc-ua/ldpd_14621921/dsc
3. Erdman, A.G.: Modern Kinematics: Developments in the Last Forty Years. John Wiley & Sons, 1993. ISBN 9780471554592.
4. Roth, B., In Memory of Professor Ferdinand Freudenstein, 1926–2006, *ASME Journal of Mechanical Design*, Volume 129, Number 3, Pages 241–242, March, 2007.

A New Design Method for Thick-panel Origami

Rui Peng[1] and Gregory Scott Chirikjian[1]

[1] National University of Singapore, Singapore 119077, Singapore
mpegre@nus.edu.sg

1 Introduction

Origami has great potential for applications in multiple fields [1]. However, it is complex and challenging to apply origami in some application circumstances, especially those with strong requirements of using thick materials to keep motion accuracy and structure robust.

Modifying the origami pattern first and then using the altered origami pattern to build a thick origami structure is a unique method to accommodate the thickness. Based on this concept, Ku and Demaine split every crease in a pattern into two creases [2], but the smooth surface of the origami pattern is broken with additional holes and more difficult to fold. These problems can only be avoided for specific symmetric origami patterns using Hull and Tachi's approach [3] or just splitting parts of creases [4,5]. Those approaches have strict geometrical requirements for the target origami patterns. They can only be applied to symmetric origami patterns, but there is no such limitation in this presentation. Thus, references [2-4] cannot achieve any physical thick panel models built in this presentation. Moreover, by using this presentation's approach, any origami patterns containing one or more of the three basic patterns proposed in this presentation can be used to build thick panel structures.

In this presentation, we propose a novel thickness-accommodation approach. The thick-panel origami structure built by our methods is one-degree-of-freedom with a large fold-deploy ratio and has no holes. Besides symmetric patterns, the approach is also suitable for more general origami patterns, such as the double-corrugated pattern, square-twist pattern, and general Miura-ori pattern. Besides flat patterns, this method can also be used for origami tubes.

2 Main concept

The inherent problem of thickness accommodation is to avoid the collision between adjacent facets induced by no allowance along the creases, which is more challenging for flat-foldable patterns. However, folding from a flat state to another flat state makes the pattern very advantageous with a large fold-deploy ratio. The basic concept of this presentation is to modify the flat-foldable vertex to a non-flat-foldable vertex but keep the original vertices' motion features. The basic concept of this presentation is to convert a flat-foldable pattern into a quasi-flat-foldable pattern and use the quasi-flat-foldable pattern to build thick origami structures [6].

Fig. 1(a) is the square-twist pattern. According to the rules in this presentation, transfer it to the quasi-flat-foldable pattern in Fig. 1(b). Then a thick panel structure in Fig. 1(c) is built based on Fig. 1(b). Compared with photos of the original pattern, its corresponding quasi-flat-foldable patterns, and thick-panel structure, it is seen that their folding motions are the same.

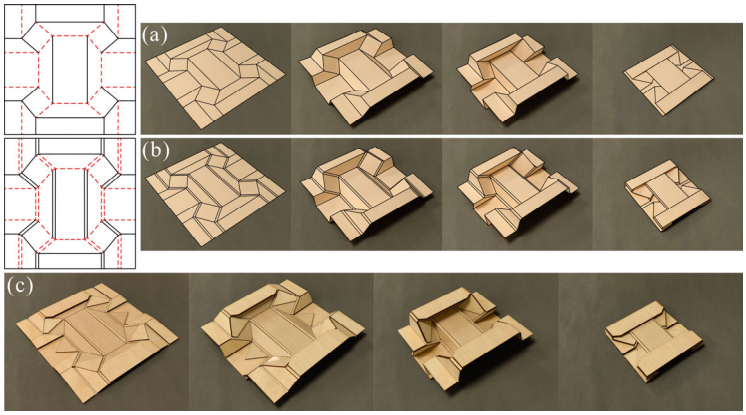

Fig. 1. (a) The original square-twist pattern. (b) The corresponding quasi-flat-foldable pattern. (c) The corresponding thick-panel structure.

3 Conclusion

This presentation has proposed a technique for building thick-panel structures from flat-foldable origami patterns. These structures maintain the folding motion of the original origami patterns. They also have large fold-deploy ratios and very compact folded states. This technique is applicable to any patterns constituted by the three basic two-vertex patterns proposed in this presentation.

References

1. J.S. Dai, J. Rees Jones, Mobility in metamorphic mechanisms of foldable/erectable kinds, Journal of Mechanical Design, 121 (1999) 375-382.
2. J.S. Ku, E.D. Demaine, Folding flat crease patterns with thick materials, Journal of Mechanisms and Robotics, 8 (2016) 031003.
3. T.C. Hull, T. Tachi, Double-line rigid origami, arXiv preprint arXiv:1709.03210, (2017).
4. K.A. Tolman, R.J. Lang, S.P. Magleby, L.L. Howell, Split-vertex technique for thickness-accommodation in origami-based mechanisms, International Design Engineering Technical Conferences and Computers and Information in Engineering Conference, American Society of Mechanical Engineers, 2017, pp. V05BT08A054.
5. K.A. Tolman, Developing hybrid thickness-accommodation techniques for new origami-inspired engineered systems, Brigham Young University, 2017.
6. R. Peng, G.S. Chirikjian, A methodology for thick-panel origami pattern design, 2023. (Under review)

A tensegrity-based elastic joint element

Lukas Merker*, Valter Böhm, and Lena Zentner

*Technische Universität Ilmenau, Germany,
lukas.merker@tu-ilmenau.de,
WWW home page: https://www.tu-ilmenau.de/

1 Introduction

In design engineering, it is frequently beneficial to couple components elastically, e.g., compensating for geometrical misalignment [1] or providing passive vibration control [2]. Within this paper, we present an elastic *tensegrity*-based joint element (TJE) according to Fig. 1(a). Even though similar structures are already commercially available as toys, art sculptures, or pieces of furniture, they are rarely realized as compliant structures and, if so, the ability of the system to undergo significant deformations often remains unconsidered. In contrast, we suggest exploiting pre-stressed highly elastic tension members to realize a compliant structure and analyze its deformations under different load cases [3]. Our investigation includes the analysis and modeling procedure of the TJE, the identification of important system parameters as well as numerical simulations to clarify the stiffness behavior of the TJE.

2 Modeling

The 3D structure in Fig. 1(b) consists of two rigid compression members (CMs), each of which includes four nodes. The nodes are pairwise connected by four cylindrical linear elastic tension members (TMs) with cross-sections A_i, Young's moduli E and original lengths l_{0_i}. We consider one CM as fixed in a *global frame* $(0, x_0, y_0, z_0)$, and the other one as displaced along with a *local frame* (Ω, x, y, z) under the inference of an external load. The final position of the displaced CM is described using the vector $\vec{r}_0 = \overrightarrow{0\Omega}$ and the classic Euler angles α, β and γ:

$$\vec{r}_0 = (r_x, r_y, r_z)^T, \quad (\vec{e}_{x_0}, \vec{e}_{y_0}, \vec{e}_{z_0})^T = \mathbf{T}(\alpha, \beta, \gamma)(\vec{e}_x, \vec{e}_y, \vec{e}_z)^T \tag{1}$$

According to (1), six unknown parameters define the overall shape of the structure, including the lengths and orientations of all TMs, see Fig. 1(b):

$$\vec{l}_i = \vec{r}_0 + \mathbf{T}(\alpha, \beta, \gamma)\vec{b}_i - \vec{a}_i, \quad l_i = |\vec{l}_i|, \quad \vec{e}_i = \vec{l}_i / l_i \tag{2}$$

In (2), $\vec{a}_i$ and $\vec{b}_i$ are the position vectors of the nodes $i = 1, ..., 4$ defined w.r.t. the global and local frame, respectively. For any external force $\vec{f}$ and/or external moment $\vec{m}$ acting at Ω, the arising tensile forces $\vec{f}_i = \frac{EA_i}{l_{0_i}}(l_{0_i} - l_i)\vec{e}_i$ of the TMs are used to express the equilibrium conditions in the deformed state:

$$\vec{0} = \vec{f} + \sum_{i=1}^{4} \vec{f}_i, \quad \vec{0} = \vec{m} + \sum_{i=1}^{4} \mathbf{T}\vec{b}_i \times \vec{f}_i \tag{3}$$

As (3) includes six scalar (nonlinear) equations and six unknown parameters, see (1), it is well defined and can be solved numerically to find the deformed shape of the structure for any given load state, e.g., see Fig. 1(c).

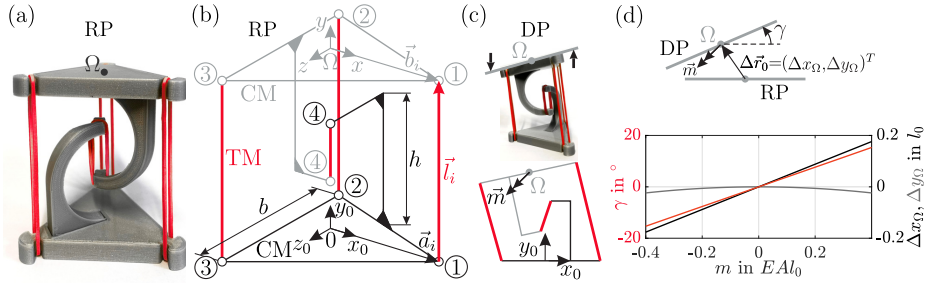

Fig. 1: (a) TJE in a reference configuration (RC); (b) mechanical model in RC; (c) deformed configuration (DC); (d) displacement $\Delta\vec{r}_0$, γ caused by $\vec{m}$.

3 Results and Discussion

Inspired by the physical model in Fig. 1(a), we choose an exemplary structure with $b{=}h{=}l_{0_i}|_{i=1,\dots,3}{=:}l_0$, $l_{0_4}{=}\frac{l_0}{2}$ and $E{\cdot}A_i|_{i=1,\dots,3}{=:}E{\cdot}A{=}\frac{1}{3}{\cdot}E{\cdot}A_4$, see Fig. 1(b). For sake of conciseness, we limit the consideration to the x_0-y_0-symmetry plane here. Figure 1(c) qualitatively shows the deformed configuration of the structure for the example of an external moment $\vec{m} = m\,\vec{e}_{z_0}$ acting at Ω. Figure 1(d) shows the displacement vector $\Delta\vec{r}_0 = (\Delta x_\Omega, \Delta y_\Omega)^T$ and angle γ plotted against $m \in [-0.4, 0.4]{\cdot}E{\cdot}A{\cdot}l_0$. It becomes clear that the deformation of the structure is approximately symmetrical for positive and negative moments with Δx and γ changing approximately linear with the external moment. In this way, we investigate the deformation of the TJE in further non-symmetry planes in the context of different load cases, including both external forces and moments. The presented model serves as a basis for parameter studies to show that the stiffness behavior of the structure is significantly affected by the parameters b and h, see Fig. 1(b) as well as by the lengths l_{0_i}. In this way, we demonstrate that the presented TJE offers tunable mechanical properties. Moreover, we highlight the advantages that the TJE is scalable, easy to manufacture and to duplicate and, thus, cascadable both in serial or parallel arrangement.

References

1. Smith, S. T.: Flexures: elements of elastic mechanisms. Crc Press (2000)
2. Bian, J., Jing, X.: Analysis and design of a novel and compact X-structured vibration isolation mount (X-Mount) with wider quasi-zero-stiffness range. Nonlinear Dyn., **101**(4), pp. 2195-2222 (2020)
3. Vega, J. C., Schorr, P., Kaufhold, T., Zentner, L., Zimmermann, K., Böhm, V.: Influence of elastomeric tensioned members on the characteristics of compliant tensegrity structures in soft robotic applications. Procedia Manuf., **52**, pp. 289-294 (2020)

We acknowledge the support by the DFG within the SPP 2100 projects ZE714/14-1, BO4114/3-1.

Coupler curves of a tendon driven hybrid rigid-flexible four-bar. Applications to optimal path design

Alfonso Hernández[1], Aitor Muñoyerro[2], Mónica Urizar[1], Oscar Altuzarra[1]

[1] Faculty of Engineering of Bilbao, University of the Basque Country UPV/EHU. Plaza Torres Quevedo 1, Bilbao 48013, Spain
[2]ITP Aero – Zamudio, Parque Tecnológico nº300, 48170 Vizcaya, Spain
Contact author: monica.urizar@ehu.eus

Unlike rigid link mechanisms, where positions can be determined by taking into account the geometry and configuration of the joints through a purely kinematic analysis, compliant mechanisms require the consideration of elasticity to define their configuration [1]. Therefore, a deformation model of the mechanism's parts must be considered together with the forces and moments applied to it by its own actuators and the external environment. This makes obtaining closed-form solutions of classical kinematic problems a difficult task. In [2], the authors develop an approach consisting of using tendon actuated bars to drive parallel kinematic mechanisms. In this case, the kinematic analysis problem of the parallel robot 3-RF[b]R has been tackled by taking advantage of the simplifications introduced by working with deformable bars of constant curvature. A flexible actuated bar of this type will replace the crank input of a four-bar hinged linkage of rigid elements. The resulting mechanism will be used to study the geometry of the curves generated by a coupler point. Now the input is the tendon's curvature, κ, instead of the angular orientation of the crank. Figure 1 shows the parameters and variables representing the kinematics of such a hybrid mechanism.

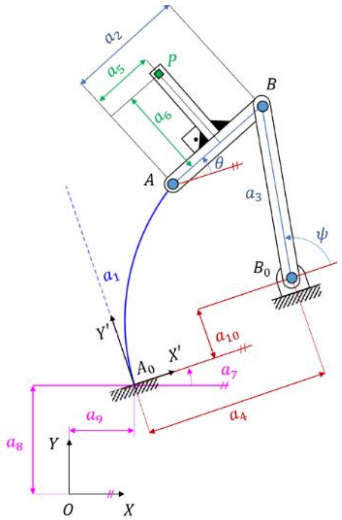

Fig. 1. Kinematics parameters of the Tendon Driven Hybrid Rigid-Flexible Four-Bar

The first part of this work consists of characterizing the coupler curves of this mechanism. We have studied the composition of the coupler curves in circuits, and within circuits the existence of one or more branches, following a pattern similar to [3]. Depending on the existence and location of the blocking positions, three different cases can occur. These is described and analyzed in detail, highlighting fundamental differences in comparison to the rigid four-bar. In fact, the paths of these hybrid frigid-flexible mechanisms can include "open" circuits, more than two circuits and there are no (closed) circuits with only one branch.

In the second part, the knowledge related to these paths is implemented in an optimization algorithm, based on the gradient of the error function. Two objectives are pursued. The first one is to avoid circuit and branch errors. To do this, the optimization algorithm must know, at each iteration, in which circuit and in which branch the coupler-point is located. The second target is to integrate the characterization about the number and type of circuits that make up the path into the optimization algorithm. The idea is that optimization process ceases to be a “closed box”, being able to use this knowledge in an intelligent way to get the best solution. The examples carried out on dimensional synthesis of path generation show the effectiveness of this new optimization algorithm. A very good quality of solutions is obtained, considering the possibilities offered by this simple mechanism. In addition, the algorithm guarantees mechanisms free of circuit and branch errors, typical of this type of synthesis.

Acknowledgments

The authors wish to acknowledge the financial support received from the Spanish Government through the Ministerio de Ciencia e Innovación (Project PID2020-116176GB-I00) financed by MCIN/AEI/10.13039/501100011033 and the support for the research group through Project IT1480-22 provided by the Departamento de Educación from the Regional Basque Government.

References

1. L.L. Howell, S. P. Magleby, B. M. Olsen (Eds.). Handbook of Compliant Mechanisms. Wiley (2013).
2. S. Lilge, K. Nuelle, G. Boettcher, S. Spindeldreier, J. Burgner-Kahrs. Tendon Actuated Continuous Structures in Planar Parallel Robots: A Kinematic Analysis. *Journal of Mechanisms and Robotics* 13 (2021) 011025.
3. A. Hernández, A. Muñoyerro, M. Urízar, E. Amezua. Comprehensive approach for the dimensional synthesis of a four-bar linkage based on path assessment and reformulating the error function. *Mechanism and Machine Theory* 156 (2021) 104126.

Genetic Algorithm Application in Walking Mechanism Designed with Planar Link Mechanism

Yoshihiko Matsumoto and Yasuhiro Inoue[0000-0002-1968-8883]

Kyoto University, Kyoto 615-8540, Japan
matsumoto.yoshihiko.t65@kyoto-u.jp

1 Introduction

Link mechanisms are essential in industries for enabling complex motions with simple structures and providing accurate performance under high-speed conditions. Traditional design methods of link mechanisms involve discretizing the desired trajectory and solving closed-loop equations at each point [1]. This study presents a new design method using a genetic algorithm specifying the desired task as an input. Our proposed method is applied to design a walking mechanism, and we present actual design result.

2 Method

In this study, we determine how to assemble the link mechanism and extract the parameters necessary for assembly, and define a relationship between the parameters and genotypes. The genetic algorithm incorporates the minimal generation gap [2] and island models to improve the preservation of genetic diversity. Physical simulations are conduced to evaluate the fitness.

3 Results

A physical simulation environment was created to test link mechanisms, considering the possibility of collisions between links and pins. The fitness of a link mechanism was defined as the distance the mechanism could move a slider when the driving link was rotated at a constant speed and torque for a duration of 60 seconds in the simulation environment. The termination criteria were set at 100,000 generations.

The walking mechanism was designed 100 times, and the results were classified into two clusters using the expectation-maximization algorithm [3] (Fig.1 a). The mechanisms that belong to high-fitness cluster categorized based on their structure pattern and Fig.1 (b) shows the best-fitted design for each pattern. Fig. 1 (c) depict the movements of the upper-right pattern mechanism shown in Fig. 1 (b). Fig. 1 (d) shows the trajectories of the ground points of mechanisms shown in Fig. 1 (b). Despite structural differences, mechanisms with links connected to the same side of the main body exhibited similar movements.

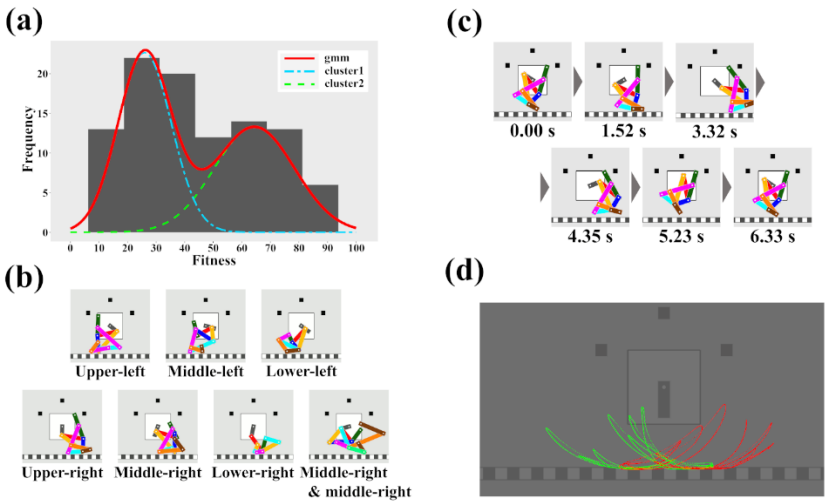

Fig. 1. (a) Histogram of the best fitness in each of the 100 design runs. (b) Best individuals per each structure pattern of high-fitness cluster. (c) Movement of the mechanism upper-right pattern in (b). (d) Superimposed trajectories of the seven mechanisms shown in (b). The red and green lines are the trajectories of the first and last points to be grounded, respectively.

4 Discussion

In this study, we successfully generated a walking mechanism using a genetic algorithm. The generated mechanisms consist of a mixed population with both low and high fitness. Notably, we observed a variety of structures within the high-fitness group, despite the single-objective optimization. This observation led us to recognize the potential for proposing a new strategy for multi-objective optimization. Our approach focuses on obtaining diverse solutions through multiple calculations instead of a single computation. The underlying idea is that, by generating numerous solutions without imposing restrictions on secondary objectives and evaluating fitness solely based on the primary objective, we can extract a solution from the diverse population that satisfies multiple objectives. We believe that this approach is now feasible due to the significant advancements in computing power.

References

1. Freudenstein, F.: Approximate Synthesis of Four-Bar Linkages. Trans. ASME 77, 853–861 (1955).
2. Satoh, H., Yamamura, M., Kobayashi, S.: Minimal Generation Gap Model for GAs Considering Both Exploration and Exploitation. Proceedings of 4th International Conference on Soft Computing, 494-497 (1996).
3. Dempster, A. P., Laird N. M., Rubin, D. B.: Maximum Likelihood from Incomplete Data via the EM Algorithm. J. Royal Stat. Society. Series B (Methodological) 39(1), 1-38 (1977).

Friction-induced redundancy of constraints and its consequences

Marek Wojtyra[1][0000-0001-7225-7647] and Janusz Frączek[1][0000-0001-8232-5439]

[1] Warsaw University of Technology, IAAM, Nowowiejska Str. 24, 00-665 Warsaw, Poland
Marek.Wojtyra@pw.edu.pl

1 Introduction

In many multibody modeling cases, the rigid body assumption is often adopted because it has many advantages, mainly in terms of model complexity and computational efficiency. However, there are limitations of this approach—associated with redundant constraints presence—which become particularly important when modeling friction effects. When friction that depends on normal reactions in joints is present in an overconstrained multibody system, the simulated motion of the system may be non-unique.

The present study shows that redundant constraints—with all their unavoidable consequences—may be introduced to the model by the frictional locking of the joints. Two distinct approaches to static friction modeling are examined: (1) constraints addition and deletion [1] and (2) adding static friction as an active force governed by the adopted friction model (e.g., the smooth Coulomb or LuGre [2]). It is indicated that in the latter case, uniqueness problems evolve into parametric sensitivity problems.

2 Research and results

A mechanism described by n coordinates forming vector $\mathbf{q}$, subjected to m non-redundant constraints $\mathbf{\Phi}(\mathbf{q}) = \mathbf{0}_{m\times 1}$, is analyzed. It has one or more kinematic loops and more than one DoF ($d = n–m > 1$). The generalized forces of sliding friction are introduced as external loads relying on normal joint reactions [1], [3].

In the constraint addition-deletion method [1], static friction in the appropriate joints is represented by additional driving constraints $\mathbf{\Psi}(\mathbf{q}) = \mathbf{0}$, imposed when the relative velocity reaches zero. In the 1-DoF case, relative motion in all joints stops simultaneously, and constraints $\mathbf{\Psi}$ are added to all joints with friction. If the number of constraints $\mathbf{\Psi}$ exceeds the number of DoFs, the mechanism becomes redundantly constrained [3]. Mind that the non-uniqueness of calculated joint reactions—and hence of friction forces—is a direct consequence of the constraints' redundancy. Further, detection of stiction to sliding transition becomes impossible.

The situation is more intricate for mechanisms with many DoFs, and several distinct cases must be analyzed. A particular case occurs when relative velocities vanish in several kinematic pairs simultaneously, and k scalar constraint equations are added, whereas the number of the system's DoFs decreases by less than k, and the mechanism becomes overconstrained (with all unwelcome consequences).

The constraint addition-deletion method is rarely used. Stiction is more often introduced in terms of active forces rather than constraints. Usually, stiction and sliding modes are modeled uniformly—the same equations (highly nonlinear at close to zero relative velocities) are used for both friction modes. In article [3] (limited to closed-loop chains with exactly one DoF), it was shown that—at the vicinity of the stiction regime—solution non-uniqueness and high parametric sensitivity occurs when mechanisms with joint friction but without redundant constraints are modeled. In the present study, we show that the earlier results regarding the outcomes of frictional locking may be generalized to the case of closed-loop systems with many DoFs, under the condition that particular relations within the kinematic structure exist. Examination of the kinematic properties of the mechanism alongside the equations depicting the friction model reveals the reasons for the high parametric sensitivity and, therefore, the low credibility of the simulation results. For the smooth Coulomb and the LuGre model, we show that—in the stiction regime and its vicinity—the obtained results hinge on some secondary parameters, usually arbitrarily set to satisfy certain numerical needs.

For some mechanisms, the simultaneity of frictional locking of several joints (leading to sensitivity or uniqueness problems) is unavoidable since this property is embedded in their kinematic structure and dimensions. Hence an apt method for the mechanism's structure investigation was devised. In brief, the fact that allowable generalized velocities of a mechanism belong to the nullspace of the constraint Jacobian matrix is utilized. The dependencies between relative velocities in joints are investigated by adding suitably selected driving constraints $\boldsymbol{\Psi}$ to geometric constraints $\boldsymbol{\Phi}$, determining the nullspace of $[\boldsymbol{\Phi}_{\mathbf{q}}^{T}(\mathbf{q}) \quad \boldsymbol{\Psi}_{\mathbf{q}}^{T}(\mathbf{q})]^{T}$, and performing specific geometrical calculations.

3 Conclusions

The uniqueness problems—encountered in certain classes of mechanisms when static friction is represented by additional driving constraints—evolve into difficulties with high parametric sensitivity when the stiction regime is modeled by active forces rather than constraints. This contribution analyzes the foundations of these problems, and a method for investigating the kinematic structure—to check if the problematic issues may arise—is devised.

Acknowledgments. This research was supported by the National Science Centre, Poland grant no. 2022/45/B/ST8/00661.

References

1. Haug E. J., Wu S. C., Yang S. M.: Dynamics of mechanical systems with Coulomb friction, stiction, impact, and constraints addition-deletion. Mechanism and Machine Theory, 21(5), 401–425 (1986).
2. Marques F., et al.: A survey and comparison of several friction force models for dynamic analysis of multibody mechanical systems, Nonlinear Dynamics, 86(3), 1407–1443 (2016).
3. Wojtyra M.: Modeling of static friction in closed-loop kinematic chains—Uniqueness and parametric sensitivity problems. Multibody System Dynamics, 39(4), 337–361 (2017).

A Study on a Method for Maintaining Contact During Capture of Space Debris with an Magneto-Rheological Damper

Ryogo Mizuno[1], Satoko Abiko[2], and Teppei Tsujita[3]

[1] Graduate School of Engineering and Science, Shibaura Institute of Technology,
3-7-5 Toyosu, Koto-ku, Tokyo 135-8545, Japan
ma22137@shibaura-it.ac.jp
[2] Department of Electrical Engineering, Shibaura Institute of Technology,
3-7-5 Toyosu, Koto-ku, Tokyo 135-8545, Japan
abiko@shibaura-it.ac.jp
[3] Department of Mechanical Engineering, National Defense Academy of Japan,
1-10-20 Hashirimizu, Yokosuka, Kanagawa 239-8686, Japan
t.tsujita@ieee.org

1 Introduction

According to [1], five debris removals per year are required for sustainable space utilization. Capturing large debris with a robot arm is considered one of the removal methods [2]. In this method, contact force must be reduced during capture so as not to push the target away. However, the momentum of the target depends on its size and state. Therefore, it is required to deal with them in the capture operation. This paper proposes debris capture with a double-rod Magneto-Rheological (MR) damper that generates a variable damping force as shown in Fig.1.

2 Modeling of a Double-rod MR damper

The MR damper is a device whose damping force is varied by changing the flow resistance of the MR fluid filled in the damper. This rheological property can be controlled by changing the magnetic field applied to the MR fluid. The principle of operation of the double-rod MR damper is modeled based on [3].

3 Dynamics Simulation for Debris Capture

The equations of motion for the chaser, MR damper and target are formulated and dynamics simulations are performed as shown in Fig.1. The simulations are performed using the numerical software MATLAB/Simulink from The MathWorks, Inc. In the simulation, the debris approaches the chaser satellite and impacts the end-effector connected to the MR damper. In the simulation, the satellite and the end-effector weigh 100 kg and 10 kg, respectively. The debris

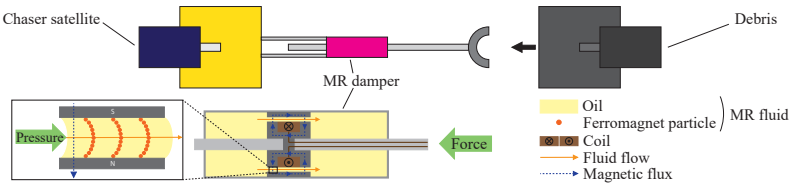

Fig. 1. Assumption of debris capture and MR damper mechanism

approaches the satellite with a relative velocity of 1 m/s. The debris weights are 10, 50, 100, 500, and 1000 kg. The four types of dampers are simulated. The first is an MR damper with no magnetic field applied, and its damping coefficient is approximately 150.8 Ns/m (Type 1). The second is an MR damper that controls the applied magnetic field by current during the collision. The reference impulse is the momentum the MR damper should accumulate so that the relative velocity between the chaser and target becomes zero. When the ratio of the impulse at time t to the reference impulse is 0 or 1, the current is set to 0 A. When the ratio is 0.95, the current is set to the maximum value. The current is changed along a 5th-order spline curve that satisfies these conditions (Type 2). The third and fourth are linear dampers, with damping factors of 150.8 Ns/m (Type 3) and 600.0 Ns/m (Type 4).

In the simulation, the smaller the damping coefficient, the smaller the maximum damping force during contact, but the longer the stroke length. In this simulation, the stroke length limit of the dampers is set to 0.20 m. In the type 1 and type 3 simulations, the damper reached its stroke limit when the target weighs 50 kg or more. In the simulation, the larger the damping coefficient, the shorter the stroke length, but the larger the maximum damping force. In the type 4 simulation, the maximum damping force is greater than that of type 1 and type 3. When the target weighs 1000 kg, the difference is about 650 N. Damping force has a negative influence on the base of a satellite. Therefore, dampers are required to reduce the maximum damping force within the possible stroke range. In the type 2 simulation, the stroke length is within 0.20 m and the maximum damping force is smaller than type 4, by changing the damping characteristics of the MR damper. For instance, when the target weighs 500 kg, the difference is approximately 350 N.

In the design of the MR damper for debris capture, it is required to have the performance for capturing a wide range of target properties. The simulation result shows the MR damper is promising to satisfy the requirement.

References

1. Liou, J.C.: An active debris removal parametric study for LEO environment remediation. Advances in Space Research, vol. 47, issue 11, pp. 1865-1876 (2011)
2. Papadopoulos, E., Aghili, F., Ma, O., Lampariello, R.: Robotic Manipulation and Capture in Space: A Survey. Frontiers in Robotics and AI, 8:686723 (2021)
3. Goldasz, J., Sapinski, B.: Insight into Magnetorheological Shock Absorbers. Springer (2015)

Experimental Determination of Calibrated Accuracy for Six-axis Force and Torque Sensors Using Compliant Mechanisms

Yu-Jen Wang[1] and Shin-Yi Huang[1]

[1] National Sun Yat-sen University, Kaohsiung 80424, Taiwan
yjwang@mail.nsysu.edu.tw

1 Introduction

With the popularity of robot arm applied in fabrication process and multi-axis loads monitoring in machining, multi-axis force and torque (F/T) sensors have become key components in the automated factory [1]. Accuracy and sensitivity of six-axis F/T sensor are crucial. Strain-gauge-based F/T sensors have high measurement accuracy, and is mainly suitable for static or quasi-static measurement. The design of the compliant structure considers coupling effects, sensitivity and full span of the sensor. A compliant mechanism composed of flexible links achieves force and motion transmission through elastic deformation. The advantages of compliant mechanisms include without mechanical parts assembly, reduced friction and no backlash. A planar-type F/T sensor using compliant mechanisms has strain gauges on the top or bottom surfaces only, without any strain gauges on the side surfaces to reduce the fabrication cost [2]. According to aforementioned information, the axis decoupling structure, e.g. the dual-frame structure [3], has benefits on high decoupling results, but it is difficult to fabricate and attached with strain gauges. On the other hand, the axis coupling structure, e.g. the planar-type F/T sensor, the main advantage is easy to fabricate, but the axis coupling effect is obvious. This paper will discuss the precision of the two F/T sensors using different calibration data sets to find the suitable calibration process for the F/T sensors.

2 Structures of dual-frame F/T and planar-type F/T sensors

The structure of the F/T sensor is axisymmetric and consists of a dual frame with inner and outer elastic parts as shown in [3]. The planar F/T sensor is 120-deg-symmetrical about the geometric center and consists of three limbs, as shown in Fig.1. The six-axis force and torque sensor is based on 3-RRR (rotation) compliant mechanism [2]. Compliant mechanisms are mechanisms using flexible hinges instead of rigid joints. Forces and torques are defined by the coordinate o at the end effector. Strain gauges S_1 to S_6 are used to sense F_x, F_y, and T_z, and are composed as V_1 to V_3. The strain gauges of sensing plates on the top and bottom surfaces are diagonally connected in Wheatston half-bridge circuit. The correspondence between the strain gauge pairs and the measured F/Ts was provided. The sensing plates are closed to pivot joints of each RRR mechanism that enlarges the strains on the sensing plates.

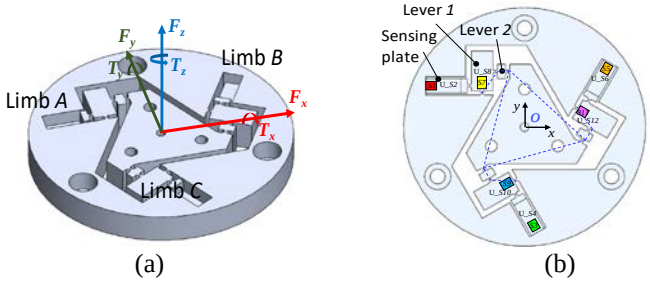

(a) (b)

Fig. 1. Structure of planar six-axis force/torque sensor [2].

3 Calibration process and results

The calibration machine was developed to provide six-axis independent and known forces and torques to calibrate F/T sensors [4]. Calibration is performed for mapping the relationship between the inputs and the outputs of a sensor. A transformation matrix to convert the output signals (voltages) into the subjected F/T components is acquired by using least square method. The calibration results are shown in Figs. 2 (a) and (b). A total of 420 single-axis F/T sets that included a repeated measure for each axis with 10 N and 0.5 N-m intervals were used as training data. The six-axis data was composed by the single-axis data. The full-span loads of the F/T sensors were decided as F_x, F_y, and F_z = ±200 N and T_x, T_y, and T_z = ±10 N-m. The test data sets are six axis data. Once the F/T sensor with excellent super position (linear) behaviors, the calibration errors using single- and six-axis data would be the same. Therefore, the two sensors have some non-superposition behaviors. The mean errors of the dual-frame sensor using single- and six-axis data sets are 1.45% and 1.21% respectively. The mean errors of the planar F/T sensor using the two data sets are 2.76% and 2.34% respectively. That shows the dual-frame F/T sensor with better accuracy than the planar type F/T sensor. To test the accuracy of the calibrated sensors, the testing data in Fig. 2 (c) are random six-axis data sets that didn't used in calculated the transformation matrix. The differences between Figs. 2 are insignificant. That shows the calibration process using six-axis data sets are representative even tested by additional data sets. The accuracy of the dual-frame F/T sensor is higher than that of the planar type F/T sensor. The calibration process in F_x, F_y and T_z should be checked or reworked. The calibration results of the two types of F/T sensors are promising. Therefore, planar F/T sensors have good performance and easy fabrication advantage. The F/T sensor using compliant mechanisms could be applied to the end effector of the robot arm to sense applied loads with high accuracy.

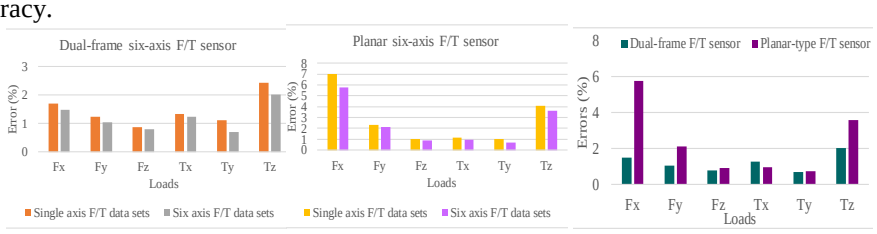

(a) (b) (c)

Fig. 2. Calibration errors using single axis and six axis data sets (a) for dual-frame F/T sensor and (b) for planar six-axis F/T sensor. (c) Calibration errors tested by random six-axis data sets for the two sensors.

References

1. I. Payo, J. M. Adánez, D. R. Rosa, R. Fernández, and A. S. Vázquez, "Six-Axis Column-Type Force and Moment Sensor for Robotic Applications," *IEEE Sensors J.*, 18(17), 6996-7004, (2018).
2. Y. J. Wang, L. C. Wu, J. D. Ke and T. F. Lu, "Planar Six-Axis Force and Torque Sensors," *IEEE Sensors J.*, 21(23), 26631-26641, (2021).
3. Y. J. Wang, C. W. Hsu and C. Y. Sue, "Design and Calibration of a Dual-Frame Force and Torque Sensor," *IEEE Sensors J.*, 20(20), 12134-12145, (2020)
4. Y. J. Wang and C. W. Tung, "A machine for calibrating six-axis force/torque sensors using a torque sensing structure and a stiffness compensation model," *Sensors and Actuators A: Physical*, 334(1), 113323, (2022).

The Effects of Passive Joints on the Stiffness of a Parallel Kinematic Manipulator

Pin-Yi Ho[1], Chia-Hsin Hsieh[1], Wei-Hsuan Lin[1], Chih-Wei Li[1], Cheng-Kuo Sung[1] and Yu-Jen Chiu[2*]

[1] National Tsing Hua University, Hsinchu 300044, Taiwan R.O.C.
[2] Ming Chi University of Technology, New Taipei City 243303, Taiwan R.O.C.
yjchiu@mail.mcut.edu.tw

1 Introduction

Due to the inherent close-looped configurations, parallel kinematic manipulators (PKMs) are anticipated to possess higher stiffness and lower inertia than those with serial-type mechanisms. Nonetheless, one of the important features of a PKM is that a number of passive joints are essentially introduced. A passive joint will lose the ability of resisting the force and moment along the direction of its degrees-of-freedom, thus considerably deteriorating the precision of a PKM when external loads are applied. It has been inferred as one of the causes that leads to geometrical discrepancies of PKMs [1]. The present work is aimed at the quantitative investigation into the passive joints that influence the stiffness of a PKM. Both the analytical approach based on the matrix structural analysis (MSA) [2] and the finite element analysis (FEA) by employing the commercial software are introduced in this study. The proper orientations of the passive joints installed are analyzed and suggested as well.

2 Methods

A translational 3-UPU configured PKM with variable-length links is considered in this work to investigate its elastostatic behavior. In Fig. 1, Each of the three linkage modules of the PKM is dismantled into two universal joints A_i, B_i and one link L_i ($i=1, 2, 3$). The universal joint is considered as two passive revolute joints with orthogonal axes. The joint components and links are flexible with the corresponding 6×6 stiffness matrices, which are obtained by the ANSYS software. It is noted the stiffness matrix of L_i depends on the distance between A_i and B_i when the prismatic joint is actuated, while the end-effector is assumed to be rigid. By associating the stiffness matrices of individual components, an analytical MSA-based stiffness model of the whole PKM can be achieved.

3 Results and Discussion

The translational and rotational stiffness values in *X*, *Y* and *Z* directions are shown in Fig. 2. It indicates the translational stiffness in *Z* direction is significantly higher than that in *X* and *Y* direction by about 2 to 7 times. Contrarily, the rotational stiffness in *Z* direction is much lower than that in *X* and *Y* directions. The averaged stiffness values on the lowest and highest planes of the workspace are listed in Table 1. The stiffness of the PKM under released and locked modes of the passive joints is analyzed and listed in Table 1. It reveals that locking joints A_i enhances the translational stiffness in *X* and

Y directions by over 40%. However, it also leads to a considerable decrease in the rotational stiffness along Z direction. Alternatively, when joints B_i are locked, a significant increase in the rotational stiffness is observed. The evidence assures the crucial influences of the passive joints on the stiffness of a PKM. The optimal orientation of the joint axes installed in a tilt angle of $35° - 40°$ from the vertical is also suggested.

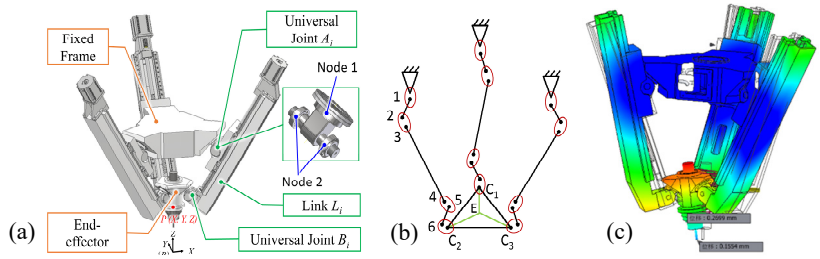

Fig. 1. A 3-UPU type PKM: (a)the configuration; (b)the schematic diagram of the MSA-based stiffness mode; (c)the stiffness analysis by adopting the FEM software.

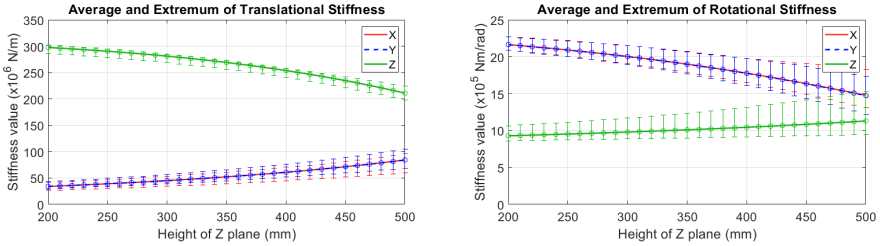

Fig. 2. The average and extremum values of the translational and rotational stiffness of the PKM.

Table 1. The effects of the joint mobility on the stiffness of the PKM.

Direction	Trans. X/Y		Trans. Z		Rot. X/Y		Rot. Z	
End-Effector's Position*	L	H	L	H	L	H	L	H
Stiffness (N μm^{-1}, N m rad^{-1})	34	84	297	211	22	15	9	11
Locking Joints A_i (%)	40	45	0	1	11	-1	-76	-30
Locking Joints B_i (%)	10	12	9	23	124	194	167	230

* L: $Z = 200$ mm, H: $Z = 500$ mm

Acknowledgement

This research was financially supported by the National Science and Technology Council, Taiwan. (NSTC 111-2221-E-007-068-MY2 and NSTC 112-2637-E-131-005). The authors also appreciate the assistance of Ms. Yi-Syuan Lee in this work.

References

1. Tang, T. F., Zhang, J.: Conceptual design and comparative stiffness analysis of an Exechon-like parallel kinematic machine with lockable spherical joints. International Journal of Advanced Robotic Systems (July-August), 1-13 (2017).
2. Klimchik, A., Pashkevich, A., Chablat, D.: Fundamentals of manipulator stiffness modeling using matrix structural analysis. Mechanism and Machine Theory 133, 365–394 (2019).

Toward Safe and Efficient Human-Robot Teams: Mixed Reality-based Robot Motion and Safety Index Visualization

Gustavo Alfonso Garcia Ricardez[1], Carl Törnberg[2], Lotfi El Hafi[1], Jorge Solis[2], and Tadahiro Taniguchi[1]

[1] Ritsumeikan University, Kusatsu 525-8577, Japan
[2] Karlstad University, Karlstad 651 88, Sweden

1 Introduction

Human-robot collaboration (HRC) is essential to address workforce shortages in aging societies like in Japan and Sweden. However, current HRC lacks effective synchronization between human and robot plans, leading to inefficiencies. Our research aims to improve communication and synchronization using mixed reality (MR) and Artificial Intelligence (AI). MR will visually convey robot plans, motions, and environmental data, while AI will interpret human input, generate robot responses, and adaptively plan the next step, with decisions conveyed via MR. Ultimately, we aim to test this framework in a collaborative assembly task, evaluating efficiency, safety, and human-centered metrics. This abstract focuses on MR-based visualization for robot motion and human safety, aiming to balance safety with efficiency.

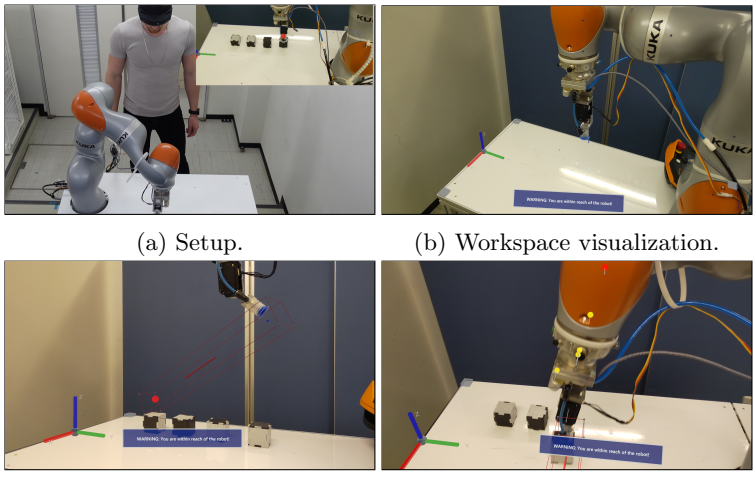

(a) Setup. (b) Workspace visualization.

(c) Workpiece occupancy. (d) Safety index visualization.

Fig. 1: Proposed system.

2 Proposed System

Our proposed system's hardware consists of a head-mounted display worn by the human and a robot arm with an end effector. The head-mounted display is the Microsoft HoloLens 2[1], the robot arm is the KUKA LBR iiwa 14 R820[2], which is equipped with a custom-made end effector developed by the team NAIST-RITS-Panasonic [1] for the Future Convenience Store Challenge, as shown in Fig. 1a. The robot is placed on a fixed base, and the workspace where the task takes place is also mounted on the base, as shown in Fig. 1b.

To display the robot's motion, the visualizer component subscribes to the topics corresponding to motion planning (i.e., MoveIt-related topics). From such information, the robot's goals are obtained and displayed to the human. Since the shape of the manipulated objects is typically known from sensor information or from *a priori* data, the object's shape is also displayed to the human to depict the soon-to-be-occupied region, as shown in Fig. 1c.

To display the human safety index, the visualizer component calculates the safety index of the Asymmetric Velocity Moderation (AVM) [2] method, as shown in Fig. 1d. AVM's safety index is obtained from the angle between displacement vectors (i.e., vectors from points on the robot and points on the human) and velocity vectors (i.e., relative velocity vectors between those points), as well as the distance between the human and the robot. In other words, AVM considers not only the distance but also the direction of the motion.

3 Ongoing Experiments

We will subjectively evaluate the user experience by controlling the amount and style of the displayed information when interacting with the robot. To do this, we place the human and the robot across a rectangular workspace. The robot picks and places cubes between predefined positions, while a human moves within the robot's reachable range. Moreover, we will measure the safety index and the proximity between the human and the robot. We expect to find the overall preferred settings to obtain motion and safety information that reduces the safety risks and allows the human to anticipate the robot's motion.

References

1. Garcia Ricardez, G.A., El Hafi, L., Ikeuchi, H., Yamamoto, M., Takamatsu, J., Taniguchi, T., Ogasawara, T.: Team NAIST-RITS-Panasonic at the Future Convenience Store Challenge: Our Approach from 2018 to 2021. Journal of the Society of Instrument and Control Engineers (SICE) 61(6), 422–425 (Jun 2022), https://doi.org/10.11499/sicejl.61.422
2. Garcia Ricardez, G.A., Yamaguchi, A., Takamatsu, J., Ogasawara, T.: Asymmetric Velocity Moderation for Human-safe Robot Control. RSJ Advanced Robotics (AR) 29(17), 1111–1125 (Sep 2015), https://doi.org/10.1080/01691864.2015.1034173

[1] https://www.microsoft.com/hololens

[2] https://www.kuka.com/products/robotics-systems/industrial-robots/lbr-iiwa

An Alternative Solution for Balancing of the 3-PRRR Fully-Isotropic Translational Parallel Robot

Mario Acevedo[1 [0000−00002−1433−8147]]

Universidad Panamericana. Facultad de Ingeniería.
Álvaro del Portillo 49, Zapopan, Jalisco, 45010, México.

The transmission of vibrations to the fixed frame, produced by the unbalanced inertia forces, increase the shaking force and shaking moment. Removing or decreasing these alternating dynamic loads is desirable. This has been solved in different ways. These methods generally imply a considerable increment in the system's mass. A different approach, based on planning the displacements of the total CoM of the system, has been applied recently to balancing a fully-isotropic translational parallel robot called orthoglide, [1].

In this work, this approach is resumed using fully Cartesian coordinates. A method already applied for balancing a planar parallel manipulator, [2]. In this way, joints are defined with no constraint equations while keeping moderate the number of variables. This modeling technique is applied for the balancing of the 3PRRR Fully-Isotropic Translational Parallel Robot, see Fig. 1, introduced in [3]. The expressions to calculate the general CoM, the shaking force, and the shaking moment of the system are obtained in a direct and automated way. The force balancing conditions, directly expressed in terms of the local coordinates of the CoM of the bodies, are obtained directly from the terms in the mass matrix, contributing to making the optimal control of the robot-manipulator CoM faster and easy to perform.

The global CoM ($\mathbf{g}$), the linear momentum ($\mathbf{l}$), and the angular momentum ($\mathbf{h}$) are all expressed as a function of the system's mass matrix and of the global Cartesian coordinates:

$$m\mathbf{g} = \mathbf{M}\mathbf{q} \tag{1}$$

$$\mathbf{l} = m\dot{\mathbf{g}} = \mathbf{B}\mathbf{M}\dot{\mathbf{q}} \tag{2}$$

$$\mathbf{h} = \tilde{\mathbf{q}}\mathbf{M}\dot{\mathbf{q}} \tag{3}$$

respectively. Where m is the system's mass, $\dot{\mathbf{g}}$ is the CoM velocity, $\mathbf{M}$ is the system's mass matrix assembled from the mass associated with the basic points, whose coordinates form the vector of positions $\mathbf{q}$, and its derivative the vector of cartesian velocities $\dot{\mathbf{q}}$. $\mathbf{B}$ is a matrix introduced here to arrange the terms of the matrix multiplication and is composed of (3×3) identity matrices. Finally, $\tilde{\mathbf{q}}$ is a column vector representing the vector product of the position of each basic point times its corresponding linear momentum. These expressions are used for the force balancing of the mechanisms applying the method based on

the optimal control of the global CoM of the manipulator. The acceleration of the global CoM is reduced using the "bang-bang" law, proposing to partially balance the manipulator without adding supplementary masses.

The shaking force $\mathbf{f}_{sh}$, calculated as:

$$\mathbf{f}_{sh} = \mathbf{B}\mathbf{M}\ddot{\mathbf{q}} \tag{4}$$

and the shaking moment, which depends on the coordinate's accelerations solely, obtained by:

$$\tau = \tilde{\mathbf{q}}\mathbf{M}\ddot{\mathbf{q}} \tag{5}$$

are used to verify the behavior of the mechanism before and after the force balancing. All the procedure is illustrated through a numerical example, and the results obtained are verified by simulation.

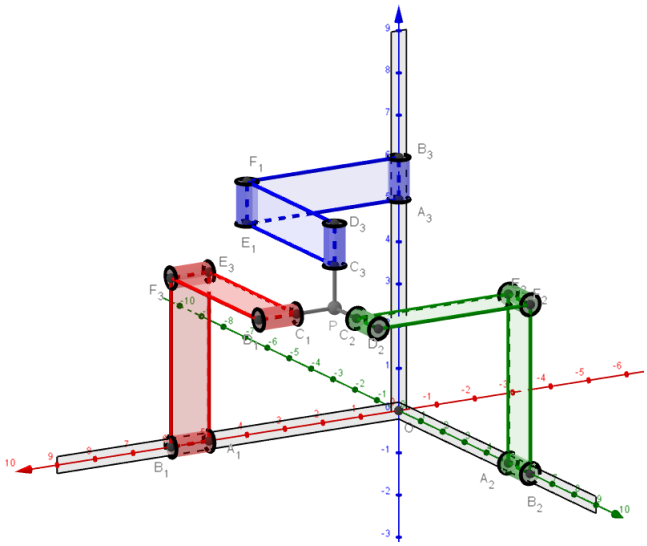

Fig. 1. A representation of the 3PRRR Fully-Isotropic Translational Parallel Robot. Point P represents the end-effector.

References

1. Geng, J., Arakelian, V., Chablat, D., Lemoine, P.: Balancing of the Orthoglide Taking into Account Its Varying Payload. Robotics **10**, 30, (2021)
2. Acevedo, M., Orvañanos-Guerrero, M.T., Velázquez, R., Arakelian, V. An Alternative Method for Shaking Force Balancing of the 3RRR PPM through Acceleration Control of the Center of Mass. Appl. Sci. **10**, 1351 (2020)
3. Gogu, G. Structural synthesis of fully-isotropic translational parallel robots via theory of linear transformations, European Journal of Mechanics - A/Solids, **23**(6), 1021–1039, (2004)

A Novel Approach to Occupancy Grid Map Merging in Environments with Highly Repetitive Features

Chung-Jui Lai and Kuei-Yuan Chan[1]

Department of Mechanical Engineering,
National Taiwan University, Taipei 10617, Taiwan,
chanky@ntu.edu.tw

1 Background and Motivation

In this work, we focus on deploying a group of robots to explore a space and reconstruct the map by sensing their surroundings and combining the information gathered. Individual maps can be merged through direct or indirect methods, as overviewed by Lee [1]. Direct methods, as described in [2], use multiple RGB images to compute the Map Transformation Matrix (MTM) by matching common 2D visual objects detected by a camera. Although they are not limited by environmental constraints, they require significant data storage. On the other hand, indirect methods use previously constructed maps for feature extraction and matching to calculate the MTM, thus reducing storage requirements. However, in scenarios such as large warehouses and factories where features extracted for map merging are highly repetitive, existing methods, regardless of whether they are direct or indirect, are unable to be effective. Fig.1 illustrates this issue, where a significant number of feature matches are incorrect, making merging impossible. We propose a modified map merging technique with communication strength inspired by a mechanism to overcome this limitation. Several studies, including the case shown in Fig.1, are used to demonstrate how our approach works in detail.

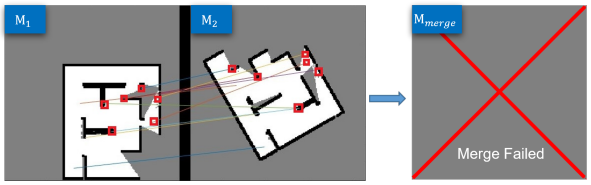

Fig. 1. The diagram shows feature matching in a highly repetitive feature environment. Incorrect feature matches are marked in red, resulting in failed map merging.

2 Proposed Methodology

Our proposed method utilizes communication signal strength to estimate the relative distance between two robots and merge their maps by calculating the MTM based on the kinematic motion analysis. The kinematic motion analysis treats two maps and relative distance at multiple time points as a link with less than one degree of freedom to achieve map merging. However, the MTM may contain inaccuracies due to signal noise. To detect errors in the MTM, we apply an Acceptance Index and modify Ferrão et al.'s feature method in [3] to correct the MTM if the error is unacceptable. This modification includes changing unique

feature matching to non-unique matching and adding rotation/translation constraints in the MTM calculation. Fig.2 shows the flowchart of our proposed process. As can be seen the process provides the merged map once the error of the corrected MTM is acceptable.

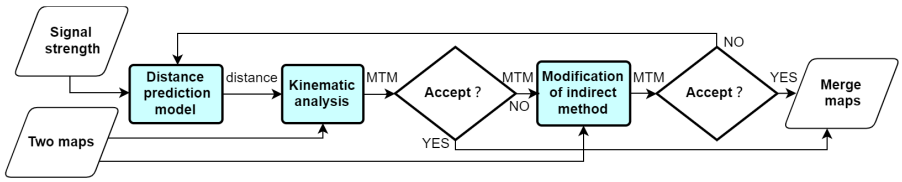

Fig. 2. Flowchart of proposed method.

3 Results and Discussion

Our proposed method was tested on four highly repetitive feature environments, and successful map merging results were obtained. One of the merged maps is shown in Fig.3. In contrast to existing merging techniques, as shown in Fig.1, our method provides a result with an Acceptance Index of 0.9736. This indicates that 97.36% of the overlapped areas are correctly matched. The application of our method enables the deployment of multiple robots with unknown initial locations in high repetitive feature fields. However, it should be noted that our method requires the resolution of both maps to be the same.

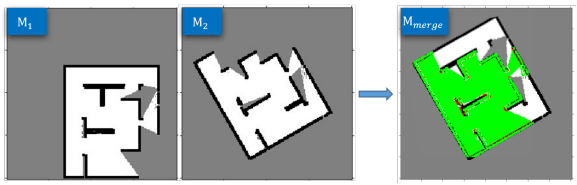

Fig. 3. The merged result of highly repetitive feature maps in this study. Green represents same-color overlaps, red represents different-color overlaps.

Acknowledgement

This work was supported by the National Science and Technology Council of Taiwan under grant MOST 110-2221-E002-136-MY3.

References

1. Lee, Heon-Cheol, et al. "A survey of map merging techniques for cooperative-SLAM." 2012 9th International Conference on Ubiquitous Robots and Ambient Intelligence (URAI). IEEE, 2012.
2. Lee, H. C. "Implementation of a network-based robot system for cooperative recognition and localization of multiple objects." Proc. IEEK Summer Conf.. 2012.
3. Ferrão, Victor Terra, Cássio Dener Noronha Vinhal, and Gelson da Cruz. "An occupancy grid map merging algorithm invariant to scale, rotation and translation." 2017 Brazilian Conference on Intelligent Systems (BRACIS). IEEE, 2017.

Human-Robot Collaboration Based on Robot Motion Planning with Adaptive Obstacle Avoidance

Hao Jian Eugene Tong[1], Brijesh Patel[1], Yan-Cen Lin[1], Zhi-Lin Zhang[1], Chao-Yi Lin[1], Chao-Lung Yang[2], Ching-Yuan Chang[3], and Po Ting Lin[1,4,*[0000-0001-5907-7828]]

[1] Department of Mechanical Engineering, National Taiwan University of Science and Technology, Taipei 10607, Taiwan
[2] Department of Industrial Management, National Taiwan University of Science and Technology, Taipei 10607, Taiwan
[3] Department of Mechanical Engineering, National Taipei University of Technology, Taipei 10608, Taiwan
[4] Intelligent Manufacturing Innovation Center, National Taiwan University of Science and Technology, Taipei 10607, Taiwan
*Corresponding Author's email: potinglin@mail.ntust.edu.tw

Abstract. Human-Robot Collaboration (HRC) has the potential to revolutionize various industries by improving performance, productivity, and safety. However, ensuring safety in the collaborative workspace is crucial. To address this, a classification system for safety standards for industrial robotics has been established by ISO 10218. This paper proposes a Human Robot Collaboration Index (HRCI) to enhance efficiency, ability, and safety of human workers in scenarios where current robots are inadequate. The HRCI system adjusts robots' safety thresholds based on the specific task being performed, promoting productive and efficient collaboration between humans and robots. The methodology involves using a 3D camera for skeleton recognition of human motion, followed by the Spatial-Temporal Graph Convolutional Network (ST-GCN) to identify human motion sequence with the analysis of therbligs. The robot's movement speed and obstacle avoidance threshold are adjusted based on the task at hand. When human motion and robot movement are supposed to be close, robot movement slows down, maintaining a lower but safe threshold of obstacle avoidance to enable gentle contact with the human. Conversely, when humans should not be near the robot, it maintains a higher level of obstacle avoidance and avoids contact. This approach optimizes the efficiency of robot motion and safety to the surrounding workers and environment simultaneously. The proposed HRCI system offers a promising solution to the challenges posed by traditional collision avoidance methods, promoting human-robot collaboration while ensuring safety.

Keywords: Human-Robot Collaboration (HRC), Spatial-Temporal Graph Convolutional Network (ST-GCN), Robot Motion Planning with Obstacle Avoidance.

1 Process Flow of the Proposed Method

As shown in Fig. 1, the proposed method was implemented in a Human-Robot Collaboration (HRC) application where a robot arm was to deliver an item to the human

worker. A 3D camera (RGBD) was utilized to capture the 3D skeleton of human motion by mapping the acquired MediaPipe skeleton [1] to the 3D point cloud. The Spatial-Temporal Graph Convolutional Network (ST-GCN) [2] was developed to classify the human motion based on the analyses of therbligs. A Human-Robot Collaboration Index (HRCI) was proposed to specify how the robot was supposed to work with human. The following formulation [3, 4] was used to find the optimal robot trajectory with adaptive upper limit of collision safety.

$$\text{Min} \quad \sum_i \left\| \mathbf{x} - \mathbf{x}_{\mathrm{T},i} \right\| \quad \text{s.t.} \quad D(\mathbf{x}, \mathbf{O}) \le \bar{D} \tag{1}$$

where $\mathbf{x}$ is the design variable of robot joints; $\mathbf{x}_{\mathrm{T},i}$ is the i^{th} point on the original trajectory; $\mathbf{O}$ is the coordinate of the obstacle; D is the danger level of collision; $\bar{D}$ is the upper limit of danger level to be adaptively adjusted based on the determined HRCI. Lower $\bar{D}$ keeps a greater safety distance between human and robot. Properly increased value of $\bar{D}$ allows the robot to keep a closer distance from human, thus HRC could be appropriately achieved.

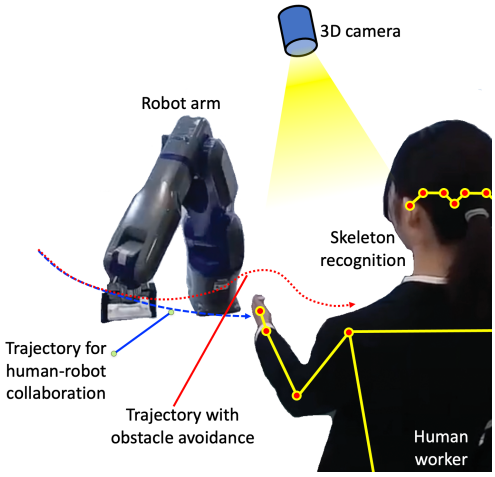

Fig. 1. Proposed method of robot motion planning with adaptive obstacle avoidance based on Human-Robot Collaboration Index (HRCI).

References

1. Lugaresi, C., Tang, J., Nash, H., McClanahan, C., Uboweja, E., Hays, M., Zhang, F., Chang, C.-L., Yong, M., Lee, J.: Mediapipe: A framework for perceiving and processing reality. In: Third Workshop on Computer Vision for AR/VR at IEEE Computer Vision and Pattern Recognition (CVPR), Long Beach, CA, USA (2019).
2. Yang, C.-L., Setyoko, A., Tampubolon, H., Hua, K.-L.: Pairwise adjacency matrix on spatial temporal graph convolution network for skeleton-based two-person interaction recognition. In: 2020 IEEE International Conference on Image Processing (ICIP), 2166-2170 (2020).
3. Lin, C.-Y.: Robot Arm Path Planning Based on Obstacle Occupancy Modeling and Trajectory Reliability Optimization. MS Thesis, Department of Mechanical Engineering, National Taiwan University of Science and Technology, Taipei, Taiwan (2021).
4. Zhang, Z.-L.: Robot Arm Path Planning with Obstacle Aviodance Based on Obstacle Occupancy Random Forest Model and Lagragian Minimization. MS Thesis, Department of Mechanical Engineering, National Taiwan University of Science and Technology, Taipei, Taiwan (2022).

Body Gesture Recognition for Collaborative Robots

Jorge Solis[1][0000-0002-6865-7346], Koyu Nakamori[1],
Gustavo Alfonso Garcia Ricardez[2][0000-0001-6518-577X] and Johan Håkansson[3]

[1]Karlstad University, Karlstad, Sweden
[2]Ritsumeikan University, Kyoto, Japan
[3]Goodtech Solutions AB, Karlstad, Sweden
solis@ieee.org

1 Introduction

One of the main reasons for using collaborative robots is to improve the efficiency of today's manufacturing technology. They will increasingly work side by side with humans, which requires a completely different safety paradigm. In this research, we aim to implement novel sustainable solutions based on collaborative robots using mixed reality and artificial intelligence.

2 Gesture Recognition System for Collaborative Robots

Gesture is one of the most well-known non-verbal communication tools by using body motions. Hazegawa et al. [1] introduced a generic method that utilizes gaze and surrounding environment information for recognizing grasp intention. Solis et.al. [2] developed a robot vehicle for carrying-medical tools with 3D gesture recognition system by using time-delay neural network. In this work, we applied the 3D gesture recognition system [2] for collaborative robots to send commands to the robot. This will make workers more comfortable to work and we implemented a function to get robot status (e.g. its speed, etc.) which enables a bi-directional human-robot interaction.

3 Integrated System Overview

The camera is installed on top of the IRB 14000 YuMi® (Fig. 1a). The height of the camera is adjusted to show above a person's knees. The camera is connected to a mini-PC, which is then connected to robot controller by an Ethernet cable.
We selected PC SDK because this is the most suitable to our work and easy to implement. PC SDK allows connecting to the robot controller and sending command directly (see Fig. 1b) from PC to the controller by using methods written in C#. In order to communicate the recognized gesture, we made a robot communication module to connect and send commands to the robot controller (Fig. 1a). We implemented a simple assemble task to the robot. In this task, the robot grabs a cup with one hand and an eraser with the other one and places the eraser inside the cup (Fig. 1a).

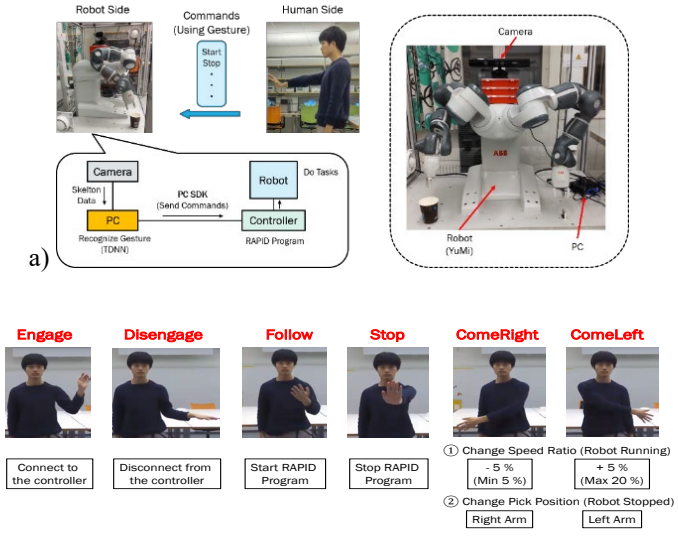

Fig. 1. a) Integrated system overview, b) Mapping between recognized gestures and commands

4 Preliminary Experiments and Results

An experimental procedure was prepared in which all gestures were performed at least once, and four volunteers were asked to perform it. The time taken for them to complete a proposed procedure was measured (*engage→come right→come left→follow→stop*). Each subject was asked to repeat the task three times and the results are shown in Table 1. Subjects #2, #3 and #4 generally completed the test smoothly, but subject #1 took significantly longer due to gestures were not being recognized. However, the task took considerably less time the second and third times.

Table 1. Time for each volunteer to perform the procedure.

Trial	Subject 1	Subject 2	Subject 3	Subject 4
1st [min]	8:04	1:45	1:26	2:01
2nd [min]	2:39	1:29	1:24	1:49
3rd [min]	2:00	1:57	1:32	1:54

References

1. Hasegawa, Y., et al., Natural grasp intention recognition based on gaze in human-robot interaction, IEEE journal of Biomedical and Health Informatics, vol. 27(4), pp. 2059-2070 (2023).
2. Solis, J., Amaral, F. (2017). Denoising of human motion data for a 3D gesture recognition system for a two-wheeled inverted pendulum robot, IEEE International Conference on Advanced Intelligent Mechatronics, pp. 43-4

Stem detection using depth camera in red perilla farm

Seito Takeuchi[1], Shunsuke Komizunai[2], Taku Senoo[1], and Atsushi Konno[1]

[1] Graduate school of Information Science and Technology, Hokkaido University, Sapporo, Japan,
{takeuchi@scc, senoo@ssi}.ist.hokudai.ac.jp,
[2] Faculty of Engineering and Design, Kagawa University, Takamatsu, Japan

1 Introduction

Since weeds have negative impacts on crop growth, weeding is an essential task. When weeding with a robotic hand, part of a weed may remain depending on the grasping position. Therefore, it is necessary to detect a stem of weed as an appropriate grasping position. A method that uses deep learning to segment weeds and detect stem positions [1] requires pixel-wise labeling of the images in the dataset, which takes a lot of time and effort. This study proposes a method that detects a weed stem position using YOLOv7 [2] and image processing.

2 Method

The proposed method has two stages. First, bounding boxes indicating weed areas are extracted using YOLOv7. Segmentation is then performed on each bounding box to separate the weeds from the background. Following this, image processing is used to find the location of the stem. In this study, Intel RealSense Depth Camera D435i was used to capture the RGBD images.

2.1 Weed detection using YOLOv7

One of the object detection methods, YOLOv7, was used for weed detection. The object detection performance of YOLOv7 outperforms the conventional YOLO series in both accuracy and speed. As both real-time performance and detection accuracy are important for weed detection, YOLOv7 was selected for this study. The model of YOLOv7 was trained with a total of 1000 images, 100 for each species, for a total of 10 species of red perilla and 9 weeds observed on the farm.

2.2 Stem detection using image processing

From top left to bottom right, Figure 1 shows the process of stem detection after weed detection. First, the green color of the weeds is extracted by specifying a range of hues (a*) in the L*a*b* color space. Next, the leaves of the weed are separated by gradually moving the outline of the weed inwards. Then each leaf is

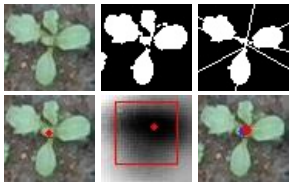

Fig. 1. Process of stem detection

Table 1. Comparison of performance

Method	Precision	Recall
Center of BBox	0.768	0.883
Line fitting	0.754	0.867
Proposed method	0.870	0.870

fitted with a straight line. The coordinates of the centroid of the figure enclosed by these lines are taken as stem position 1. The area around the coordinates corresponding to stem position 1 is then searched in the depth image and the nearest point is taken as stem position 2. Finally, the midpoint between stem position 1 and stem position 2 is detected as the final stem position.

3 Results and Discussion

Precision and recall were used to evaluate the stem detection performance. To verify the effectiveness of the proposed method, a comparison of the three cases is shown in Table 1. From top to bottom, the results are shown when the center of the bounding box is detected as the final stem position, when the result of stem position 1 is detected as the final stem position, and when the proposed method combining line fitting method and depth image search method is used to detect the final stem position. The proposed method achieved higher accuracy by combining the two method than when using the center of the bounding box as the final stem position or when using line fitting method alone.

4 Conclusions

In this study, a method of stem detection was proposed. The proposed method detects weeds using YOLOv7, and then detects the stem position using only a combination of simple image processing. This simplifies the preparation of the dataset compared to deep learning-based methods for detecting stem positions. The accuracy of stem detection needs to be further improved in the future.

Acknowledgment

We appreciate the support of Mishima Foods Co., Ltd. and Hiroshima University.

References

1. X. Zhang, et al.: "A Unified Model for Real-Time Crop Recognition and Stem Localization Exploiting Cross-Task Feature Fusion," *2020 IEEE International Conference on Real-time Computing and Robotics (RCAR)*, pp.327–322, 2020.
2. Wang, C.Y., et al.: "YOLOv7: Trainable bag-of-freebies sets new state-of-the-art for real-time object detectors." http://www.ncbi.nlm.nih.gov

Vacuum-powered and fabric-based soft actuator

Lola Courty and Kenjiro Takemura

Keio University, 3-14-1 Hiyoshi, Kohoku-ku, Yokohama, Kanagawa 223-8522, Japan
takemura@mech.keio.ac.jp

In the past few years, pneumatic artificial muscles (PAMs) have been widely considered in the field of soft robotics. Inherently compliant, they offer high speed, large deformation and actuation stress, and high force to weight ratio at a relatively low cost. It therefore promises a safe and powerful actuation for a multitude of applications. Usually, they involve a bladder that expands upon pressurization, with strain-limiting components to guide the deformation and achieve complex motions. Those PAMs operate with positive pressure. However, vacuum-powered artificial muscles (VAMPs) have recently gained interest as they can exhibit equivalent range of motions, most often at larger contraction ratios, in constrained space, hence offering greater safety and compactness. A previous study [1] on VAMPs has introduced a *Fluid-driven Origami Artificial Muscle* (FOAM) which consists of a compressible zigzag-like skeleton, encased in a tight nonstretchable skin. The role of the skeleton is to guide the deformation induced by depressurizing the actuator, with the caveats that the skeleton can unpredictably buckle or slide, hindering its movement and force induced, as well as reproducibility over extended use [2].

For this work, an improved version of FOAMs is designed and characterized, having in mind an application in hand rehabilitation. The actuator proposed here is a small fabric-based soft actuator, whose skeleton is fixed to both ends to avoid sliding. It operates on low vacuum pressure (<80 kPa), and is, to mimic the flexion of a hand joint, a bending actuator.

To manufacture the actuator, a skeleton is 3D printed using flexible resin (*Flexible 80A, Formlabs*). The design consists of an asymmetric zigzag; only one side can contract while the other can merely expand. Then, it is inserted into a TPU-coated nylon fabric tube (170 g/sqm), and a string is looped and tightened around both ends in grooves dug into the skeleton. Beforehand, to make the tube, two sheets of fabric are cut, with one larger than the other, and heat sealed on both same-length sides. Traditionally, a single sheet is rolled and adhered to itself. We, however, heat-seal a sheet of fabric upon a flat shorter one to easily creates a cavity into which the skeleton can be inserted. In addition, it helps the bending movement by using the fabric inherent stiffness. Finally, an air inlet is encased into one end of the skeleton and sealed using an adhesive (*Aquaseal, GEAR AID*) to avoid leaks.

The actuator is characterized in terms of angular displacement and blocked tip force upon depressurization. The latter is realized via a 60 mL syringe mounted on a motorized linear stage to achieve repeatable pressure values. To determine the angular displacement, the actuator is hung, with a colored pin

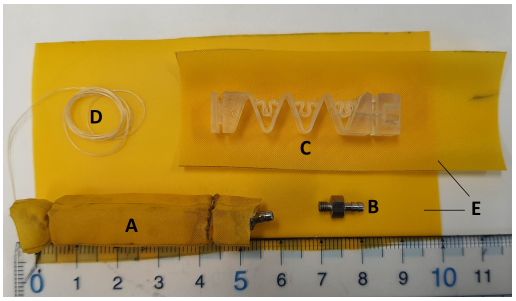

Fig. 1. 45-mm actuator (A) components: air inlet (B), skeleton (C), thread (D), and fabric (E)

attached to its other end to track the displacement. A camera is placed in front of the actuator, perpendicular to the motion plane. The bending angle is defined as the angle between the tracked end initial and final positions, with the origin set at the fixed end. The blocked tip force was measured by steadily increasing vacuum, with a customized force measurement setup, inspired from a previous study [3]. One end of the actuator is fixed, while the other is lying upon a weighting scale, and a constraining plate is placed above the actuator. Therefore, the non-linear effects induced by bending are limited.

With a 45-mm actuator (Fig. 1), the bending angle reaches 50° at -50 kPa. The displacements are consistent and reproducible, and a small hysteresis can be observed when the actuator is repressurized to reach its initial state. To achieve a larger bending angle, the skeleton must be longer: for instance, for a 100-mm long actuator, 75° is reached at -50 kPa. The blocked tip force obtained at -50 kPa is about 1 N, and 1.4 N at -80 kPa for the 45-mm actuator. To increase the blocked tip force, the cross-section of the actuator can be enlarged.

This actuator is a demonstration of the FOAM concept: depending on the design of the skeleton, various motions can be achieved. Our new technique to close the outer membrane with thread enables direct contact with the ends of the skeleton, therefore allowing personalized extrema, and facilitating the integration of the actuator.

References

1. Li, S., Vogt, D.M., Rus, D., Wood, R.J: Fluid-driven origami-inspired artificial muscles. Proc. Natl. Acad. Sci. USA, 114, 13132–13137 (2017). doi:10.1016/0022-2836(81)90087-5
2. Mendoza, M.J., Gollob, S.D., Lavado, D., Koo, B.H.B., Cruz, S., Roche, E.T., Vela, E.A.: A Vacuum-Powered Artificial Muscle Designed for Infant Rehabilitation. Micromachines, 12, 971 (2021).doi:10.3390/mi12080971
3. Polygerinos, P., Wang, Z., Overvelde, J. T. B., Galloway, K. C., Wood, R. J., Bertoldi, K., et al: Modeling of soft fiber-reinforced bending actuators. IEEE Trans. Robot. 31, 778–789. (2015) doi:10.1109/TRO.2015.2428504

Accuracy Criteria for Planar Flexures

Matteo Verotti, Simone Serafino, and Pietro Fanghella

University of Genoa
Department of Mechanical, Energy, Management and Transportation Engineering,
Via all'Opera Pia, Genoa, Italy 16145

In the last decades, compliant mechanisms have been widely implemented in a variety of precision engineering applications. While many studies focused on analysis and synthesis methods [1], limited results regarding the analysis of the accuracy criteria have been presented. According to the rigid-body replacement method [2], the substitution of a revolute joint with a compliant element determines a relative motion between the connected bodies that generally differs from the nominal rotation around the axis of the kinematic pair, phenomenon often called *center* or *axis drift*. In literature, various criteria to evaluate the position accuracy of flexures have been proposed [3]. These criteria are briefly illustrated in Fig. 1 in case of a uniform flexure, where the position accuracy is evaluated as the magnitude of the vector that defines the position of a specific point associated to the deformed configuration with respect to the nominal center of rotation of the flexure, C^r, coincident to the trace of the revolute joint axis.

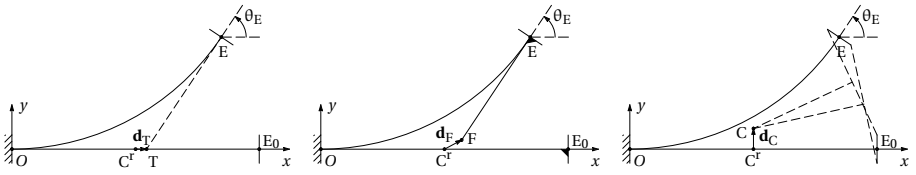

Fig. 1: Position accuracy criteria: end-section tangent (a), rigid-body (b), and pole of the displacement (c).

Figure 2(a) shows a cross-axis flexural pivot with straight flexure elements intersecting at their midpoint with crossing angle $\beta = \pi/4$ rad. Figure 2(b) reports the trends of the end-section tangent, rigid-body, and pole of the displacement criteria for a platform rotation up to $\phi = \pi/2$ rad, evaluated by performing finite element simulations with the commercial software Ansys.

The position accuracy criteria can be considered as a useful tool for designing high-accuracy compliant systems. The cross-axis pivot depicted in Fig. 2(a) is adopted as a starting reference design to be improved, and the parameter d_C is used to evaluate the system accuracy. In a previous investigation [4], it was demonstrated that accuracy of cross-axis pivots strongly depends on flexures initial curvature and orientation, represented through the design parameters 2α and β, respectively, in Fig. 3(a). The study considered initially-curved elements positioned in such a way their centroids were coincident. Figure 3(b) shows the accuracy design map generated evaluating the accuracy $d_C^{(2\alpha)}$ and $d_C^{(0)}$ of the curved and straight pivots, respectively, for a

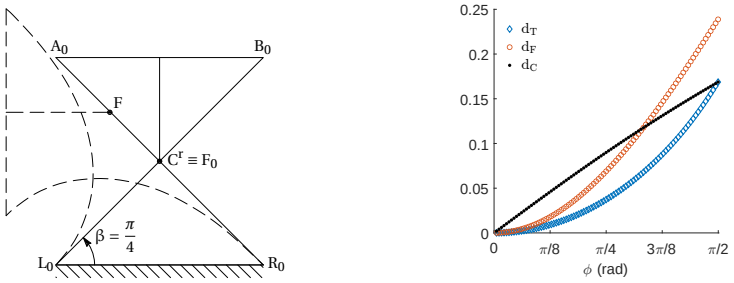

(a) (b)

Fig. 2: Cross-axis flexural pivot in neutral (solid) and deformed ($\phi = \pi/2$, dashed) configurations (a); trends of accuracy parameters for increasing rotations ϕ (b).

platform rotation $\phi = \pi/4$. Colored dots represent the α-β configurations for which the ratio $\tilde{d} = d_C^{(2\alpha)}/d_C^{(0)} < 1$, therefore determining an accuracy improvement with respect to the straight case. It can be noted that accuracy improvements about 20% can be achieved in the left-bottom region, for relatively small values of α and β. Higher accuracy performance can be obtained in the right-upper region, that correspond to curved cross-axis pivots with strong curvature and orientation. For example, the configuration with $\bar{\beta} = 0.513$ rad and $\bar{\alpha} = 1.032$ rad achieves an accuracy ratio $\tilde{d} = 0.74$. Hence, the corresponding curved cross-axis, reported in Fig. 3(a), is 26% more accurate with respect the straight cross-axis reported in Fig. 2(a).

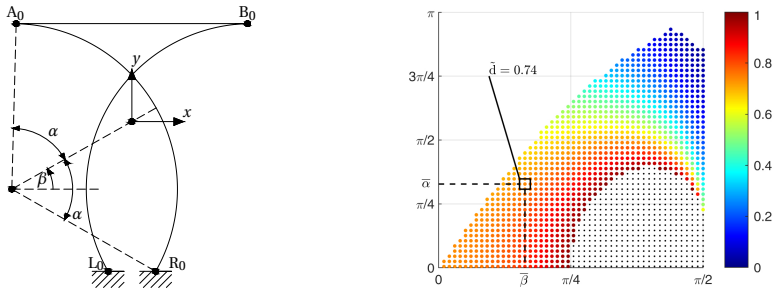

(a) (b)

Fig. 3: Curved cross-axis pivot with $\bar{\beta} = 0.513$ rad and $\bar{\alpha} = 1.032$ rad (a); accuracy design map corresponding to $\phi = \pi/4$ (b), β and α in radians.

References

1. Liu, Y., Zhang, Z.: A large range compliant XY nano-manipulator with active parasitic rotation rejection. Precision Engineering 72, 640–652 (nov 2021)
2. Mattson, C.: Handbook of compliant mechanisms, chap. Synthesis through Rigid-Body Replacement, pp. 109–121. John Wiley & Sons (2013)
3. Verotti, M., Serafino, S., Fanghella, P.: Position accuracy criteria for planar flexural hinges. Precision Engineering 80, 82–94 (2023)
4. Serafino, S., Fanghella, P., Verotti, M.: Initial curvature and centroid positioning effects on cross-axis flexural pivots accuracy. Mechanism and Machine Theory 177, 105039 (nov 2022)

Dynamic Task Capability based Task Allocation for Collaborative Manipulation

Keshab Patra[1], Arpita Sinha[1], and Anirban Guha[1]

[1] Indian Institute of Technology Bombay, Mumbai 400076, India,
Keshabpatra19@gmail.com

Collaborative mobile manipulators have an advantage over single manipulators for tasks requiring dexterity, e.g., transporting heavy or oversized payload and fixture-less multipart assembly. This advantage comes with the cost of complexity in robot coordination, communication, and task allocation, especially while manipulating an unknown object in a cluttered environment. The manipulators should suitably share the task for optimal task capability, resource allocation, and maximum fault tolerance. Hence it is essential to quantify the dynamic task capability of the individual members, the entire group and allocate the task equitably. This work introduces a computationally efficient cooperative task capability finding method and a corresponding dynamic task allocation scheme.

Task-space force and manipulability ellipsoids are defined [1] for cooperating manipulators grasping a rigid object where the task/load sharing among them is constant and predefined. It leads to inefficient utilization of the capabilities of the manipulators. A coupled inverse dynamic-based technique has been reported for computing the dynamic load-carrying capacity of multiple cooperating manipulators in the joint space using D' Alembert's principle [3], ignoring the inertia properties of the object and the end effector (EE). Analytical and optimization-based methods [2] for force capabilities computation require high computational time and do not scale well when used for many manipulators, making it incapable of real-time operation.

We reformulate the task capability finding formulation of the manipulator based on the force polytope proposed by Yoshikawa [5] that defines the map between the joint actuator torque $\boldsymbol{\tau}$ and the external wrench $\boldsymbol{h}$ at the EE is $\boldsymbol{J^T h} = \boldsymbol{\tau}$. The task capability of $i-th$ manipulator is computed online using Eqn. (1) for each time instant as a scalar multiplier k_i of the desired wrench $\boldsymbol{h_o}$ for the task completion in the task space considering the manipulator's dynamics $\boldsymbol{\tau_i'}$ and the joint torque limitations $\boldsymbol{\tau_{i,max}}$. The sum of the individual manipulators' task capabilities provides the group's total capability $K = \sum k_i$, where K is the scaling parameter of the total task $\boldsymbol{h_o}$. The individual manipulators share the task proportional to their task capabilities k_i obtained using efficient utilization of a manipulator. Dynamic task allocation coefficient $\beta_i = k_i/K$. The task share by $i-th$ manipulator for the task would be $\beta_i \boldsymbol{h_o}$.

$$\begin{aligned} &\max\ k_i \\ &s.t.\quad \left|\boldsymbol{\tau_i'} + k_i \boldsymbol{J_i^T}(\boldsymbol{q})\boldsymbol{h_o}\right| \le \boldsymbol{\tau}_{i,max} \\ &\qquad\quad k_i > 0 \end{aligned} \tag{1}$$

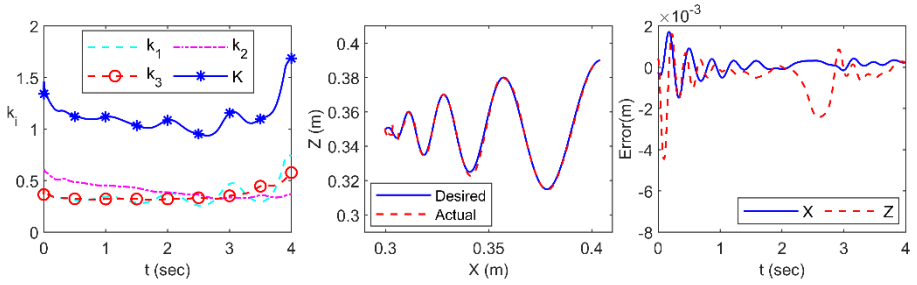

Fig. 1 (a) The task capability of the three manipulator arms k_1, k_2, k_3 and the total task capability K, (b) 2-D path tracing by the center of mass of the manipulated object, and (c) Trajectory tracking performances.

Numerical studies on three manipulators performing a task of trajectory tracking by the object's center of mass, indicate the efficacy. The diverging sinusoid-like trajectory $[0.3 + 0.01t + 0.001t^3, 0, 0.35 + 0.01tcos(2\pi t)]^T\ m$ is considered here. All EEs rigidly grasped the object on its periphery. The proposed method efficiently computes online task capabilities 85% faster than the existing vertex search-based state-of-art capability finding algorithm [4] and dynamically allocates the task for efficient utilization of the capability. The trajectory tracking performance in Fig. 1 shows the efficacy of the proposed metric. Near $t = 2.5\ sec$ (Fig. 1. (a)) when the value of K (0.93) goes below one the trajectory tracking performance deteriorated, evidenced by Fig.1 (c). For successful task completion, the total capability (K) should be greater than one at every instant. The trend of trajectory tracking error matches with the predictions of the proposed metric. The task capability aids in identifying the least capable manipulator for the task. Identifying such a least capable one amongst a group of manipulators assists in the efficient utilization of the capability of the group.

References

1. Chiacchio P, Chiaverini S, Sciavicco L, Siciliano B (1991) Task space dynamic analysis of multiarm system configurations. The International Journal of Robotics Research 10(6):708–715
2. Mejia L, Simas H, Martins D (2015) Force capability in general 3dof planar mechanisms. Mechanism and Machine Theory 91:120–134
3. Sheng Zhao Y, Lu L, Shi Zhao T, Hui Du Y, Huang Z (1999) The novel approaches for computing the dynamic load-carrying capacity of multiple cooperating robotic manipulators. Mechanism and Machine Theory 34(4):637–643
4. Skuric A, Padois V, Daney D (2021) On-line force capability evaluation based on efficient polytope vertex search. In: 2021 IEEE International Conference on Robotics and Automation (ICRA), pp 1700–1706, DOI 10.1109/ICRA48506.2021.95620
5. Yoshikawa T (1985) Manipulability of robotic mechanisms. The International Journal of Robotics Research 4:3–9

Experimental research of a parallel manipulator in a singular configuration

Jacek Bałchanowski[0000-0002-1510-0122] and Sławomir Wudarczyk[0000-0003-4953-4516]

[1] Wrocław University of Science and Technology, Wrocław, Poland
jacek.balchanowski@pwr.edu.pl,slawomir.wudarczyk@pwr.edu.pl

1 Materials and methods

Mechanism links can assume kinematically indeterminate positions during operation. Such positions of the mechanism are commonly called singularity configurations. A system brought to such a configuration changes its kinematic and dynamic properties. Singular configurations of parallel manipulators are configurations at which the robot loses its natural rigidity. At these configurations, one or more degrees of freedom of the platform become uncontrollable [2, 4, 5].

A 3RUU parallel manipulator with 3 DoF near a singular position described by an angle $q_{(0)} = 27.65$o was subjected to stand tests (Fig. 1). The singular configurations of this system were determined analytically [1, 3].

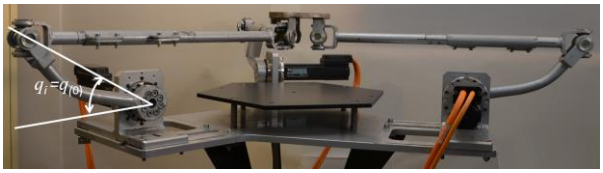

Fig. 1. View of the 3RUU manipulator in the analyzed singular configuration

The experimental study measured the platform's positioning accuracy near the singular configuration depending on the qi drive settings. The tests consisted of placing the manipulator in the q_i measurement position and measuring the deflection u_z of platform under the load of the force $\boldsymbol{F}_i$ caused by the mass m_i. The scheme of the experiment and measurements is shown in Fig. 2.

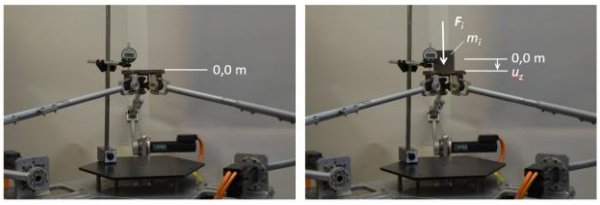

Fig. 2. Views of the stand and diagram of how to carry out the measurements of the deflection of the manipulator platform: a) unloaded platform, b) loaded platform

The tests were conducted in the range $q_{(0)} \leq q_i \leq 90^o$. Measurements were made for three different loads on the platform with forces $\boldsymbol{F}_1$ = 14.70 N, $\boldsymbol{F}_2$ = 29.40 N,

$\boldsymbol{F}_3$ = 75.50 N. Analyzing the results, it can be seen that as the platform approaches the singular position $q_{(0)}$, the values of u_z deflection increase significantly, and from a specific value, they change abruptly (Figure 3). This indicates that the system in the singular position rapidly loses stiffness.

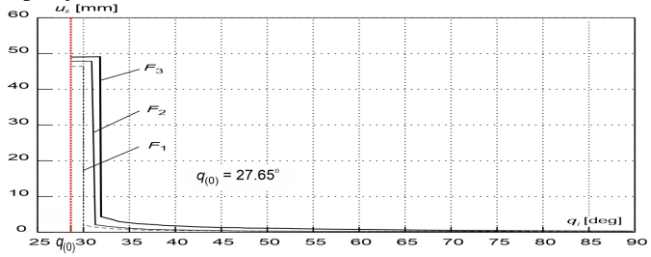

Fig. 3. Deflections of u_z center of the platform under load $\boldsymbol{F}_i$ as a function of rotation angle q_i

Measurements have shown that it can also be dangerous for the mechanism's links to approach the singular configuration. A system loaded with a higher force enters the singular position sooner. The entry point into the singularity can be read from the diagrams of the deflection of u_z at the points of abrupt changes in the waveforms.

2 Final Remarks

The obtained experimental results of the manipulator indicate that it is impossible to obtain influence on holding the set position of the links in the singular configuration. Hence, when planning working trajectories, it is necessary not only not to bring the system into the singularity, but also to maintain an appropriate "safe distance" from singular configurations. The results of the experiments and measurements confirm the theoretical conditions for the categorical prohibition of introducing of parallel manipulators into singular configurations from the task of direct kinematics. This conditions the development of such drive control algorithms to prevent the execution of trajectories leading to singular positions.

References

1. Bałchanowski J.: Topology and analysis of the singularities of a parallel mechanism with three degrees of freedom. Archives of Civil and Mechanical Engineering. vol. 14, 80–87, (2014).
2. Bałchanowski J.: Spatial parallel mechanisms. Analysis and Synthesis. Publishing House of Wrocław University of Science and Technology, Wrocław, Poland (in Polish), (2016).
3. Bałchanowski J., Szrek J., Wudarczyk J.: Analysis of constraint equations of the parallel mechanisms with 3 DoF in singular configurations. Proceedings of the 15th IFToMM World Congress on Mechanism and Machine Science, Springer, 607-616, (2019).
4. Gosselin C., J. Angeles J., Singularity analysis of closed-loop kinematic chains, IEEE Trans. Robot. Automat., vol. 6, 281–290, (1990).
5. J.-P. Merlet J. -P: Parallel Robots. Springer Dordrecht, ISBN 978-1-4020-4132-7, (2006).

Design of Underwater Robot system for collecting Floating debris

Sangheon Roh[1[0009-0009-6136-5760]] , Donghwi Shin[1[0009-0005-5121-947X]], Jeonghyeon Lee[2[0009-0000-2758-6273]], Taegyun Kim[#1[0000-0002-7655-1883]] and Sungkeun Lee[#2[0000-0002-5393-2560]]

[1] Yeungnam University, Gyeonsan-si, Republic of Korea
[2] Keimyung University, dalseo-gu, Republic of Korea
[#1] Yeungnam University, Gyeonsan-si, Republic of Korea
tgkim@yu.ac.kr
[#2] Keimyung University, dalseo-gu, Republic of Korea
skyoo@kmu.ac.kr

Abstract. This paper presents a system design for an underwater robot capable of collecting floating debris on the water's surface using pumps and a vortex generator. An experimental environment was established, and a series of experiments were conducted to confirm the performance of the vortex generator with varying parameters, including pump pressure, vortex generator angle, motor control for vortex generation, and the vortex inlet shape. The optimal design criterion for the underwater robot was the power consumption during operation and the speed of the floating object induced by the generated vortex, measured using vision-based methods. An experiment was conducted to determine the optimal design value of the underwater robot system. Data to establish the relationship between various design criteria and vortex performance were obtained through various experiments. In this process, the suction mechanism of the vortex generator was optimized. The proposed system provides an effective solution for collecting floating debris on the water's surface.

Keywords: Underwater robot, Vortex generator, Floating debris, computer vision

1 Introduction

The environmental impact is increasing due to the rise in floating waste in rivers and seas. To mitigate environmental problems, it is necessary to reduce the amount of floating waste. However, floating debris often exists in various environments and locations that are difficult for humans to access. As the vortex generated in the water has the property of collecting floating matter in the center, it can effectively collect floating waste over a large area proportional to the size of the vortex. This paper introduces an underwater robot that utilizes a vortex to collect floating waste around it.

2 Hardware Design

2.1 Overall Structure of underwater robot and testbench

Fig. 1(a) shows a load cell that measures the change in buoyancy, and a motor for the rotation mechanism that measures the input power. The flow sensor measures the pump discharge flow rate, and the discharge pump measures the pump input power. Fig. 1(b) shows a vision system for obtaining the speed of floating matter in the vortex. Fig. 1(c) shows the structure of the vortex generator, which includes a flow dispersion device that helps maintain the shape of the vortex.

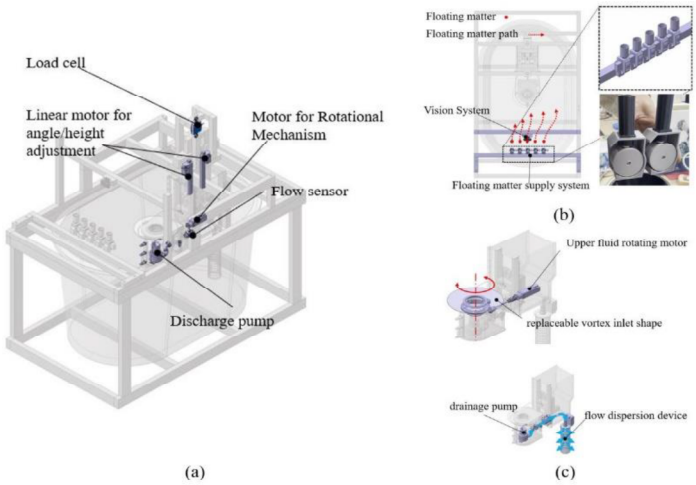

Fig. 1. (a) Various sensors. (b) Vision system. (c) Vortex generator.

References

1. Suaria, G., & Aliani, S. (2014). Floating debris in the Mediterranean Sea. *Marine pollution bulletin*, *86*(1-2), 494-504.
2. Xie, Q., Wang, T., Yao, S., Zhu, Z., Tan, N., & Zhu, S. (2020). Design and modeling of a hydraulic soft actuator with three degrees of freedom. *Smart Materials and Structures*, *29*(12), 125017.
3. Youngtak Kim, ″Function,″ Computational Thinking and Python Programing, 1th ed, HONGREUNG, PUBLISHING COMPANY, Korea(2022)

Acknowledgement

This research was supported by Basic Science Research Program through the National Research Foundation of Korea(NRF) funded by the Ministry of Education(No. NRF-2022R1I1A3072904)

Robust Position Control Through Variable Stiffness and Damping

DongHwi Shin [1][0009-0005-5121-947X], MinNo Lee [1][0009-0002-6493-5617], SangHeon Roh[1][0009-0009-6136-5760] and TaeGyun Kim [#][0000-0002-7655-1883]

[1] Yeungnam Univ, 280, Daehak-ro, Gyeongsan-si, Gyeongsangbuk-do, Republic of Korea
[#] Yeungnam Univ, 280, Daehak-ro, Gyeongsan-si, Gyeongsangbuk-do, Republic of Korea
tgkim@yu.ac.kr

Abstract. This paper presents a 1-degree-of-freedom system with a variable stiffness and variable-damping mechanism utilizing one pair of springs and rubber friction. A wide range of target impedance can be achieved, and the overall system consumes less energy due to the presented mechanism. The dynamic model was defined and validated through simulation and real-world experiments. Results show that the damping coefficient is a function of contact force, contact area, and material, while the stiffness of system, which is nonlinear, depends on each of the three motor angles. To simplify impedance control, the non-linear term was linearized by the Stiffness-Controller that controls the two spring-mounted motors separately to follow a reference spring constant. The ultimate goal of the study is to achieve robust position control using impedance control in a disturbance environment. Overall, the paper presents an approach to designing a system with variable stiffness and damping that could be useful in various adaptive control applications, such as polishing and grinding robots.

Keywords: Variable stiffness, Variable damping, Impedance control, Robust-position control.

1 Introduction

In the manufacturing process, polishing is a kind of finishing process to obtain even surface condition. In generally, most of the surface subject to polishing has high stiffness and same for the machine. Improper contact force can damage both the surface and the machine in this condition. For a good surface condition (low surface roughness), it is important to finely follow reference force in terms of force control. Also Reducing external influence like vibration should be considered. Therefore, we propose a system with adjustable impedance not only virtually but also mechanically.

2 Design of Hardware

The presented system uses four motors. Two for variable stiffness, rest of them used for variable damping and main rotor respectively. One pair of springs are connected

between main rotor and each of two motors. For damping, rubber pad is mounted in front of loadcell and this part can move up and down to make friction on main rotor. This hardware can change its stiffness and damping roughly but for more precision, impedance control in main rotor should control rest of it.

3 Dynamic Analysis

There are three controllers below. Each controller is responsible for generate corresponding torque such as damping, stiffness and impedance torque to main rotor.

$$\sum M_o = J_m\ddot{\theta} = \text{Damping CONT}(D_m) + \text{Stiffness CONT}(K_m) + Impedance\ \text{CONT}(J_c, D_c, K_c) \quad (1)$$

$$J_m\ddot{\theta} = -K_m\theta - D_m\dot{\theta} + (J_c\ddot{\theta} + D_c\dot{\theta} + K_c\theta) \quad (2)$$

$$(J_m - J_c)\ddot{\theta} + (D_m - D_c)\dot{\theta} + (K_m - K_c)\theta = 0 \quad (3)$$

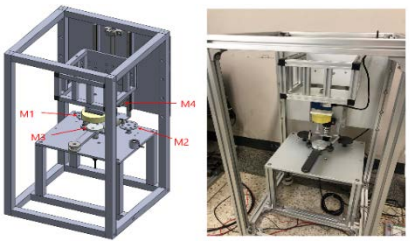

Fig. 1. 1-degree-of-freedom system for Robust position control.

References

1. Laffranchi, M., Tsagarakis, N. G., & Caldwell, D. G. (2010, May). A variable physical damping actuator (VPDA) for compliant robotic joints. In *2010 IEEE International Conference on Robotics and Automation* (pp. 1668-1674). IEEE.
2. Sarakoglou, I., Tsagarakis, N. G., & Caldwell, D. G. (2014, May). Development of a hybrid actuator with controllable mechanical damping. In *2014 IEEE International Conference on Robotics and Automation (ICRA)* (pp. 1078-1083). IEEE.
3. Radulescu, A., Howard, M., Braun, D. J., & Vijayakumar, S. (2012, July). Exploiting variable physical damping in rapid movement tasks. In *2012 IEEE/ASME International Conference on Advanced Intelligent Mechatronics (AIM)* (pp. 141-148). IEEE.

Acknowledgement

This research was supported by Basic Science Research Program through the National Research Foundation of Korea(NRF) funded by the Ministry of Education(No. NRF-2021R1I1A3059727)

Unfolded Paper Manipulation by a Robot Hand Using High-speed Image Processing

Hideto Okura[1], Shunsuke Komizunai[2], Taku Senoo[1], and Atsushi Konno[1]

[1] Graduate school of Information Science and Technology, Hokkaido University, Sapporo, Japan,
{okura@scc,senoo@ssi,konno@ssi}.ist.hokudai.ac.jp,
[2] Faculty of Engineering and Design, Kagawa University, Takamatsu, Japan

1 Introduction

Nowadays, handling paper is an essential part of everyday life and is required in various situations. Since paper is a flexible material, its stiffness changes irregularly when folded. Therefore, precise handling requires bending without creases. Examples of such tasks include handling and transferring paper, as well as packaging work. Although the several studies on paper grasping have been reported [1], [2], its manipulation was static and slow. Causes of difficulties in manipulating flexible objects include deformation of the flexible object during manipulation and estimating the amount of deformation of the flexible object. The goal of this study is to solve the difficulty of flexible object manipulation by combining a multi-finger robotic hand with visual information from high-speed vision, and to manipulate paper as if it were a human hand. By dynamically manipulating paper, it performs the task of changing paper from a gravitationally bent state to a taut state with a small number of degrees of freedom and at high speed.

2 Proposed Method

Paper has the property of having stiffness in the direction perpendicular to the direction of bending. A smooth curved surface that can be created simply by bending a sheet of paper without incising or creasing it is called a flexible surface, and has the property that at any given point, a straight line passing through that point exists on the curved surface. In other words, the shape of paper can be manipulated by applying a bending force in a direction perpendicular to the desired bending direction.

In this study, a high-speed vision system is used to detect paper deformations in real time. Due to the nature of perspective projection, the contours of the paper captured by the camera are distorted in the direction of the curved surface. This distortion is calculated by cubic spline interpolation of four markers placed at equal intervals on each side of the paper. The curvature of the resulting curves is calculated to provide feedback on how much the paper is bent. The markers are tracked using a self-windowing method that takes advantage of the properties of high-speed vision. This process achieved a high processing speed of 300 Hz.

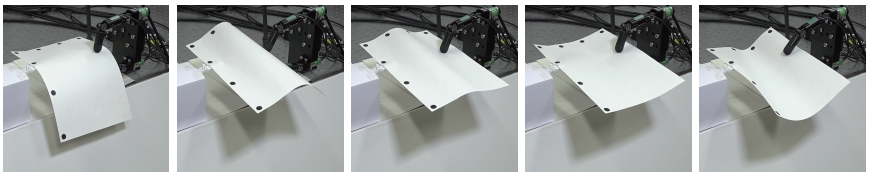

Fig. 1: Manipulation of the paper shapes using both hands

Fig. 2: Manipulation of the paper shapes using one hand

3 Result

Figure 1 shows how the paper shape is manipulated by applying force from both sides. Since only one hand was available for this study, the paper shape was manipulated by fixing one side of the hand to reproduce a two-handed grasp. Figure 2 shows a piece of paper being grasped by a robot hand. The paper can be manipulated dynamically and at high speed by deforming the shape of the paper surface using the inertia caused by the downward swing of the hand. By devising manipulation operations and applying image processing to detect the shape of the paper surface even during high-speed movements, the appropriate timing for switching operations could be obtained. As a result, the paper surface can be manipulated and constrained quickly and with minimal movement.

4 Conclusion

This paper proposes a handling strategy that can impart stiffness in any direction by exploiting the physical properties of paper. By optimizing the procedure of manipulating paper using this strategy, it became possible to perform dynamic bending operations of paper without making creases. In the future, efforts will be made to achieve more complex movements by increasing degrees of freedom using a robot arm.

References

1. K, Hoya., et al.: On Grasping a Sheet of Paper by Multi-Fingered Hand, SICE Tohoku Chapter, Vol. 293(2015), No. 7. (in Japanese)
2. C, Elbrechter., et al.: Bi-Manual Robotic Paper Manipulation Based on Real-Time Maker Tracking and Physical Modelling. In: IEEE/RSJ International Conference on Intelligent Robots and Systems, pp. 1427–1432. (2001).

Tactile determination of the instantaneous screw axis of a human knee surrogate by a force-controlled robot using a Krylov method

Alexander Hoffmann, Patrick Jendro, and Andrés Kecskeméthy

Universität Duisburg-Essen, Duisburg, Germany,
alexander.hoffmann-lmr@uni-due.de,
WWW home page: https://www.uni-due.de/mechanikb/

Knowledge about human joint axis location and orientation is required for rehabilitation robotics and surgical planning procedures. An approach based on a tactile force-controlled robot is developed in [1], to which this paper presents a follow-up stemming from a project to determine the instantaneous screw axis (ISA) of a human knee (Fig. 1). A surrogate with a revolute joint (Fig. 2) is utilized for intermediate testing [2], while the traction boot requires no further adaptations for future experiments. A force/moment sensor is mounted at the end-effector of the robot, which is coupled to the set-up to guide its movement.

Fig. 1. Project vision

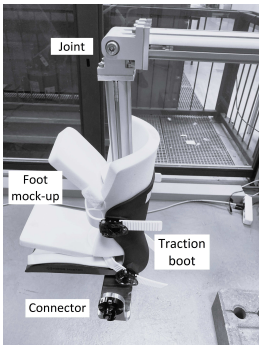

Fig. 2. Test set-up

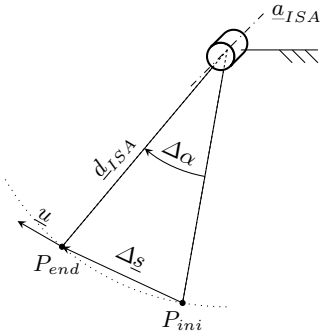

Fig. 3. Inital and final pose

For ISA determination, the initial and final pose of an incremental movement in direction of least resistance $\underline{u}$ are analyzed (Fig. 3). A power iteration method [1] is applied to iteratively determine the eigenvector of the greatest eigenvalue of the compliance matrix, which corresponds to the sought direction $\underline{u}$. Then the ISA orientation is derived from the end-effector rotation from initial to final pose expressed by rotation axis $\underline{a}_{ISA}$ and angle $\Delta\alpha$. The ISA position $\underline{d}_{ISA}$ is determined by analyzing the isosceles triangle spanned in time by the step distance $\Delta\underline{s}$ and $\underline{d}_{ISA}$ at the initial and final end-effector pose. The robots movement is controlled by a fully parallel force and torque admittance controller according to [3] combined with two low-pass filters LP (Fig. 4). In order to avoid the force and moment control working against each other, a coupling of the two was pre-installed in the force/moment control such that the desired moment at the expected ISA due to the orthogonal force component is subtracted from the sen-

sor moment. In this way, the control predicts an estimate of the correct rotation about the current ISA, denoted as C_{ISA}. In the control scheme, the admittance controller determines the desired position and orientation of the end-effector, which are transformed by inverse kinematics for the inner position control loop of the manipulator realized in joint space. The measured force $\underline{F}_m$ and moment $\underline{\tau}_m$ are fed back to the admittance controller. The control law with force difference $\Delta\underline{F} = \underline{F}_d - \underline{F}_m$ and moment difference $\Delta\underline{\tau} = \underline{\tau}_d - \underline{\tau}_m$ as inputs is

$$\begin{bmatrix} \Delta\underline{F} \\ \Delta\underline{\tau} \end{bmatrix} = \begin{bmatrix} M_T \\ M_R \end{bmatrix} \begin{bmatrix} \ddot{\underline{r}} \\ \dot{\underline{\omega}} \end{bmatrix} + \begin{bmatrix} D_T \\ D_R \end{bmatrix} \begin{bmatrix} \dot{\underline{r}} \\ \underline{\omega} \end{bmatrix} \tag{1}$$

where $\underline{r}$ and $\underline{\omega}$ denote the position and angular velocity increments respectively. The diagonal positive 3×3 matrices M and D represent virtual translational (T) and rotational (R) mass and damping matrix respectively. Experimentally a trajectory guidance with mean deviations of 1.0073 mm and four checkpoints lead to an orientation error of 2.8057° and a positioning error of 0.6997 mm on average in identifying the ISA (Fig. 5). Future research will focus on validating the proposed algorithm with artificial knees and human limbs as project objectives.

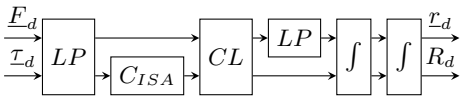

Fig. 4. Admittance control scheme

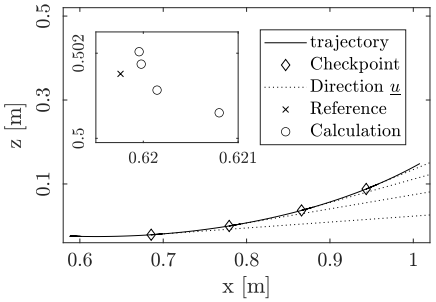

Fig. 5. Resulting trajectory

Public funding acknowledgment

This research was partially funded by the German Federal Ministry of Education and Research under support code 16SV8516. The authors thank Battenberg Robotic GmbH & Co. KG for cooperation in experiment design and execution.

References

1. Liu, H., Kecskeméthy, A., Nguyen, D.H., Parzer, H., Gattringer, H.: Determination of an unknown unactuated joint axis in a compliant serial kinematical chain using force control and the Krylov power iteration method. Mechanism and Machine Theory. 2017. vol. 117. pp. 198-209.
2. Lohse, N.: Entwicklung eines Beinmodells mit anschließender Messung und Analyse von mechanischen Kenngrößen bei der robotergestützten Kniegelenkanalyse (unpublished master's thesis). Justus-Liebig-Universität Giessen. 2021.
3. Siciliano, B., Villani, L.: Robot Force Control. Kluwer Academic Publishers. 1999.

Design of a hybrid suspended cable and thruster driven parallel robot using hexarotor

Yifan Feng[1], Yusuke Sugahara[1], Ming Jiang[1], Marco Ceccarelli[2,3], and Yukio Takeda[1]

[1] Tokyo Institute of Technology, Tokyo, Japan
{ho.i.aa, sugahara.y.ab, jiang.m.ad, takeda.y.aa}@m.titech.ac.jp,
[2] International Research Frontiers Initiative, School of Engineering, Tokyo Institute of Technology, Tokyo, Japan
[3] University of Rome Tor Vergata, Rome, Italy
marco.ceccarelli@uniroma2.it

Cable-driven parallel robots (CDPRs) have been studied for decades for the capability of high speed and acceleration motion over a wide workspace with low inertia. However, due to the characteristic that cable can only pull but not push, at least $n+1$ cables are required to fully control the n degrees-of-freedom (DOF) of the end-effector(EE). The set of feasible EE poses can be collectively referred to as the wrench-feasible workspace (WFW) [1]. Adding extra cables can expand the WFW, but it decreases the interference-free workspace (IFW), especially when there are collisions between the cables under the EE and obstacles on the ground. Cable-suspended parallel robots (CSPRs) do not have cables below, but the cable tension depends on the gravitational force acting on the EE. A lightweight EE reduces the WFW, while a heavy one compromises acceleration and safety.

Recent developments in unmanned aerial vehicles (UAVs) have inspired the use of thrusters in CDPRs. Thrusters can offer greater flexibility for generating additional wrenches that can be freely attached on EE. Furthermore, the addition of thrusters has minimal impact on IFW. In [2], co-axial counter-rotating propellers as thrusters are utilized to generate unidirectional forces and counteract the effects of gyroscopic moments, and the arrangement of thrusters on the EE to generate a desired wrench set within a specified workspace.

CDPRs have potential advantages for use in indoor collaborative robotics with the function of such as picking, placing, and transporting items that require a specific orientation. If it is intended to be used in a confined room with limited overall structure space, the maximum distance between the winches connecting one end of the cable is restricted. Therefore the propellers as thrusters can be applied to enhance the WFW and IFW, and considering the effects of directions, connection positions, maximum thrust of propellers, a fully actuated hexarotor is employed, as shown in Figure 1, which is able to decouple position and attitude control. The fully actuated hexarotor fixed on the EE that is reversal facing downward is proposed, which is shown in Figure 2. Three cables connect winches and EE, generating three-dimensional forces, but there is no downward component. The hexarotor generates three-dimensional torques that are used to control the attitude of the EE, as well as three-dimensional forces.

The vertical downward force is applied to maintain tension in the cables, while the horizontal force is used to further expand the WFW.

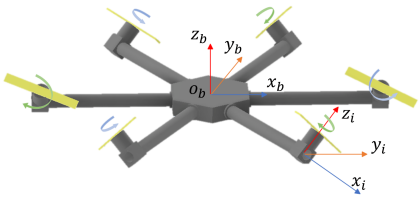

Fig. 1. Schematic diagram of fully actuated hexarotor with double-tilted rotors

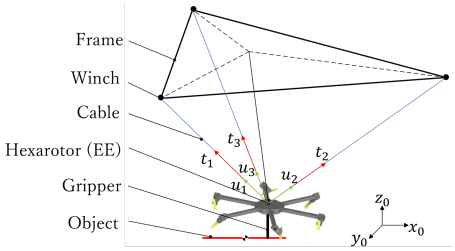

Fig. 2. Schematic diagram of CSPR with fully actuated hexarotor

Hyperplane Shifting Method proposed in [3] is used to calculate the WFW. Since the hexarotor independently controls the attitude of the EE, only the 3 DOF translational motion is considered in this calculation. WFW is indicated by the colored dots in Figures 3, and can be significantly expanded by increasing the thrust in a single downward direction. Figure 4 demonstrates that the WFW can be further expanded by employing the hexarotor arrangement and distributing a total force of 90 N to each of the six propellers.

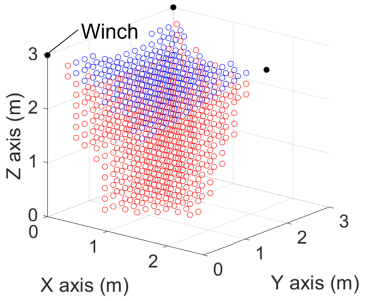

Fig. 3. CSPR with unidirectional downward 30 N & 90 N thrust and the WFW are 2 m^3 (Blue) & 6.22 m^3 (Blue and Red)

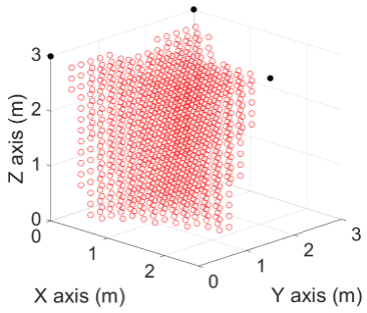

Fig. 4. CSPR with hexarotor and the WFW is 7.98 m^3

References

1. Abbasnejad, G., Eden, J., & Lau, D. (2018). Generalized ray-based lattice generation and graph representation of wrench-closure workspace for arbitrary cable-driven robots. IEEE Transactions on Robotics, 35(1), 147-161.
2. Sun, Y., Guo, Y., Song, C., & Lau, D. (2022). Wrench-feasible workspace-based design of hybrid thruster and cable driven parallel robots. Mechanism and Machine Theory, 172, 104758.
3. Bouchard, S., Ement, C., Gosselin, C., & Moore, B. (2010). On the ability of a cable-driven robot to generate a prescribed set of wrenches. Journal of Mechanisms and Robotics, 2, 1-9.

Machine Learning Aided Self-Calibration Schemes for Parallel Kinematic Manipulators

Yu-Jen Chiu[1*], Wei-Hsuan Lin[2], Cheng-Kuo Sung[2] and Syanala Jaya Prakash Reddy[1]

[1] Ming Chi University of Technology, New Taipei City 243303, Taiwan R.O.C.
[2] National Tsing Hua University, Hsinchu 300044, Taiwan R.O.C.
yjchiu@mail.mcut.edu.tw

1 Introduction

Self-calibration or autonomous calibration methods have been well-known for compensating kinematic errors in the robotics areas for the recent decades. The methods require no expensive metrology equipment and avoid the measurement procedures that are time consuming, inconvenient, and difficult to obtain accurate results. Indeed, there inevitably exist certain limitations, such as the issues of redundant parameters, observability of the selected postures, the complexity of the error models [1]. Self-calibration schemes have been approved to be feasible and effective due to their benefits. The conventional calibration is based on the analytical error models, thus is generally dealing with the geometrical error sources. Researchers have been devoting themselves into the investigation of the machine learning algorithms for calibrating non-geometrical errors. Nonetheless, massive measurement by individual equipment is essential for training a machine learning model. The present work is aimed at the possibilities that a self-calibration approach incorporates machine learning algorithms to enhance the positioning accuracy of a parallel kinematic manipulator (PKM).

2 Methods

A translational 3-UPU configured PKM with variable-length links is considered as an illustrative example. Each of the three links of the PKM is dismantled into two universal joints A_i, B_i and one extensible link L_i (i = 1, 2, 3). In addition to the encoders on the driving motors to control the lengths of the links, there are additional 6 redundant sensors installed on each passive joint A_i and B_i (Fig. 1). The objective of the conventional calibration method is to identify the parameters in the kinematic error model. Theoretically, only one redundant sensor is capable of fulfilling self-calibration purposes. In the neural network (NN) methods, the compensation values of the actuating variables are pursued alternatively [2]. In this work, the position errors of all joints and the detected offsets of all sensors are considered. The compensation values of the link lengths δL_i and the angular deviation of the redundant sensor readings $\delta\theta_i$ and $\delta\phi_i$ are introduced. For each real posture, various estimated postures $\mathbf{X}_j$ can be obtained according to different kinematic chains j and the sensor readings $L_i + \delta L_i$, $\theta_i + \delta\theta_i$ and $\phi_i + \delta\phi_i$ within the PKM. The genetic algorithm is adopted for searching the best fit of δL_i, $\delta\theta_i$ and $\delta\phi_i$ such that the estimated posture errors from different kinematic chains are minimized. Based on a number of postures, the combinations of $\mathbf{X}_j$ (input) and $L_i + \delta L_i$ (output) are achieved to serve as the basis for NN training. The resultant NN function therefore provides the actuated variables for the desired postures.

3 Results and Discussion

For the self-calibration schemes based on the kinematic error models, 17 kinematic parameters are identified by adopting 6 redundant sensors and 3 positions for data acquisition. The translational and angular errors for joint locations and sensor readings are within the range of ± 1 mm and $\pm 0.5°$, respectively. Figure 2(a) reveals the resultant trajectories of a circular path are accurately improved. The root mean squares error is significantly reduced from 2.16 mm to 2.63×10^{-5} mm in the simulation. As for the neural network approach, another 100 positions of the end-effector are randomly generated within the feasible workspace. The translational and angular errors for joint locations and sensor readings are introduced within the range of ± 0.2 mm and $\pm 0.5°$, respectively. The neural network aided self-calibration scheme reduces root mean squares error of the positioning accuracy from 1.450 (un-calibrated) to 1.321 mm. The error reduction rate in Fig. 2(b) shows an obvious tendency to enhance the positioning accuracy (below the red line), nonetheless, some tests become worse in the illustrative example. It reveals certain limitation worthy of further investigations.

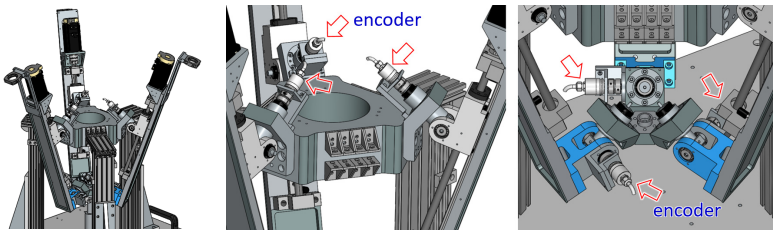

Fig. 1. A 3-UPU type PKM and the installation of redundant sensors.

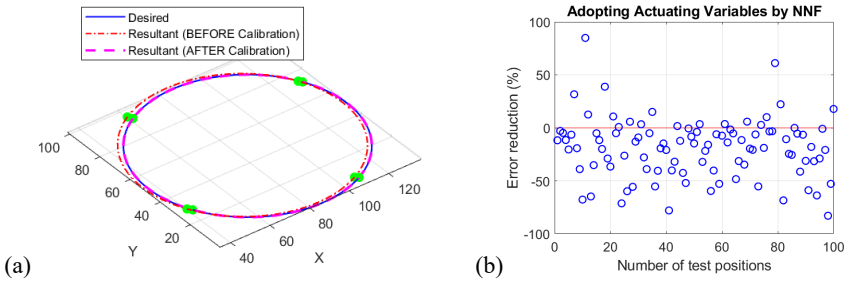

Fig. 2. The improvement in the positioning accuracy: (a)the self-calibration schemes based on kinematic error models; (b)the effectiveness of the neural network aided self-calibration scheme.

Acknowledgement

This work was financially supported by the National Science and Technology Council, Taiwan, R.O.C. (NSTC 111-2221-E-007-068-MY2 and NSTC 112-2637-E-131-005).

References

1. Chiu, Y. J. and Perng, M. H.: Self-calibration of a general hexapod manipulator with enhanced precision in 5-DOF motions. Mechanism and Machine Theory 39(1), 1–23 (2004).
2. Zhong, X., Lewis J. and N-Nagy F. L.: Inverse robot calibration using artificial neural networks. Engineering Applications of Artificial Intelligence (9), 83–93 (1996).

Foldable base plate mechanism for parallel link robots

Daigo Tokunaga[1][0009-0009-4191-7521], Satoshi Nishikawa[1][0000-0003-0905-8615] and Kazuo Kiguchi[1][0000-0003-4408-0420]

[1] Kyushu University, Fukuoka, 819–0395, Japan
kiguchi@ieee.org

1 Introduction

Robotic limbs have been studied in a great number of configurations, some mimicking living organisms and others specialized to perform a desired function [1]. Parallel link manipulators are used to develop robotic limbs that exhibit high rigidity [2][3]. However, most parallel link mechanisms have actuators located near the base plate, and the base plate also becomes larger when the actuator size increases according to the required output characteristics. Some robots use a wide base plate to ensure that the actuators have a range of motion without interfering with each other. When robots are applied to support human behavior in living environments, it is desirable for the robots to change their size to be suitable for the desired workload and space. Therefore, a parallel link robot that can change the size of its base plate, which is the largest part of the parallel link robot, is proposed.

2 Foldable base plate mechanism

The robotic limb shown in Fig. 1(a) is taken as an example of the parallel link robot in which the proposed foldable base plate mechanism is applied. The robotic limb can change the characteristics of the end-effector's output and range of motion by manipulating the force point and pivot point of the lever mechanism with two 3-spherical-prismatic-revolute parallel manipulators [4]. Fig. 1(b)(c)(d) shows a 3D model of the proposed foldable base plate mechanism. Each actuator mounting point is connected to the circle plate via vertical links, horizontal link and hexagonal plates. Vertical links are driven by a ball screw in the center, and actuator mounting points move linearly from the center. The hexagonal plate rotates around the central circle plate to which the ball screw is attached. The Pitch Circle Diameter (PCD) of the actuator mounting position in Fig. 1 is 360 mm in the open position and 190 mm in the closed position, reproducing the PCD of the existing base plate. The range of PCD is determined by the length of the link arm and the link ratio. In the closed position, the end-effector can only move vertically with respect to the base. The base can be continuously expanded, and as the distance of expansion increases, the range of motion of the robotic limb increases as well as the rigidity against moments applied to the end-effector (Fig.2).

*This work was supported by JST [Moonshot R&D][Grant Number JPMJMS2034].

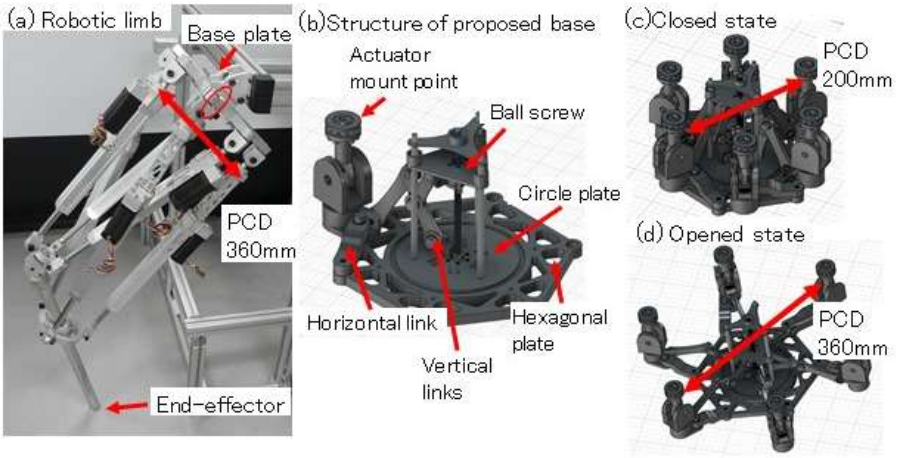

Fig. 1. The robotic limb and the proposed base structure. (a) The robotic limb using an adjustable lever mechanism with double parallel link platforms. (b) The mechanism of one actuator. (c)(d) The mechanism changes continuously from state (c) to state (d).

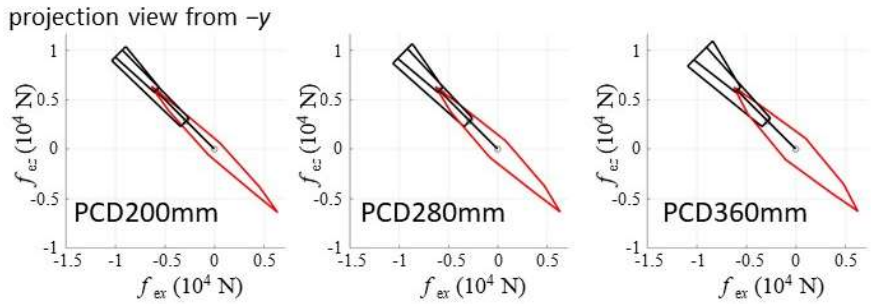

Fig. 2. Maximum output force profiles at the end-effector when actuator mounting PCD is 200, 280, and 360mm. The thrust of each actuator in this simulation is 1500 N.

References

1. X. Zhou and S. Bi, “A survey of bio-inspired compliant legged robot designs,” Bioinspiration & biomimetics, vol. 7, no. 4, p. 041001 (2012).
2. P. Yang and F. Gao, “Leg kinematic analysis and prototype experiments of walking-operating multifunctional hexapod robot,” Proceedings of the Institution of Mechanical Engineers, Part C: Journal of Mechanical Engineering Science, vol. 228, no. 12, pp. 2217–2232 (2014).
3. M. Morisawa, T. Yakoh, T. Murakami, and K. Ohnishi, “A comparison study between parallel and serial linked structures in biped robot system,” in 26th Annual Conference of the IEEE Industrial Electronics Society (IECON), vol. 4, pp. 2614–2619. (2000).
4. S. Nishikawa, D. Tokunaga and K. Kiguchi, "Adjustable Lever Mechanism with Double Parallel Link Platforms for Robotic Limbs," IEEE/RSJ International Conference on Intelligent Robots and Systems (IROS), Kyoto, Japan, pp. 1950-1956 (2022).

Vibration isolation in spacecraft using Gough-Stewart Platform

Yogesh Pratap Singh[1[0000−0001−6582−6004]] and Ashitava Ghosal[1[0000−0002−8308−7724]]

[1] Indian Institute of Science, Bangalore 560012, India
{yogeshsingh,asitava}@iisc.ac.in

1 Introduction

In spacecraft, micro-vibrations (up to 300 Hertz) induced due to the presence of reaction wheels, momentum wheels, and cryocoolers, reduces the pointing accuracy of sensitive payloads mounted on it. A 6 degree of freedom Gough-Stewart platform (GSP) is effective for isolating payloads from these micro-vibrations. It is known that a conventional Gough- Stewart platform fails to give dynamic isotropy where the first six vibration modes have the same or nearly the same natural frequency. The primary reasons to use dynamically isotropic GSP are a) it is easy to tune dampers for passive vibration attenuation for the given frequency bandwidth, and b) a multi-input-multi-output system system can be treated as six decoupled single-input-multi-output systems (for six degrees of freedom), which simplifies active control.

A **two radii or Modified Gough-Stewart Platform (MGSP)** is proposed to achieve dynamic isotropy. An MGSP is a parallel manipulator with a movable top platform, a fixed base, and struts with a linear actuator in between them. It differs from the traditional GSP with the anchoring points/spherical joints are on two radii on each platform instead of on one radius in a traditional GSP, as shown in Fig. 1(a). In an MGSP, these struts are divided into two sets having a rotational symmetry for their attachment points along the circumference with an equal angular spacing of 120°.

2 Design of MGSP

The unknowns (design parameters) for an MGSP are the inner and outer radii of the bottom and top platforms, R_{bi}, R_{ti}, R_{bo}, R_{to} the angular separation of the connection points in the top and bottom platform (inner and outer), $\alpha_{to}, (\alpha_{bi} - \alpha_{ti})$, the leg length ratio a, and the height of the top platform H from the bottom platform (see Fig. 1a). The force transformation matrix ($[\mathbf{B}]$), together with a novel *geometry-based approach*, is used to obtain closed-form analytical solutions in their explicit form for dynamic isotropy in a 6-6 MGSP at its neutral position. For dynamic isotropy, the six eigenvalues of the natural frequency matrix $[\mathbf{G}]$ [1] must be equal.

$$[\mathbf{G}] = [\mathbf{M}]^{-1}[\mathbf{K_T}] = [\mathbf{M}]^{-1}k[\mathbf{B}][\boldsymbol{B}]^T \quad (1)$$

where $[\mathbf{M}]$ is the mass matrix of the payload, $[\mathbf{K_T}]$ is the stiffness matrix in the task

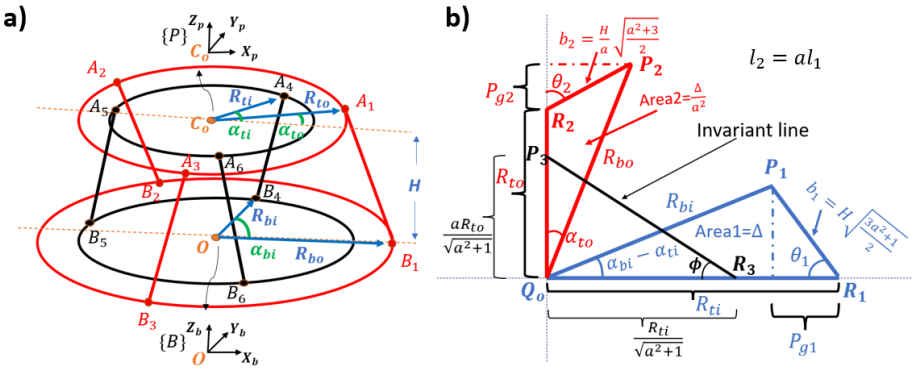

Fig. 1. a) MGSP, **b)** Geometrical interpretation of MGSPs' design variables [1]

space, and *k* is the axial stiffness of each strut. The obtained set of transcendental equations from equal eigenvalue conditions lead to several geometrical observations from where closed-form solutions to the design variables were developed [1] – a 3-D dynamically isotropic MGSP design problem could be simplified into sets of triangles in 2-D space related by certain geometrical relationships (refer to Fig. 1(b)) that can be used to find the design variables.

3 Validation via simulation and experiments

A prototype based on flexural joints (refer to Fig. 2) was developed for experimentation (to avoid friction and backlash in the spherical joints), and various flexural joints were explored before arriving at the final design. All six natural frequencies obtained analytically from Section 2 match well with simulation results -- validating our design. We were able to capture the first six modes experimentally lying in a narrow frequency bandwidth around 29 Hertz, which were very close to analytical and simulation results. The platform is designed for approximately 10.5 Kg payload including the mobile platform and can isolate micro vibration above 41 Hertz.

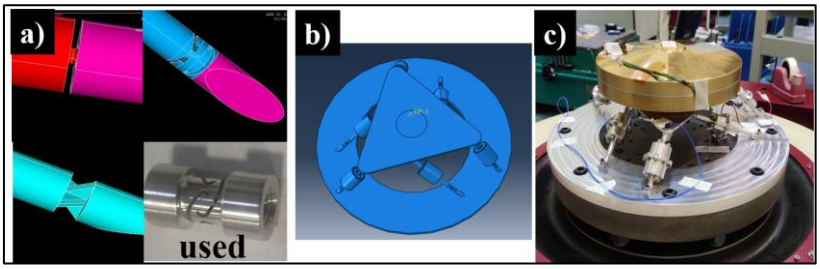

Fig. 2. a) Various flexural joints explored, **b)** CAD model, **c)** Experiment prototype of MGSP

References

1. Singh, Y.P., Ghosal, A.: Dynamically isotropic Gough-Stewart platform design using a pair of triangles. In: Proc. of 32nd International Conference on Robotics in Alpe-Adria-Danube Region, Springer Nature, Bled, Slovenia (2023, Accepted).

Motion Design for Robotic Contact: Insertion Tasks

Siamak Arbatani[1] and József Kövecses[1] Marek Teichmann[2]

[1] Department of Mechanical Engineering and Centre for Intelligent Machines, McGill University, Montréal, QC H3A 0C3, Canada,
siamak.arbatani@mcgill.ca; jozsef.kovecses@mcgill.ca
[2] CM Labs Simulations, Montréal, QC H3C 1T2, Canada
marek@cm-labs.com

Motion planning and trajectory tracking control for general unconstrained motion of robotic arms is quite well-established and possible to achieve in different ways. On the other hand, motion while the robotic arm is in contact with static or dynamic objects is a much more complex problem to deal with.

In this work, we specifically study insertion tasks where a given motion of the end effector is required but with the presence of contact. Such physical interactions can occur in both grasping and insertion and represent significant challenges in various areas of robotic mechanical systems. Robotic motion tasks with insertion can be challenging for conventional feedback control that is designed for free space trajectory tracking, and it may have to be augmented with force feedback based control. A small misalignment between the insertion tool and socket can lead to unwanted phenomena such as jamming during an insertion maneuver as a result of emerging contact forces.

Various approaches have been developed for motion planning and controlling robotic systems which involve contact tasks. Established control methods with compliant manipulators and mating parts require sophisticated and task specific designs as well as accurate models embedded in the control system along with manually tuned feedback controllers to achieve acceptable performance.

Reinforcement Learning (RL) has shown strong potential in some challenging applications. In RL based methods, human insight and intuition are replaced by autonomous learning techniques to achieve optimal control policy from exploring and exploiting the learning environment. Deep RL is successfully used in learning of robotic navigation and manipulation skills [1]. Robotic contact tasks are also examined with RL based methods in various studies. Sparse rewards are common in robotic manipulation applications. Reward shaping is quite challenging to guide the learning agent in these applications. Use of demonstrations to tackle the sparse reward problem is first proposed in [2], and simulation based demonstrations and the use of reverse curriculum in robotic contact tasks have also been explored. Training of a Deep RL agent has also been examined directly on a real robotic insertion setup [3]. In the training environment, they consider outputs of a force/torque sensor and rounded position values of the peg as their observation space and desired force components and orientation angles of the peg as their discrete action space. They have defined the reward function based on distance between the peg and target for the search phase and downward dis-

placement for the insertion phase. They have demonstrated high success rate in all cases with maximum initial position and angle errors of 1 mm and 1 deg.

The majority of published work about RL-based robotic contact tasks use reward functions based on notions of distance, vision and output from force/torque sensors. Distance and vision would not provide any insight about the forces resulted from contacts. The information solely from force/torque sensors would not characterize the motion in presence of contact forces. Therefore, in presence of contact forces, feedback from a combination of sources are typically employed.

In this work, we investigate robotic contact maneuvers related to insertion problems using a novel method that requires minimum information and employs a physically motivated reward function. We propose and develop a framework using reinforcement learning, specifically employing residual policy learning (RPL), to tackle the problem.

The proposed approach augments the parametric robotic models, in our case an inverse kinematic model, with a learned element. This captures the part that cannot be described by parametric models, but it also takes advantage of the information already contained in the parametric model. In the core of this framework lies a reward function that is designed based on physical considerations, and captures the important phenomena in insertion in a physically meaningful way. The use and implementation of this reward function requires a minimum level of information and instrumentation from the robotic system.

This work can be used in different applications. In this paper, we demonstrate it in the context of simulation and human-computer interaction. The other possible application is in physical robotic contact manipulation.

Our demonstration of the framework includes a virtual robotic contact testbed and human-computer interaction. The results obtained illustrate the effectiveness of the proposed approach. Sensitivity and uncertainty in contact friction and in misalignment due to the insertion angle are analyzed and incorporated. The parameters representing these are randomized during the learning step in order to generalize the solution.

Three different training scenarios are investigated. It is found that the wider range of insertion angle and randomized friction coefficient during the training leads to more intuitive motion behaviour from the residual policy. Results present 100% success with the residual policy for both the prescribed motion and human controlled cases.

References

1. Kahn, G., Villaflor, A., Ding, B., Abbeel, P. & Levine, S. Self-supervised deep reinforcement learning with generalized computation graphs for robot navigation. *2018 IEEE International Conference On Robotics And Automation (ICRA)*. pp. 5129-5136 (2018)
2. Hester, T., Vecerik, M., Pietquin, O., Lanctot, M., Schaul, T., Piot, B., Horgan, D., Quan, J., Sendonaris, A., Osband, I. & Others Deep q-learning from demonstrations. *Proceedings Of The AAAI Conference On Artificial Intelligence*. **32** (2018)
3. Inoue, T., De Magistris, G., Munawar, A., Yokoya, T. & Tachibana, R. Deep reinforcement learning for high precision assembly tasks. *2017 IEEE/RSJ International Conference On Intelligent Robots And Systems (IROS)*. pp. 819-825 (2017)

Optimal inverse kinematics solution for redundant manipulators combined with trajectory scaling

Łukasz Woliński[1[0000-0001-9617-4117]] and Marek Wojtyra[1[0000-0001-7225-7647]]

[1] Warsaw University of Technology, IAAM, Nowowiejska Str. 24, 00-665 Warsaw, Poland
Marek.Wojtyra@pw.edu.pl

1 Introduction

A kinematically redundant structure increases the dexterity of the robotic manipulator and offers an ability to avoid obstacles and handle singularities. Therefore, redundant robots are well-suited for work in human-centered, cluttered environments. However, planning of the joint trajectory that satisfies the desired end effector trajectory and does not exceed the capabilities of the robot joints is not a trivial task. This article presents a novel algorithm—based on the quadratic programming (QP) approach—that allows for traversing the prescribed task-space path while satisfying joint-space constraints.

2 Algorithm overview

The Predictive Quadratic Programming Inverse Kinematics with Scaling (PQPIK-S) solves the optimal trajectory planning task by combining the inverse kinematics (IK) problem with trajectory scaling and solving them simultaneously. The proposed method is inspired by [1] and emerges from our earlier work [2]. The core of the PQPIK-S is the quadratic programming (QP) problem:

$$min_{\dot{\boldsymbol{q}},\dot{\lambda}} \frac{1}{2}\gamma_0\left(1-\dot{\lambda}\right)^2 + \frac{1}{2}(\dot{\boldsymbol{q}}-\dot{\boldsymbol{\varphi}})^T\boldsymbol{W}(\dot{\boldsymbol{q}}-\dot{\boldsymbol{\varphi}})$$

$$\text{w.r.t. } \boldsymbol{J}\dot{\boldsymbol{q}} = \boldsymbol{v}\dot{\lambda},\ \dot{\boldsymbol{q}}_{min} \le \dot{\boldsymbol{q}} \le \dot{\boldsymbol{q}}_{max},\ 0 \le \dot{\lambda} \le 1$$

Joint coordinates are gathered in vector $\boldsymbol{q}$. The vector $\dot{\boldsymbol{\varphi}}$ defines an additional task for a redundant robot (such as obstacle avoidance), whereas parameters γ_0 and $\boldsymbol{W}$ are used to assign weights to different tasks. The end effector velocity $\boldsymbol{v} = \boldsymbol{v}\dot{\lambda}$ is parameterized in terms of virtual time λ, allowing to slow down the desired motion if (and only if) the joint constraints cannot be satisfied in any other way. Note that the equality constraints rather than the cost functional guarantee that the desired task-space path is traversed. It should also be stated that the equations are discretized at the acceleration level.

Moreover, the QP problem is formulated in such a way that it utilizes the prediction of the manipulator's future joint states, allowing the scaling to begin sufficiently early. Outside the prediction horizon, the desired trajectory does not have to be known, allowing for replanning when working in dynamic environments. The obtained joint trajectory is optimal: inside the prediction horizon, it satisfies the end effector trajectory (the main task), fulfills in the best way the secondary tasks (e.g., obstacle avoidance), and maintains the least possible scaling, all with regard to the joint constraints.

The PQPIK-S plays the role of the *joint trajectory planner* block shown in Fig. 1 (left). It was implemented in C++ with the use of the *Eigen* library for linear algebra and *qpOASES* containing the active-set solver for the QP problem.

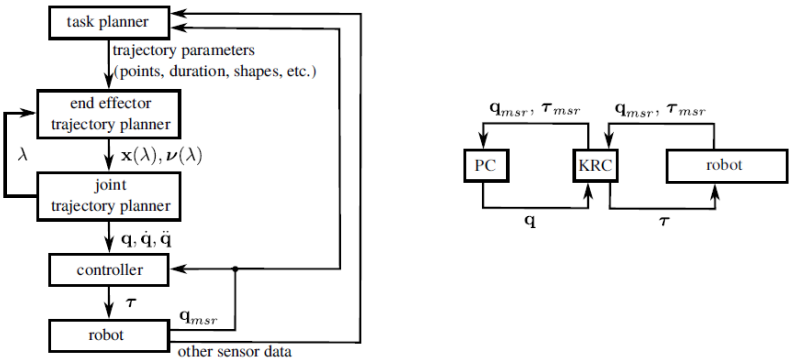

Fig. 1. PQPIK-S flow-chart (left) and overview of control system arrangement (right).

3 Simulations and hardware experiments

Comprehensive simulation studies prove the PQPIK-S's advantages compared to the classic IK methods. The most important feature of the PQPIK-S is the ability to satisfy the joint constraints, slowing down the end effector motion only when needed. Moreover, the PQPIK-S computations are done within a 10-millisecond cycle, allowing for a real-time operation.

The experiments performed on KUKA LWR 4+ redundant robot prove the feasibility of the PQPIK-S-generated joint trajectories. The experiments were performed with the use of the Fast Research Interface – KUKA's interface for the communication between the user's PC and KUKA Robot Controller (KRC)—see Fig 1 (right).

4 Conclusions

A novel method developed in this work proved to be capable of fulfilling the constraints while traversing the desired path with minimum possible velocity adjustments.

Acknowledgments. This research was partially supported by the National Science Centre, Poland grant no. 2022/45/B/ST8/00661.

References

1. Flacco F., De Luca A., Khatib O.: Control of redundant robots under hard joint constraints: Saturation in the null space, IEEE Trans. Robot. 31(3), 637–654 (2015).
2. Woliński Ł., Wojtyra M.: A Novel QP-Based Kinematic Redundancy Resolution Method With Joint Constraints Satisfaction, IEEE Access, 41023-41037, vol. 10 (2022).

Experimental Estimation of Bending of a Cylinder-Piston Actuator of a Parallel Platform by Relative Optical Marker Tracking

Christian Brans[1] and Andrés Kecskeméthy[1]

University of Duisburg-Essen, Chair of Mechanics and Robotics, Lotharstr. 1, 47058 Duisburg, Germany
[christian.brans, andres.kecskemethy]@uni-due.de,
https://uni-due.de/lmr

In the setting of parallel platforms, tracking of bending of actuator legs is problematic as due to construction restrictions the placement of strain gauges is difficult and optical markers are impossible to be placed in an absolute coordinate system whithin the precision needed to track bending ($\sim 5\mu$m). In this work, a method is described to track bending out of relative optical measurements with respect to a bended start position. Fig. 1 shows the parallel architecture tool machine under investigation, the new R(2RPS-RP)-UPS parallel platform named 'TriMule' developed by Prof. Tian Huang in his laboratory in Tianjin [1]. Four optical markers by Leica Absolute Tracker AT901-LR (0.32μm accuracy) were placed along the horizontal of the RPS limb, which was extended in five 50mm steps $y_0 ... y_5$. The position of the markers were measured relative to a world reference system aligned with the base coordinate system of the parallel platform. To avoid errors caused by noise, the experiment was repeated seven times. For the reproduction of the bending, a Bernoulli beam model of the limb as an overlap of the cylinder and the piston was implemented in Matlab using Heaviside functions for the discontinuous changes and an ODE integrator over the length. In the area of overlap, the bending stiffness and the masses were superposed. Moment of inertia of the piston $I_{y,p}$ and the cylinder $I_{y,c}$, Young modulus E and density ρ were fitted by numerical optimization such that the bending deflections obtained from the optical tracking for each optical marker matched in a least square error sense the corresponding displacements of the model. Joint clearance could be neglected as there was no reverse loading. The model and the detailed computations are omitted here due to lack of space

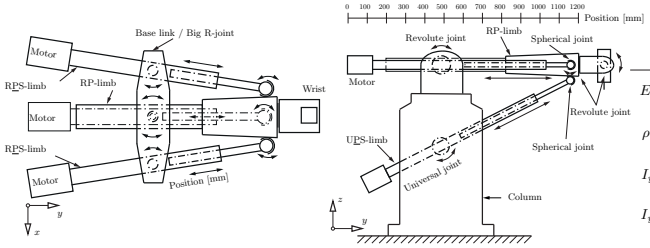

	exp.	fit.
E 10^5[N/mm^3]	2.10	2.27
ρ 10^{-6} [kg/mm^3]	7.75	7.99
$I_{y,p}$ 10^4 [mm^4]	3.92	4.54
$I_{y,c}$ 10^5 [mm^4]	2.38	2.79

Fig. 1: Top and side view sketch of parallel platform and fitted parameters

and will be presented at the conference. The calculated bending lines for every y_i (Fig. 2 b)) are compared with the values of the measurements, showing good agreement for the first three strokes. For the two larger strokes, the measurement points seem to deflect less than the model. Also, the fitted moments of inertia are unrealistically large (Fig. 1, right table). This may be due to the sagging of the end effector at longer strokes by 1μm, which seems plausible. The experiment shows that a relative model-based optical beam deflection sensor may render sufficient accuracy if effects of sagging of the end-effector are identified and compensated. Further investigation will foresee an overconstrained guidance of pistons, sagging, and more involved material and cross-section parameters.

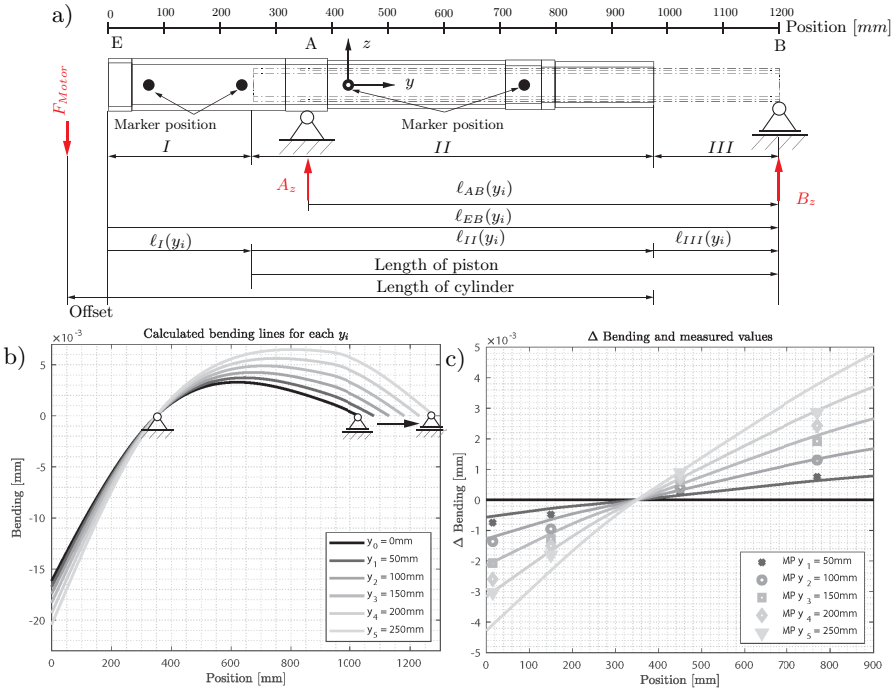

Fig. 2: a) Beam model of the RPS limb in an arbitrary position, b) calculated bending lines, c) Δ bending and measured values

Acknowledgments

This work was supported by EU H2020-MSCA-RISE 2016 (Grant 734272). The authors wish to particularly thank Prof. Huang Tian and Prof. Liu Haitao from Tianjin University for their support in their laboratory for the experiment.

References

1. Tian Huang, Chenglin Dong, Haitao Liu, Tao Sun, and Derek G. Chetwynd. A simple and visually orientated approach for type synthesis of overconstrained 1T2R parallel mechanisms. *Robotica*, 37(7):1161–1173, 2019.

Efficient walking of the quadruped using passive linear spring

Pramod Pal[1], Shishir Kolathaya[1] and Ashitava Ghosal[1]

Indian Institute of Science, Bangalore, India[1]
pramodpal@iisc.ac.in

1 Introduction

Quadruped robots have garnered considerable interest due to their potential in various applications. The design components of a quadruped, such as link design, actuation and control systems, compliant foot and sensors, play a crucial role in achieving efficient and stable locomotion. An essential component of attaining efficient walking in quadrupeds is the design of compliant feet that allow the quadruped to absorb impact forces and store and release energy with each step. In earlier work, we developed a design of a leg for a quadruped with a linear passive spring in the foot. Through a combination of rigid body simulations and experiments, we were able to demonstrate that the range of values of the spring constant at the leg resulted in the highest hopping height, outperforming legs equipped with spring systems with either higher or lower stiffness[1]. These results highlight the significance of selecting the optimal linear spring configuration for efficient locomotion in quadrupeds. In this work, we extend the idea of a linear spring in the legs to all the legs of a quadruped and perform simulations in MuJoCo – a multi-body simulation platform where contact/impact of the leg with the ground, the kinematics and dynamics of the legs, torso and other links of a quadruped can be modeled and taken in to account for simulations[2]. One of the key preliminary result is that the designed (and modeled) quadruped can traverse a longer distance when there is a linear spring in the foot as compared to a quadruped where the legs are "rigid" with no springs.

2 Simulation results

As mentioned earlier, we have now designed a quadruped with each leg containing a linear spring. The trajectory traced by a foot of the quadruped is shown in Fig. 2a and it can be seen that the trajectories are similar (bit not exactly the same) with and without a spring in the leg. The quadruped is made to undergo a trotting gait – front and hind legs on opposite sides move together. Simulations are done for about 10000 time-steps and the forward motion of the quadruped is shown in Fig. 2b. It can be clearly seen that quadruped traverses (on flat ground) more distance when there is spring in the leg – about 3.5 m versus about 2 m when there is no spring.

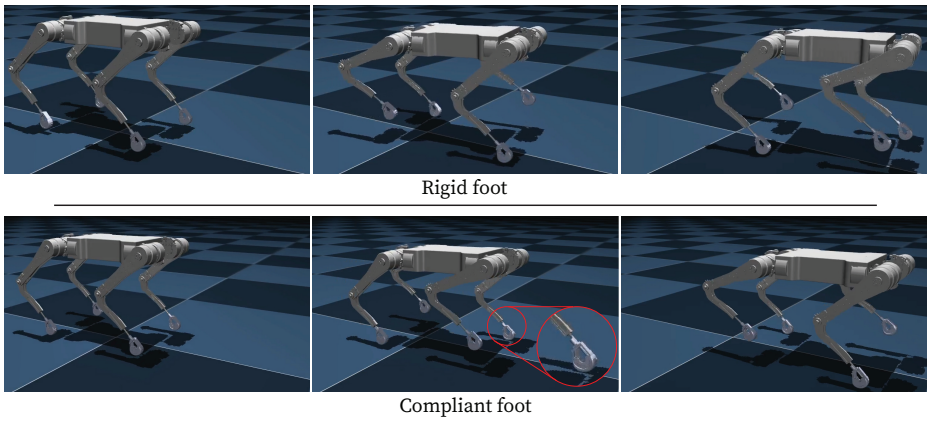

Fig. 1. Snapshot of motion of quadruped

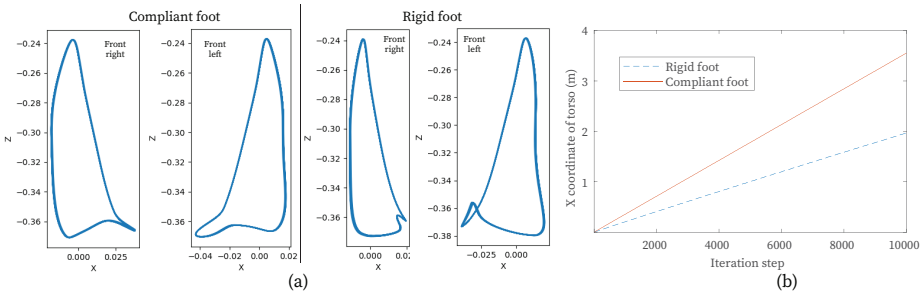

Fig. 2. (a)Trajectory of the foot (b)Distance traveled by quadruped

3 Conclusion

This work deals with the simulation of a quadruped with and without a spring(compliance) in the leg. Preliminary results show that the quadruped with compliance can travel a longer distance as compared to a quadruped with a rigid foot. The work is continuing and will be validated with hardware results in the future.

References

1. Pramod Pal, Anubhab Dasgupta, Avinash Bhashkar, Shishir Kolathaya, and Ashitava Ghosal,Efficient Robot Hopping Mechanisms with Compliance using Evolutionary Methods.In: Proc of 32nd International Conference on Robotics in Alpe-Adria-Danube Region, Springer Nature, Bled, Slovenia (2023, Accepted)
2. Todorov E, Erez T, Tassa Y. Mujoco: A physics engine for model-based control. In2012 IEEE/RSJ international conference on intelligent robots and systems 2012 Oct 7 (pp. 5026-5033). IEEE.

Kinematics of a Tripod Parallel Continuum Robot

O. Altuzarra[1], V. Petuya[1], M. Acevedo[2], M. Vizcaíno[2], and S. Rodríguez[2]

[1] University of the Basque Country UPV/EHU, Torres Quevedo s/n, Bilbao 48012, Spain,
victor.petuya@ehu.es
[2] Universidad Panamericana. Facultad de Ingeniería. Álvaro del Portillo 49, Zapopan, Jalisco, 45010, México

A Tripod $3\underline{P}RS$ is a lower mobility parallel manipulator with 3 degrees of freedom whose usual geometrical constraints enforce a 2 rotational and 1 translational type of motion. Nevertheless, some parasitic motions occur on the constrained degrees of freedom accounted for by a set of algebraic constraint equations. Parallel Continuum Manipulators are devices where some elements are replaced by slender rods whose deformation is the source of mobility, allowing the elimination of some of kinematic joints. This type of closed-loop compliant mechanisms have some features that can be useful in certain applications, i.e. the deformed state introduces a preload that avoids backslash, and their inherent compliance can be useful in delicate tasks. In this contribution, the kinematic analysis of a tripod-type parallel continuum manipulator, $3P\underline{F}S$ shown in Fig. 1, is performed; then Workspace and singularity locus are obtained, and positioning accuracy is evaluated experimentally.

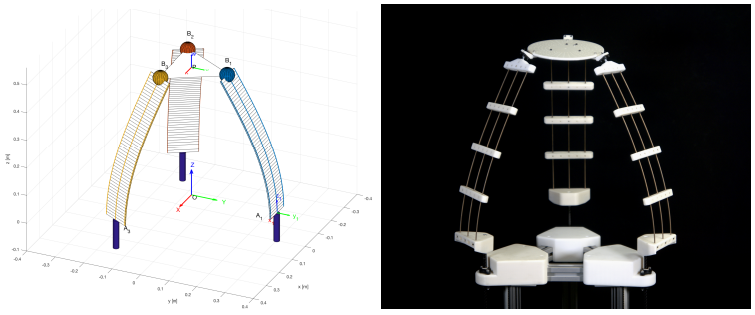

Fig. 1. Flexible Tripod $3\underline{P}FS$ with Cosserat Rods

The $3\underline{P}FS$ Tripod is a coupled mechanism of flexible rods, where a rigid end-effector is connected to 3 rods A_iB_i, in which the proximal ends of each rod are clamped to a vertical linear actuator such that $\mathbf{a}_i = \mathbf{p}_i(0) = [a_{xi}\ a_{yi}\ \rho_i]$. At each configuration, under given load, rods will be deformed $\mathbf{p}_i(s)$ so that the system is in a stable equilibrium pose.

The *FK* consists of determining the pose of the end-effector, i.e $\mathbf{p}_{\mathcal{P}}$ and the quaternion $\tilde{\mathbf{e}}$, when input values for each rod ρ_i and a load are imposed [1]. Guess values are required to start a boundary value problem on a vector of 25 geometric and static equilibrium residuals. A Newton method is used in the shooting method and requires the evaluation of a Jacobian of the residue vector function with respect to the variables of the problem. After each iteration, guess values are updated and the process starts again until residuals are below a given tolerance. In Lower Mobility Parallel Mechanisms, dependent output variables are defined with a constraint analysis. However, this is no longer possible in flexible systems as such *hard* geometric constraints cannot be imposed. Output components are obtained with no distinction on whether they are *principal* (controlled) or *parasitic*. However, for the *IK* it is essential to asses appropriately which components are *principal* and *parasitic*. We will show that some translational and rotational ellipsoids can be found to do this. Then, only some output components are imposed in the *IK* while the *parasitic* ones are unknowns of the problem. Once these Kinematic problems are solved, a workspace analysis can be performed.

For the prototypes, an actuators' platform was designed with 3 linear guides controlled by stepper motors. The electronic control includes a GUI with a MATLAB application that communicates through a serial port with a microcontroller, allowing the control of the manipulator using direct and inverse kinematic solutions.

For measuring the output coordinates of a manipulator, 6D pose estimation is used [2]. This computer vision technology provides high-precision estimates of position and orientation by solving a PnP problem, where the ArUco markers are matched with their 2D projections in the image. Another approach for validating the accuracy of artificial vision measurements is through the use of an accelerometer. In this study, the MMA8451Q three-axis accelerometer sensor with a 14-bit resolution will be employed. This analysis aids in the determination of an object's orientation using a straightforward trigonometry algorithm.

Acknowledgments

The authors thank the financial support received from the Spanish Government (Project PID2020-116176GB-I00) financed by MCIN/AEI/10.13039/501100011033 and the support through Project IT1480-22 provided the Regional Basque Government.

References

1. Black, C.B.; Till, J. and Rucker, D.C.: Parallel Continuum Robots: Modeling, Analysis, and Actuation-Based Force Sensing. IEEE Transactions on Robotics. 34, 29-47 (2018) 10.1109/TRO.2017.2753829
2. Wu, G. and Shi, G.: Experimental statics calibration of a multi-constraint parallel continuum robot. Mechanism and Machine Theory. 136, 72-85 (2019) https://doi.org/10.1016/j.mechmachtheory.2019.02.013

A Novel Integrated Driving and Steering Module and Its Multi-objective Optimization

Xinbo Chen[1], Jiawei Chen[1] and Wei Wang[2]

[1] Tongji University, Shanghai 201804, China
[2] Tokyo University of Agriculture and Technology, Tokyo 184-8588, Japan

1 Introduction

The integrated driving and steering module allows the vehicle to independently control the steering angle and driving torque of each wheel. This enables the vehicle to realize various driving modes such as oblique driving and lateral driving, which improve the vehicle's maneuverability and operating stability. However, the suspension system of existing integrated driving and steering modules is typically a sliding pillar type suspension, which makes balancing the mass and structural stiffness of suspension system a challenge. For the modules based on wishbone arm type suspension and trailing arm type suspension, due to the installation of additional steering motor in the suspension, the unsprung mass will also increase, affecting the contact characteristics of the wheels. In order to solve the problem of large unsprung mass in the integrated driving and steering module, this paper proposes a new type of integrated driving and steering module based on a lasso mechanism, and multi-objective optimization is conducted.

2 Structure Introduction

The new integrated driving and steering module proposed is shown in Fig. 1.

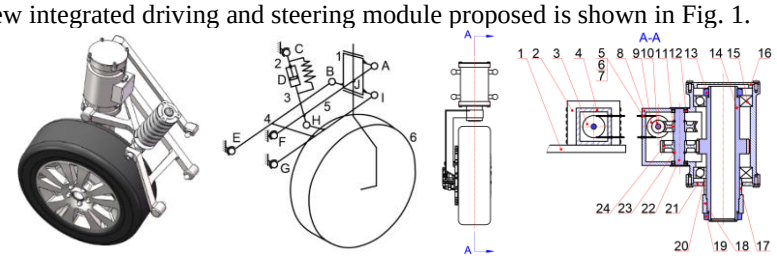

a) b)

Fig. 1. The noval integrated driving and steering module. a) Schematic diagram of suspension structure. b) Schematic diagram of transmission mechanism.

This module adopts a double trailing arm type suspension. The steering motor is installed on the frame, which is different from the existing modules. The steering motor becomes a part of the sprung mass. Due to the variation of the center distance between the output shaft of the steering motor and the input shaft of the steering mechanism with

the height of the wheel jump, this module transmits steering force through a flexible compound lasso mechanism. The steering mechanism contains a worm gearing, whose self-locking characteristics help lock the steering angle. This module has the advantages of 0 kingpin offset, good structural stiffness (especially the longitudinal stiffness), and low unsprung mass.

3 Multi-objective Optimization

The optimization design of suspension system typically includes optimization of wheel alignment parameters, lightweight design of suspension components, and optimization of the K&C characteristics. As there is a coupling relationship between the kinematics, statics and dynamics of the suspension, the traditional serial optimization method requires multiple rounds of iterative calculation. In order to improve the optimization efficiency, this paper established a multi-objective collaborative optimization model of the suspension. The optimization problem is solved by using Isight software and the sequential quadratic programming algorithm.
The established collaborative optimization model is shown as follows:

$$\begin{cases} \min F(X_g) = \lambda_1 K + \lambda_2 S + \lambda_3 D \\ s.t. \sum (X_g - X_g^*)^2 \leq \varepsilon \end{cases} \tag{1}$$

In the equation, K is the optimization model for wheel alignment parameters, and each wheel alignment parameter is derived from the pose change formula based on the RRSS mechanism; S is the lightweight design model for the trailing arms, and the maximum stress value of the arms is calculated by the trained radial basis neural network model; D is the optimization model for vehicle body vibration, and the root mean square value of the vertical acceleration of the vehicle body is also calculated by the trained radial basis function neural network model.
Compared to the serial optimization results, the wheel alignment parameters after multi-objective optimization have been optimized with ranges of 45.02% to 87.28%. Only the longitudinal slip of the wheel center has increased by 17.99%. The mass of the upper trailing arm has decreased by 8.81%. The mass of the lower trailing arm has decreased by 8.18%. The root mean square value of the vertical acceleration of the vehicle body has decreased by 11.43%.

4 Conclusion

Through configuration innovation design and multi-objective optimization, the novel integrated driving and steering module proposed in this paper has a small unsprung mass. The multi-objective optimization method adopted helps to improve the effectiveness and efficiency of suspension optimization. This paper can provide reference for the design and optimization of integrated driving and steering modules in the future.

Investigation of Tribological Properties of Carbon Coatings Deposited on Polymer Substrate

Youn-Hoo Hwang, YouJin Min and Dae-Eun Kim

Yonsei University, Seoul, South Korea
kimde@yonsei.ac.kr

Keywords: Polymer, friction, wear, DLC (Diamond-like Carbon) coating

1 Introduction

Polymer materials have outstanding properties such as light weight, self-lubricating ability, chemical stability, and moderate wear resistance. Due to these attractive properties, polymers are used in a variety of mechanical parts such as gear, bearing and seal. However, polymers have relatively low strength and poor wear resistance, which can lead to early failure of machine parts [1]. In order to minimize these problems and improve the durability of the polymer, research on fabricating composite materials with various nanomaterials and polymers is being actively conducted. In this regard, methods to improve the tribological properties of polymers by depositing protective coatings need to be further explored.

Diamond-like carbon (DLC) has emerged as a useful coating material due to its unique combination of mechanical, chemical and thermal properties [2]. DLC has a low coefficient of friction and high wear resistance, so it can be used to improve the durability of precision parts. In this study, in order to reduce the wear, DLC coating was applied to the surface of the polymer, and the frictional properties of the polymer were investigated in various environments.

2 Method

2.1 Tribological test and analysis

A polytetrafluoroethylene (PTFE) that is widely used in the industry was selected for the experiments. The DLC coating was deposited on PTFE using a sputtering technique. The experiments were performed using a reciprocating type of tribometer in environment chamber. The experiment was conducted three times per specimen at each condition to ensure reliability. After the test, the wear tracks were measured using a laser confocal microscope and scanning electron microscope (SEM). The chemical compositions of the wear tracks were measured by energy dispersive X-ray spectroscopy (EDS) and Raman spectroscopy.

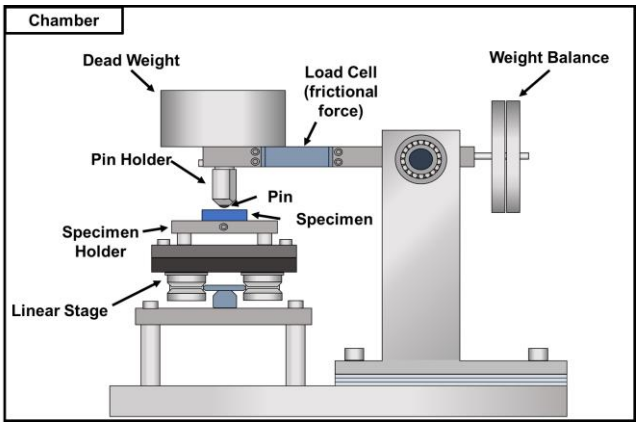

Fig. 1. Schematic of reciprocating type tribometer in the environment chamber

3 Results and conclusions

Comparing the average coefficient of friction between the DLC coated PTFE and the pure PTFE, the DLC coated PTFE had a relatively high friction coefficient. As for the wear behavior, it was found that in general the wear rate was higher in the case of the pure PTFE compared to DLC coated PTFE.

The tribological properties of PTFE and DLC coated PTFE were examined in vacuum environment as well. It was found that one of the important factors causing the difference in the wear rate of the specimens in a vacuum environment was that the surface coating inhibited the adhesive wear of pure PTFE during sliding motion. These results show that DLC coatings can be effectively used to improve the tribological properties of polymers used in various environments.

4 Acknowledgement

This research was financially supported by the Ministry of Trade, Industry and Energy (MOTIE) and Korea Institute for Advancement of Technology (KIAT) through the International Cooperative R&D program (Project ID: P0019808)

References

1. Lin, L. Y., Kim, D. -E.: Tribological properties of polymer/silica composite coatings for microsystems applications. Tribology International. 44(12), 1926-1931 (2011).
2. Liu, Y., Zhang, K., Han, J. -H., Hwang, Y. -H., Xu, S., Kim, D. -E.: One-step method to enhance biotribological properties and biocompatibility of DLC coating by ion beam irradiation. Friction. 10(7), 1114-11126 (2022).

Profile optimization in roller bearings for pressure uniformity

Macareno, L.[1[0000-0003-2225-9032]] Aguirrebeitia, J.[1[0000-0002-0709-9432]]
Heras, I.[1[0000-0002-1320-7823]] Eizmendi, M.[1[0009-0006-8415-9634]]

[1] Department of Mechanical Engineering, Faculty of Engineering in Bilbao.
University of the Basque Country, UPV/EHU, 48013, Bilbao, Spain

1 Introduction

The study of the contact between elastic solids is of great importance in several fields of mechanical engineering [1], mainly in tribology. When all the assumptions of Hertz theory are fulfilled, the relationship among load, deformation, contact area and pressure distribution are well known. However, for many cases in the practical engineering application, these relationships cannot be obtained in an easy way, and the use of numerical methods such as the Finite Element Method or Boundary Element Method [2] is necessary. The latter is the one used in this work. By means of this method, a profile optimization methodology is developed, aiming pressure uniformity in the roller-raceway contact for roller bearings.

2 Development of the method

The BEM was programmed ad-hoc to reach the deformation, contact area and pressure distribution between an arbitrarily defined roller shape and a cylindrical or conical raceway. Then, the optimization procedure was designed to reach uniform pressure distributions. Bearing design is established upon several variables that are determined by the specific application in which they are to be used. From the point of view of the design of the rolling elements, the operational variable is the maximum contact force, while the geometrical variables are the length, the diameter, and the taper angle. Once the raceway is defined, the only geometrical variable that remains the manufacturer's choice is the type of profile to be applied to the roller. In fact, the choice of the profile is the differentiating characteristic between rollers, and a correct choice is of paramount importance if the service life of the bearing is to be maximized. This profile is usually defined by logarithmic functions [3], since they provide a smooth variation of the profile curvature. There are several studies [4] showing methods to optimize these profiles based on various parameters. All these optimizations are limited by the mathematical stiffness of the logarithmic function. This work reaches a solution established upon obtaining the optimum profile using a multipoint method, leaving each point free to move to create the profile with which the distribution of contact pressures is optimal. To achieve this solution, the first step is to define an objective function, which consists of the optimal contact pressure distribution in the mid-contact plane, avoiding pressure

peaks due to abrupt curvature changes. Considering this, the optimum distribution will be rectangular, with a constant pressure that will cancel out in the extreme areas of the roller. The method starts from an initial profile and, in each iteration, the difference of pressures at each point between the obtained distribution and the optimum one is quantified. With these values, a geometric proportional correction is made at each point of the profile. This operation is repeated iteratively until the chosen norm of the pressure difference vector is less than a certain value. The method is highly convergent, and its stability depends on the step size of the proportional adjustment at each iteration. The number of profile definition points also influences the choice of the step size, as well as the execution time.

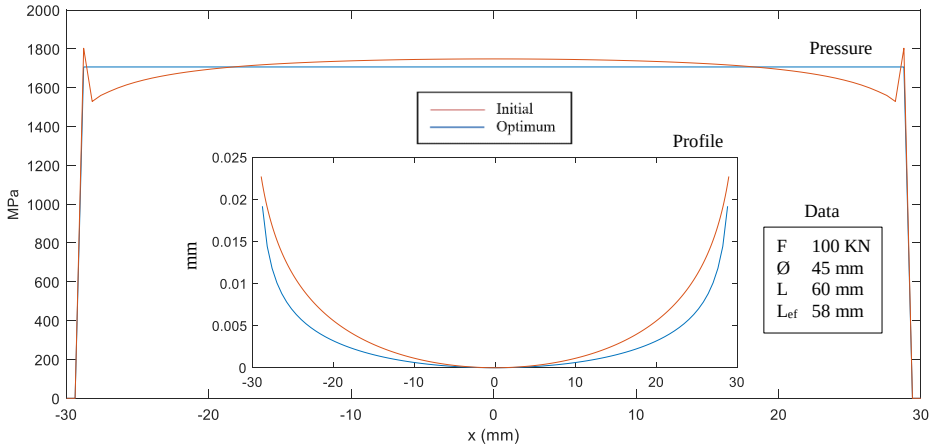

Fig. 1. Contact pressure distribution for initial and optimum profiles.

3 Conclusions

This paper presents an iterative numerical method to obtain the optimum profile of the rollers in a bearing without using any defined mathematical function.

References

1. Johnson, K. L.: Contact Mechanics, Cambridge University Press, Cambridge, UK (1985).
2. Hartnett M. J.: The Analysis of Contact Stresses in Rolling Element Bearings. Journal of Lubrication Technology (101), 105-109 (1979).
3. Lundberg, G.: Elastic Contact Between Two Semiinfinite Bodies. Forschung auf den Gebiete des Ingenieurwesen 10(5), 201-211 (1939).
4. Abhijeet V. Salunkhe et al: A Review on Design Optimization of Rolling Contact Bearings. In: International Journal of Current Engineering and Technology, 7(3) 983-986, Inpressco, (2017)

The effect of graphite domain direction on the friction coefficient of diamond-like carbon measured by polarized Raman analysis

Takayuki Tokoroyama[1], Chiro Fujiwara[1] and Noritsugu Umehara[1]

[1] Nagoya University, Furo-cho, Chikusa-ku, Nagoya, Aichi 464-8603, Japan
takayuki.tokoroyama@mae.nagoya-u.ac.jp

Abstract. We focus on the existence of friction induced graphite domains on the topmost surface of carbonaceous coating. The direction of the incident electric field can be controlled by rotating the polarizer, and clarify the relationship between the direction of friction and the direction of the graphite domain. Two types of thin coatings were prepared. One was tetrahedral amorphous carbon nitride (ta-CNx) coating which slid against a Si_3N_4 ball in vacuum (μ=0.013), and the other was in air under room temperature (μ=0.4). The D peak intensity of low friction surface induced by parallel incident light showed approximately 20 % increase from 0° to 90°. The high friction surface showed approximately 16.8 % increase from 0 to 40°. The result indicated that friction induced graphite domains were possibly existed on the topmost surface. Since the low friction coefficient is considered to occur by incommensurate configuration, so it is assumed that the transfer layer built on counter material will show different direction of the graphite domain due to frictional force.

Keywords: Carbonaceous coating, Graphitization, Polarized Raman.

1 Introduction

The low friction phenomena of carbonaceous coatings are reported its graphitization at the topmost surface by cyclic friction under nitrogen gas [1]. The low friction mechanism of those coatings due to graphitization is divided that low shearing strength graphite sheets were generated at the topmost surface, or graphite domains generated on the topmost surface arranged incommensurate position [2] between transfer layer and its coating. A measurement method capable of detecting the direction of graphite domains formed by friction is interesting. Raman spectroscopy can detect the collective behavior of carbon atom clusters constituting graphite domains [3]. Furthermore, it is assumed that polarized Raman spectroscopy [4], which can control the direction of the incident electric field, can be used to evaluate the direction of graphite domains formed due to friction. In this study, we focus on the existence of such friction induced graphite domains so that we built the direction of the incident electric field can be controlled by rotating the polarizer, and clarify the relationship between the direction of friction and the direction of the graphite domain.

2 Experimental method

A half-wave plate was set among the light source and an optical microscope lends can rotate the polarization of the incident laser beam. The polarizer can rotate 2° of accuracy. The measurement by using the polarizer is divided two types; the incident light polarizer and scattered one is same direction as parallel, and the incident and scattered is perpendicular. Two types of thin coatings were prepared. One was tetrahedral amorphous carbon nitride (ta-CNx) coating which slid against a Si_3N_4 ball in vacuum (5.0×10^{-4} Pa). The other was slid in air under room temperature. The surface prepared in vacuum showed approximately 0.013 of friction coefficient, and the surface of in air showed approximately 0.4. The normal load was 0.19 N, sliding speed was 15.7 mm/s under room temperature.

3 Results and discussion

The polarized Raman analysis for low friction coefficient surface (in vacuum) with 10° from 0° as parallel to the friction direction to 90° was conducted as shown in Fig. 1(a) of D peak intensity, and high friction coefficient surface in air; Fig. 1(b). The D peak intensity induced by parallel incident light showed approximately 20 % increase from 0° to 90°. On the other hand, the high friction surface showed approximately 16.8 % increase from 0 to 40°. The D intensity is related to the graphite edge direction [4], therefore, the result indicated that friction induced graphite domains were possibly existed on the topmost surface as illustrated in Fig. 1(c) and (d). Since the low friction coefficient is considered to occur by incommensurate configuration, so it is assumed that the transfer layer built on counter material will show different direction of the graphite domain due to frictional force.

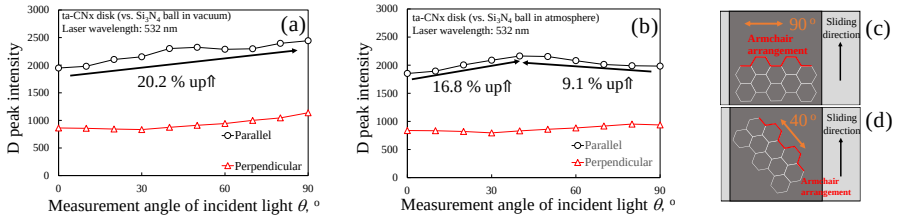

Fig. 1. The D peak intensity as a function of incident light direction (a) low friction in vacuum and (b) high friction in air (c) The D peak intensity as a function of incident light direction of low friction in vacuum and (d) high friction in air.

References

1. H. Inoue, S. Muto, X. Deng, S. Arai and N. Umehara: Thin Solid Films. **616**, 134 (2016).
2. M. Dienwiebel et. al.: Phys. Rev. Lett. 92, 126101 (2004).
3. A.C. Ferrari and J. Robertson: Phys. Rev. B. 61, 14095 (2000).
4. C. Casiraghi et. al.: Nano Lett. 9, 4, 1433 (2009).

The tribological properties of DLC coating with B/Cr co-dopants and clarification of the mechanism at 300ºC

Ruixi Zhang[1], Woo-Young Lee[1,2], Noritsugu Umehara[1], Takayuki Tokoroyama[1], Motoyuki Murashima[1,3], Yuji Takimoto[4]

[1] Department of Micro-nano Mechanical Science and Engineering, Nagoya University, Japan
[2] Intelligent Optical Module Research Center, Korea Photonics Technology Institute, Korea
[3] Department of Mechanical Systems Engineering, Tohoku University, Japan
[4] Toyo Tanso Co.,Ltd., Japan
Corresponding author's E-mail address: ruixi.zhang@mae.nagoya-u.ac.jp

1 Preparation of a-C:B:Cr coating and its mechanical properties

Diamond-like carbon (DLC) coatings, which have widespread applications in many fields due to their low friction, high wear resistance, and other excellent tribological behaviors, have been regarded as a promising candidate of solid lubricants for many years [1]. However, it was found that hard DLC coating became dramatically worn out since 200ºC, thus researchers have been trying to explore new DLC coatings to improve their thermal resistance and tribological properties at high temperature. The current common method is to dope additive elements such as boron, silicon, or certain transition metals into DLC coatings [2]. In recently years, the rapid development of FCVA made it possible to deposit doped-DLC coatings by adding dopant elements into graphite target. However, the optimal deposition of doped-DLC coating and its high-temperature tribological properties have not been clearly studied yet.

In this research, boron and chromium (B/Cr) co-doped DLC coating were prepared by T-shaped FCVA deposition facility. Argon gas with different flow rate was introduced to maintain the deposition continuity, compensating the extinguishment of arc discharge caused by additive elements. Three different graphite targets with various chromium contents (0.5, 1 and 3, at. %) were adopted to deposit different a-C:B:Cr coatings with more than 100 nm thickness. The mechanical properties were evaluated by the nano-indenter (ELIONIX INC.: ENT-1100a), demonstrating that a-C:B:Cr coatings with 10 GPa hardness can be prepared, shown in Fig.1. Besides, the analysis by Raman spectroscopy (JASCO Corporation: NRS-1000) revealed that the additive Cr element improved I_D/I_G ratio of pristine a-C:B:Cr coatings, thus the more "graphite-like a-C:B:Cr coatings" exhibit softer hardness than a-C:B coating,as well as a-C coating.

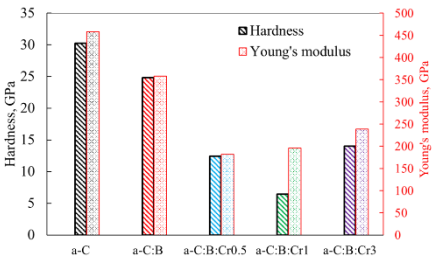

Fig.1. Mechanical properties of a-C:B:Cr coatings with various Cr concentrations

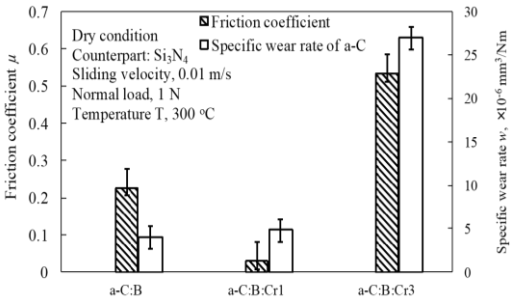

Fig.2. Tribological properties of a-C:B:Cr coatings with various Cr concentrations at 300ºC

2 Tribological properties of a-C:B:Cr coating and its mechanism at 300°C

Three different Cr-containing a-C:B coatings (0, 1, 3 at.%) were used to estimate the tribological properties. Friction experiments were conducted by a pin-on-disk tribometer tester in ambient air with the temperature of 300°C. Si_3N_4 balls were employed to press against the rotating a-C:B:Cr disk (Φ8mm) with a normal load of 1.0 N. Besides, the experiments were carried out at a rotating speed of 200 rpm and sliding radius was 3 mm. Results of tribological properties of each a-C:B:Cr coating were shown in Fig.2, illustrating that a-C:B:Cr_1 coating exhibited ultra-low friction with the average friction coefficient of 0.02, as well as high wear resistance with specific wear rate less than 5×10^{-6} mm^3/Nm. The results also demonstrated that a-C:B:Cr_1 coating was the optimal one among the three various Cr-containing a-C:B coating, Raman analysis on the tribo-film adhered on the Si_3N_4 balls, as shown in Fig.3, proved that graphite-like transfer film was formed on the Si_3N_4 counterpart, where the softest a-C:B:Cr_1 coating might be easiest to realize graphitization and cause low friction. Meantime, the rich C-B bonds in the wear track of a-C:B:Cr coating measured by X-ray Photoelectron Spectroscopy (XPS) was considered as the reason of high wear resistance at high temperature for the a-C:B:Cr_1 coating, since B_4C nanoparticles were proved to be one factor to improve the wear resistance under high temperature.

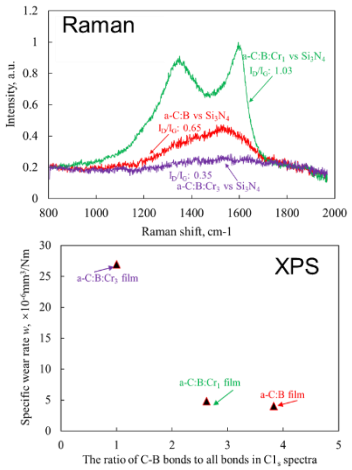

Fig. 3. Surface analysis of Raman spectroscopy on balls and XPS on disks

Conclusion

A DLC coating with co-doped elements is designed for the high temperature, its mechanical and tribological properties are evaluated. The a-C:B:Cr_1 coating is found to realize the low friction and high wear resistance. The graphitization and the formation of B_4C nanoparticles are believed to be the reason of low friction and high wear resistance, respectively.

References

1. Robertson, J., “Diamond-Like Amorphous Carbon,” Material Science and Engineering R, 37, 2002, 129-281.
2. Camargo Jr, S. S., Baia Neto, A. L., Santos, R. A., Freire Jr. A. L., Carius, R. and Finger, F., “Improved High-Temperature Stability of Si Incorporated a-C:H Films,” Diamond Relat. Mater., 7, 8, 1998, 1155-1162.

Effect of Fracture Toughness on Wear of DLC Coatings

Yusei Yamada[1] , Motoyuki Murashima[2] , Noritsugu Umehara[1] ,
Takayuki Tokorfoyama[1] and Woo-Young Lee [3]

[1] Nagoya University, Nagoya, 464-8603, Japan
[2] Tohoku University, Sendai, 980-8579, Japan
[3] Korea Photonics Technology Institute, Gwangju, 61007, South Korea
noritsugu.umehara@mae.nagoya-u.ac.jp

1 Introduction

Diamond-like carbon (DLC) coatings, which are one of amorphous carbon coatings, have many applications due to low friction, high hardness, high wear resistance. Hard materials would have brittleness, so we should avoid the intrinsic fracture of DLC coatings. However it is quite difficult to evaluate the intrinsic fracture properties of DLC coatings and obtain the effect of the fracture properties on wear properties of DLC coatings.
In the present study, we demonstrate a comprehensive study showing a detailed relation between quantitative values of fracture toughness and wear under severe contact conditions. To obtain coatings with various fracture toughness, we prepared a variety of DLC coatings: ta-C:H, a-C:H, and ta-C coatings with different carbonaceous structures and surface roughness. As a result, the present paper clearly illustrates that the wear behavior of DLC coatings can be categorized into two trends; one with fracture and the other without fracture. Finally, we conclude that the wear behavior of the DLC coatings strongly depends on the parameter of K/K_{IC}, which is expressed with a fracture toughness and a stress intensity factor.

2 Experimental

Nine types of DLC coatings were deposited on a silicon substrate: two a-C:H coatings, one ta-C:H coating, and six ta-C coatings. Fracture toughness of these DLC coatings were measured by indentation method. Nastasi et al. demonstrated an improved method to evaluate fracture toughness from the crack length formed on DLC coatings/Si-substrate system [1]. The fracture toughness of the system was measured as a combination between the total fracture work and the composite modulus of the system (including a substrate and a coating). Therefore, a critical fracture toughness of a coating KIC (Eq.(1)) is given by the following Eq.(2)

$$K_{\mathrm{IC}} = \sqrt{G_f E_f} \qquad (1)$$

$$\left[\left(\frac{c_0}{c}\right)^3 - 1\right] = \frac{2d}{\pi c}\left(\frac{G_f}{G_s} - \frac{E_f}{E_s} - 2\right) \qquad (2)$$

Where K_{IC} is the fracture toughness of the coating, G_f is the work of fracture in the coating (fracture energy of the coating), and E_f is the Young's modulus of a coating. In the Eq.(2), c_0 is the half radial crack length in the uncoated substrate, c is the half radial crack length in the coating/substrate system at the same indentation load, d is the coating thickness, G_s is the work of fracture in the substrate (fracture energy of the substrate), and E_s is the Young's modulus of the substrate. Friction test were conducted under dry air condition with a Pin-on-Disk friction tester. Stress intensity factor K was estimated from stress and estimated initial crack length from surface roughness under the friction conditions. Figure 1 shows the relation between specific wear rate and K/K_{IC}. The figure presents a clear trend that the specific wear rate increases with the increase of the K/K_{IC}.

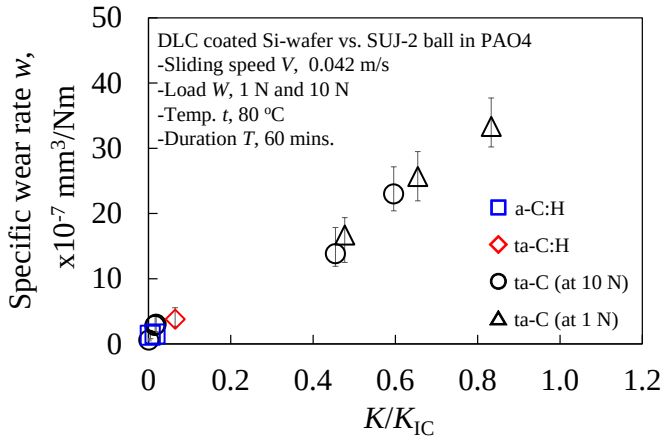

Fig. 1. Relation between specific wear rate and K/KIC of the DLC coatings.

3 Conclusion

The ratio of stress intensity factor to the critical fracture toughness K/K_{IC} was introduced, and the specific wear was characterized by K/K_{IC}. The relationship between K/K_{IC} and specific wear rate showed good linear relationship, where the specific wear rate increased with increasing K/K_{IC}. In the case DLC coatings with K/K_{IC} of more than 0.4, the main wear mechanism was fracture. On the other hand, for coatings with K/K_{IC} of less than 0.1, fracture did not occur under friction.

References

1. Nastasi M, Kodali P, Walter KC, Embury JD, Raj R, Nakamura Y. Fracture toughness of diamondlike carbon coatings. J Mater Res 1999;14:2173–80

Development of low-friction DLC surface with liquid film derived from the air using dielectric barrier discharge

Wenjun Wu [1], Noritsugu Umehara [1], Takayuki Tokoroyama [1], Motoyuki Murashima [2] and Ruixi Zhang [1]

[1] Department of Micro-Nano Mechanical Science and Engineering, Nagoya University, Japan
[2] Department of Mechanical Systems Engineering, Tohoku University, Japan
wuwenjun@ume.mech.nagoya-u.ac.jp

1 Introduction

Diamond-like carbon (DLC) is a fascinating material as a solid lubricant, and its hybridization of sp^2 and sp^3 structure provides the anti-friction, and wear-resistance characteristics. From these advantages, it is attracting research attention and is widely in the spotlight throughout mechanical applications. It has been reported that the tribomicroplasma reaction caused the production of polymers on the friction surface that reduce the friction coefficient [1]. Thus, the friction characteristics of the DLC coating can be controlled by acting on the DLC coating with the simulated tribomicroplasma. In this study, we developed a new surface treatment method by using dielectric barrier discharge (DBD) to achieve low damage treatment, which resulted in low friction. DBD is a type of non-thermal plasma formed when an AC voltage is applied across two electrodes separated by a dielectric barrier.

2 Experimental method

The tetrahedral amorphous carbon-containing nitrogen (ta-CNx) coating was deposited on SUJ2 disks by using the ion beam assisted filtered arc deposition (IBA-FAD) system. A T-shaped filter was used to eliminate macro-droplets to improve the coating quality. The effect of in-situ irradiation of DBD on the friction behavior of ta-CNx coatings was elucidated by using a ball-on-disk tribometer. In the friction test, a normal load of 0.98 N and a sliding speed of 38 mm/s were used.

3 Results

The friction test results and the effect of DBD irradiation on friction reduction are shown in Fig. 1. The results show that the average friction coefficient of ta-CNx is approximately 0.25 before DBD irradiation, and then decreases sharply to 0.01 after the third DBD irradiation. And a liquid film was observed on the surface. And after the first and second DBD irradiations, the friction coefficient returned to about 0.25. The reason may be that the liquid film could not be produced when the DBD irradiation was stopped.

Figure 2(a) shows the FTIR result. It shows that the liquid film produced in humid air contains large amounts of CH, NH, NO, and OH bands. The LC/MS results are shown in Fig. 2(b), and the results indicate that the liquid film contains nitrate ions. And the liquid film was analyzed using the pH test paper, revealing a pH value of 2 (strong acid).

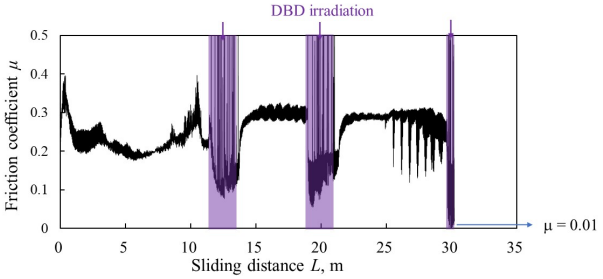

Fig. 1. The effect of DBD irradiation on friction reduction

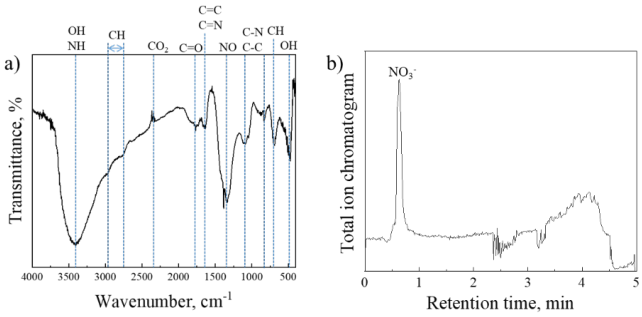

Fig. 2. Analysis results of liquid films using FTIR (a) and LC/MS (b).

4 Conclusion

In this study, we developed an in-situ surface treatment method for DLC coating using DBD. After DBD irradiation, the friction coefficient decreased from 0.25 to 0.01. In particular, when the humid air was blown to the DBD irradiation location, it was observed that a liquid film was produced on the DLC coating. Therefore, it can be considered that the CH, OH, NO, and NH bands in the liquid film are important for reducing friction. And in-situ production of acidic lubricants using DBD can be used to achieve low friction.

References

1. Nakayama K, Hashimoto H.: Triboemission, tribochemical reaction, and friction and wear in ceramics under various n-butane gas pressures. Tribology International.29(5), 385–393, (1996).

Tribo-corrosion properties of hard carbonaceous coatings

Lulu Li[1], Noritsugu Umehara [1], Takayuki Tokoroyama [1], and Ruixi Zhang [1]

[1] Department of Micro-Nano Mechanical Science and Engineering, Nagoya University, Japan
lilulu@ume.mech.nagoya-u.ac.jp

1 Introduction

From the viewpoint of combustion engines used in marine environments, the wet and salt-rich environments, particularly NaCl and water vapor, make the hot components (such as compressor blades) suffer mechanical wear, variable temperature, and corrosion simultaneously during operation. High hardness, high corrosion proof, and low friction material are desired. One of the candidate materials is hard carbonaceous coating such as tetrahedral amorphous carbon (ta-C) which has high hardness and chemical inertness. The tantalum element has also been proven to exhibit good high-temperature resistance and corrosion resistance. However, it is unclear whether the material can perform low friction (no more than 0.05) under corrosive situations.

This study conducted a friction test for ta-C, tantalum doped ta-C: Ta, and double layers ta-C/ta-C: Ta coatings to understand basic corrosion-proof ability under NaCl solution. The effect of microstructure changes and ions of NaCl solution on the friction process is also clarified.

2 Experiment method

For depositions of ta-C, ta-C: Ta, and ta-C/ta-C: Ta coatings, a hybrid coating system was used, which includes an anode-layer closed-drift linear ion source (LIS), unbalanced magnetron sputter (UBMS), and filtered cathodic vacuum arc (FCVA).

For the friction process, a ball (Si_3N_4)-on-disk (coating) type was used under 3.5 wt% NaCl solution (according to references) with temperatures of 15°C and 80°C. After the friction test, the optical microscope observed the wear track of the disk and ball. Raman spectroscope (RENISHAW in Via Reflex, England) was employed to identify the chemical structure with a 532-nm laser and 1800 lines/mm grating.

3 Experiment result

The optical microscope and Raman spectra of disk and ball wear areas (80°C) are shown in Fig.1. For the ta-C and ta-C: Ta coating, the obvious wear debris can be observed on the disk. From the Raman result, the wear area of the ta-C coating shows a W-O peak around 690 cm^{-1} from the substrate, which indicates the damage to the coating during the friction process. With the Ta doped, the wear area on the ta-C: Ta coating shows obvious peeling off, which may be the reason for the fluctuating friction

coefficient (up to 0.15). For the ta-C/ta-C: Ta coating, the obvious Ta-O peak around 670 cm^{-1} was observed on the wear area without any W element and peeling off. The wear area on the counterpart ball of ta-C/ta-C: Ta coating also shows a more continuous and dense friction film than ta-C and ta-C: Ta coating. From the Raman result, the D peak and G peak show a higher intensity for the friction film on the counterpart ball of ta-C/ta-C: Ta coating.

To compare the effect of corrosive NaCl solution on the friction properties, the wear area Raman result of disk and ball on the pure water was also conducted. Ta-O peak on the disk wear area was not sharp and the intensity was as same the as-deposited coating. Besides, the intensity of the D peak and G peak was lower than that in NaCl solution. Therefore the NaCl solution has a positive effect on the formation of Tantalum pentoxide [1,2]. Tantalum oxide is the N-type oxide with a number of oxygen vacancies. When the coating was immersed in the NaCl solution, Ta^{5+} was replaced by the Na^{+}, which reduced the electrical conductivity of the oxide and increased the formation of Ta-O[3].

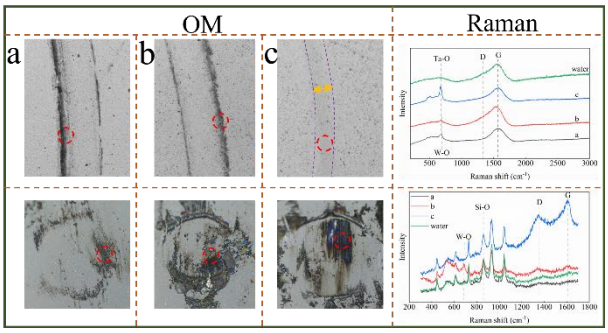

Fig. 1. Optical microscope and Raman images of wear areas, a: ta-C coating; b: ta-C: Ta coating; c: ta-C/ta-C: Ta coating.

4 Conclusions

The ta-C/ta-C: Ta coating can reduce the friction coefficient by the formation of Ta_2O_5 and carbonaceous friction film. NaCl solution can have a positive effect on the reduction of friction coefficient by the replacement of Na^{+} to promote the oxide formation.

References

[1] Yongsheng Chen, Israel E. Wachs: Tantalum oxide-supported metal oxide (Re2O7, CrO3, MoO3, WO3, V2O5, and Nb2O5) catalysts: synthesis, Raman characterization and chemically probed by methanol oxidation. Journal of Catalysis 217, 468–477 (2003).

[2] V. N. Kruchinin, V. A. Volodin, T. V. Perevalov: Optical Properties of Nonstoichiometric Tantalum Oxide TaO_x ($x < 5/2$) According to Spectral-Ellipsometry and Raman-Scattering Data. Optics and Spectroscopy 124, 808–813 (2018).

[3] B. Prakash Æ J. P. Celis: The Lubricity of Oxides Revised Based on a Polarisability Approach. Tribology Letters 27, 105–112 (2007).

Contact behavior of a sliding spherical indenter at supersonic speed

Se Jun Shim, Hyeonggeun Jo, Ilkwang Jang and Yong Hoon Jang*

School of Mechanical Engineering, Yonsei University, 50 Yonsei-ro, Seodaemun-gu, Seoul 120-749, Republic of Korea
* jyh@yonsei.ac.kr

Sliding contacts have become a subject of intense research due to their potential applications across a wide range of speeds, from low-speed brakes to high-speed systems such as rocket-sleds, rail guns, and interactions with air friction during spaceflight.

Numerous studies have investigated sliding contact problems in various dimensions and speed ranges. Cole and Huth [1] examined a two-dimensional space with line forces, while Georgiadis and Barber [2] identified errors in the proposed displacement field for transonic speeds. Craggs and Roberts [3] demonstrated the relationship between sliding object velocity and Rayleigh wave speed. Georgiadis and Barber [4] presented contact pressure based on object shape at different speeds, offering acceptable solutions for various speed regions.

Barber [5] proposed solutions for normal surface displacement in three-dimensional sliding, specifically for point forces at different speeds. Rahman [6] analysed contact pressure distribution when a rigid sphere slides on an elastic half-space at sub-Rayleigh subsonic speed, revealing an expanding contact area with increasing sliding velocity. Georgiadis and Lykotrafitis [7] extended their research on displacement caused by point forces, incorporating diverse scenarios such as thermal interaction, friction, surface vibration, and finite element analysis.

Understanding non-conforming contact sliding behaviour for 3D object shapes, particularly when sliding speeds exceed dilatational speeds, remains limited. Singular behaviour of contact pressure within specific contact areas and the presence of anticipated linear contact pressure pose challenges, influenced by kinematic considerations.

In this study, our objective is to numerically analyse the distribution of contact pressure in a three-dimensional space under steady-state conditions. Specifically, we investigate the scenario where a frictionless, rigid spherical object slides on an elastic half-space at supersonic speeds. To accomplish this, we employ the integral equation for contact pressure, incorporating the gap function and contact condition equation based on Barber's proposed Green function solution [5]. Our primary focus is to present the findings regarding the contact pressure distribution and contact area within the regime where the sliding speed exceeds the dilatation speed. This critical range of analysis holds significant importance for understanding the behaviour of the system.

Examining the typical distribution of contact pressure, as depicted in Figure 1, we observe that it corresponds to the contact pressure distribution when the sliding speed is 2.5 times the shear speed (represented by c_2). The contact region can be categorized into two distinct areas based on the magnitude of the sliding speed. The first area resides

near the contact edge, where the propagation of the dilatation wave occurs. The second area lies beyond, where the Rayleigh wave propagates.

Notably, within the region characterized by dilatation speed and wave propagation, the contact pressure exhibits a linear pattern, aligning with the predictions from the two-dimensional results. Additionally, the contact surface assumes a spherical or ellipsoidal shape. These outcomes emphasize the influential role of kinematics in the contact analysis, thereby shaping the observed results.

By conducting this comprehensive investigation, we contribute to the understanding of contact pressure distribution and its dependence on various factors within the given sliding scenario.

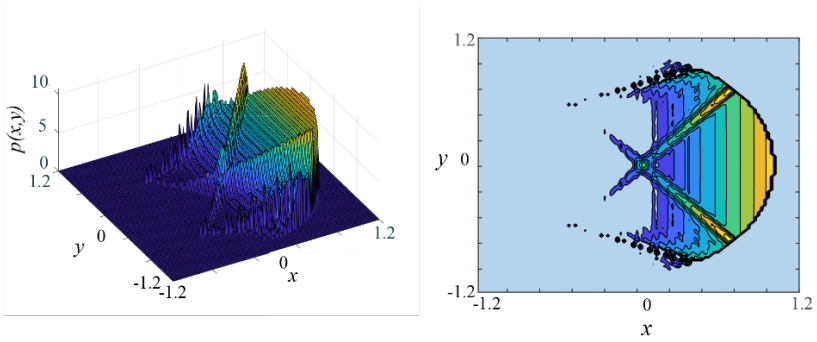

Fig. 1. Contact pressure distribution in supersonic sliding speed of $V = 2.5c_2$.

Acknowledgment: This work was supported by the National Research Foundation of Korea(NRF) grant funded by the Korea government(MSIT) (No.2021R1A2C3010731).

References

1. Cole, J.D., Huth J.H.: Stresses produced in a half plane by moving loads. ASME J. Appl. Mech. 25, 433-436 (1958).
2. Georgiadis H.G., Barber J.R.: Steady-state transonic motion of a line load over an elastic half-space: The corrected Cole/Huth solution. ASME J. Appl. Mech. 60, 772-774 (1993).
3. Craggs J.W., Roberts A.M.: On the motion of a heavy cylinder over the surface of an elastic solid. ASME J. Appl. Mech. 34, 207-209 (1967).
4. Georgiadis H.G., Barber J.R.: On the super-Rayleigh/subseismic elastodynamic indentation problem. J. Elast. 31, 141-161 (1993).
5. Barber J.R.: Surface displacements due to a steadily moving point force. ASME J. Appl. Mech. 63, 245-251 (1996).
6. Rahman M., Barber J.R.: Exact expressions for the roots of the secular equation for Rayleigh waves. ASME J. Appl. Mech. 62,250-252 (1995).
7. Georgiadis H.G, Lykotrafitis G.: A method based on the radon transform for three-dimensional elastodynamic problems of moving loads. J. Elast. 65, 87-129 (2001).

Highly Flexible Stretchable Strain Sensor with Sensitivity and Durability for Human-Motion Detection

Sung-Jun Lee [0009-0001-1059-6050], Dae-Hyeon Kim [0009-0009-3461-301X] and Chang-Lae Kim*[0000-0002-1983-0181]

Department of Mechanical Engineering, Chosun University, Gwangju 61452, Republic of Korea
*kimcl@chosun.ac.kr

1 Introduction

Stretchable and flexible electronics have been widely used in e-skin, wearable electronics, and strain sensors [1]. In particular, flexible strain sensors are attracting great attention in various fields, such as medical monitoring, human-machine interaction, and electrocardiogram sensors, due to their excellent efficiency in converting changes in human body movement into electrical signals [2]. Generally, strain sensors are composed of conductive materials and flexible elastomers to detect human motion [3]. To monitor human motion, strain sensors must meet the requirements of elasticity, high sensitivity, fast response and recovery, and durability [3]. Additionally, the durability of the strain sensor must be high enough not to be affected by human activity. Although considerable research has been done on strain sensors over the past few decades, fabricating a sensor with both high durability and sensitivity remains a challenge. Among various fabrication processes, spray coating was chosen in this work to impart conductivity to the elastomer. Compared to the typical sputtering deposition method, spray coating enabled thickness control and rapid fabrication.

In this study, we report a strain sensor with improved durability. This strain sensor was fabricated by embedding CNTs in polydimethylsiloxane (PDMS). By controlling the curing degree of PDMS, the optimized strain sensor exhibits excellent sensitivity and durability. Strain sensors made with a simple production process can be applied to sensors for detecting human motion.

2 Experimental Methods

Prior to spray coating, commercially available CNTs were dispersed at a concentration of 3 wt% in isopropyl alcohol. The CNTs were successfully embedded in the PDMS surface through the curing parameters of PDMS. A multimeter and a sheet resistance meter were used to investigate the electrical characteristics of the fabricated strain sensor. Additionally, we investigated the durability of the strain sensor according to the degree of curing of PDMS through repeated deformation tests and friction tests. The resistance and friction coefficient were monitored in real-time to obtain signals for repeated deformation and sliding cycles. The shape of the wear track was observed to confirm the wear resistance according to the degree of CNT embedding.

3 Results and Discussion

The electrical properties of CNT-embedded PDMS were considerably varied by controlling the curing degree of PDMS. These electrical changes showed a big difference in the electrical durability of each sensor. Additionally, different types of strain sensors exhibited significantly different friction/wear characteristics. That is, in the case of a sensor with a short pre-curing time of PDMS, it was confirmed that the electrical durability was quite stable. Therefore, it was suggested that the thickness of the CNT coating layer embedded in the PDMS surface has a significant effect on the electrical and tribological properties. Overall, the experimental results suggest that the degree of curing of PDMS can play an effective role in improving the performance of strain sensors.

4 Conclusions

Highly flexible and durable strain sensors using PDMS-based composites in which CNTs are embedded by controlling the curing degree of PDMS have been fabricated through a simple and efficient spray coating process. The experimental results show that these strain sensors exhibit excellent stability and high durability from 0-100% strain. Furthermore, the CNT embedded layer according to the curing degree of PDMS plays a significant role in the electrical properties and wear resistance of the fabricated strain sensor. Interestingly, as the pre-curing time of PDMS is shortened, the electrical conductivity and wear resistance show opposite trends, which suggests the potential to tune the properties of the sensor. These results indicate that the strain sensor has great potential in the field of wearable electronics, as it can detect both large and small human body movements with high sensitivity and durability.

Acknowledgment

This research was supported by Basic Science Research Program through the National Research Foundation of Korea (NRF) funded by the Ministry of Education (2021R1I1A3059770).

References

1. Kim, S. O., Han, C. J., Kim, Y., Kim, K. S., Kim, D. U., Lee, C. R., Kim, J. W.: Fabrication of a bending-insensitive in-plane strain sensor from a reversible cross-linker-functionalized silicone polymer. ACS Applied Materials & Interfaces 12, 6516-6524 (2020).
2. Fan, K., Wei, W., Zhang, Z., Liu, B., Feng, W., Ma, Y., Zhang, X.: Highly stretchable, self-healing, and adhesive polymeric eutectogel enabled by hydrogen-bond networks for wearable strain sensor. Chemical Engineering Journal 449, 137878 (2022).
3. Lee, S. J., Kim, C. L.: Highly flexible, stretchable, durable conductive electrode for human-body-attachable wearable sensor application. Polymer Testing 122, 108018 (2023).